UNIVERSIDADE FEDERAL DE MINAS GERAIS
Programa de Pós-Graduação em Engenharia Metalúrgica, Materiais e de Minas

Tese de Doutorado

INFLUÊNCIA DO PROCESSAMENTO POR DEFORMAÇÃO PLÁSTICA SEVERA NO COMPORTAMENTO MECÂNICO, ELETROQUÍMICO E CITOTÓXICO DO MAGNÉSIO.

Autor: Cláudio Laudares Passos Silva
Orientador: Roberto Braga Figueiredo

Outubro/2018

UNIVERSIDADE FEDERAL DE MINAS GERAIS
Programa de Pós-Graduação em Engenharia Metalúrgica, Materiais e de Minas

Cláudio Laudares Passos Silva

INFLUÊNCIA DO PROCESSAMENTO POR DEFORMAÇÃO PLÁSTICA SEVERA NO COMPORTAMENTO MECÂNICO, ELETROQUÍMICO E CITOTÓXICO DO MAGNÉSIO.

Tese de doutorado apresentada ao Programa de Pós-Graduação em Engenharia Metalúrgica, Materiais e de Minas da Escola de Engenharia da Universidade Federal de Minas Gerais, como requisito parcial para obtenção do grau de Doutor em Engenharia Metalúrgica, Materiais e de Minas.

Área de Concentração: Ciência dos materiais.
Orientador: Roberto Braga Figueiredo

Belo Horizonte
Universidade Federal de Minas Gerais
Escola de Engenharia
2018

Silva, Cláudio Laudares Passos.

S586i Influência do processamento por deformação plástica severa no comportamento mecânico, eletroquímico e citotóxico do magnésio [manuscrito] / Cláudio Laudares Passos Silva. - 2018.

xiii,106 f., enc.: il.

Orientador: Roberto Braga Figueiredo.

Tese (doutorado) - Universidade Federal de Minas Gerais, Escola de Engenharia.

Apêndice: f.104 – 106.

Inclui bibliografia.

1. Engenharia metalúrgica - Teses. 2. Ciência dos materiais - Teses. 3. Magnésio - Teses. 4. Corrosão - Teses. I. Figueiredo, Roberto Braga. II. Universidade Federal de Minas Gerais. Escola de Engenharia. III.Título.

CDU: 669(043)

SUMÁRIO

LISTA DE FIGURAS

LISTA DE EQUAÇÕES

LISTA DE ABREVIATURAS

I_{Corr} = Corrente de corrosão

ΔW = Taxa de perda de massa

P_W = Taxa de penetração

V_H = Taxa de evolução de hidrogênio

ECAP = *Equal Channel Angular Pressing*

HPT = *High Pressure Torsion*

AZ31 = Liga de magnésio com 3% de alumínio e 1% de Zinco

AZ91 = Liga de magnésio com 9% de alumínio e 1% de Zinco

ZK60 = Liga de magnésio com 6% de Zinco e 0,4 % de Zircônio

CP-Mg = Magnésio comercialmente puro

wt.% = Percentual em peso

MEV = Microscopia eletrônica de varredura

MET = Microscopia eletrônica de transmissão

MTT = 3-(4,5-dimetiltiazol-2yl)-2,5-difenil brometo de tetrazolina

LISTA DE SÍMBOLOS

Φ – Ângulo de interseção dos canais da matriz de ECAP

σ – Tensão verdadeira

ε – Deformação verdadeira

$\dot{\varepsilon}$ – Taxa de deformação

N – Número de passes de ECAP

A – Rota de processamento em que a amostra não sofre rotação entre os passes de ECAP

B_A – Rota de processamento em que a amostra sofre rotação de 90º em sentidos alternados entre os passes de ECAP

B_C – Rota de processamento em que a amostra sofre rotação de 90º no mesmo sentido entre os passes de ECAP

C – Rota de processamento em que a amostra sofre rotação de 180º entre os passes de ECAP

RESUMO

Entre os materiais com potencial para aplicações em implantes biodegradáveis o magnésio tem ganhado uma atenção especial por apresentar uma boa combinação de propriedades mecânicas, biológicas e eletroquímicas. Estudos recentes mostram que o processamento do magnésio por deformação plástica severa refina a microestrutura e melhora as propriedades mecânicas. O presente trabalho mostra a caracterização microestrutural e mecânica do magnésio puro e de ligas comerciais AZ31, AZ91 e ZK60 após processamento por ECAP (*Equal-Channel Angular Pressing*) e HPT (*High Pressure Torsion*). O magnésio comercialmente puro (CP-Mg) foi processado por ECAP em alta temperatura e por HPT na temperatura ambiente. As ligas de magnésio foram processadas por HPT na temperatura ambiente. Para avaliar possíveis modificações nas propriedades mecânicas causadas pelo processamento foram feitos ensaios de tração em temperatura ambiente das amostras de magnésio e foram construídos mapas de distribuição de dureza das seções transversais das amostras processadas por HPT. A taxa de corrosão de todas as amostras foi determinada por meio de ensaios eletroquímicos de polarização e ensaios de evolução de hidrogênio. A resistência de polarização também foi medida utilizando técnicas de espectroscopia de impedância eletroquímica EIS (*electrochemical impedance spectroscopy*). Para comparar os aspectos morfológicos do processo corrosivo em cada amostra também foram realizados ensaios de inspeção visual com registro fotográfico. Para avaliação da citotoxicidade foram utilizados dois testes diferentes o MTT e o teste comercial Live/Dead. O tipo de distribuição e o tamanho médio de grão nas amostras em cada etapa de processamento foram avaliados utilizando procedimentos de metalografia e a aquisição de imagens foi feita por microscopia óptica, microscopia eletrônica de varredura (MEV), e microscopia eletrônica de transmissão (MET), no caso das amostras com microestrutura ultrafina. Os resultados mostram que o processamento por HPT refina a estrutura de grãos do magnésio e suas ligas até a escala submicrométrica e aumenta significativamente a dureza. A biocompatibilidade não é afetada pelo processamento e o comportamento durante a corrosão varia dependendo do material processado. O refino de grão promove uma mudança no comportamento em corrosão de um perfil de corrosão localizada para corrosão generalizada no magnésio puro. Os resultados dos ensaios eletroquímicos não mostram mudanças significativa nas ligas de magnésio após processamento por HPT.

Palavras-chave: Magnésio, Corrosão, Citotoxidade, HPT, ECAP.

ABSTRACT

Among the materials with potential for applications as biomaterials magnesium has received special attention due to their good combination of desirable (mechanical, biological and electrochemical) properties. Recent studies show that the processing of magnesium by severe plastic deformation refines the microstructure and improves the mechanical properties. The present work shows the microstructural and mechanical characterization of pure magnesium and commercial alloys AZ31, AZ91 and ZK60 after processing by ECAP (Equal-Channel Angular Pressing) and HPT (High Pressure Torsion). Commercially pure magnesium (CP-Mg) was processed by ECAP at high temperature and by HPT at room temperature. The magnesium alloys were processed by HPT at room temperature. To evaluate possible modifications in the mechanical properties caused by the processing tensile tests were performed at room temperature on magnesium samples and hardness distribution maps of HPT discs cross section were constructed. The corrosion rate of all samples was determined by electrochemical polarization tests and hydrogen evolution tests. The polarization resistance was also measured using electrochemical impedance spectroscopy (EIS) techniques. To compare the morphological aspects of the corrosive process in each sample, visual inspection tests with photographic record were also carried out. To evaluate the cytotoxicity, two different tests were used the MTT and the Live / Dead assays. The distribution and the average grain size in the samples at each processing stage were evaluated using metallography procedures and the image acquisition was performed by optical microscopy, scanning electron microscopy (SEM) and transmission electron microscopy (MET) in the case of samples with ultrafine microstructure. The results show that HPT processing refines the grain structure of magnesium and its alloys to submicron scale and significantly increases hardness. Biocompatibility is not affected by processing and the corrosion behavior varies depending on material. Grain refinement promotes a change from localized corrosion to generalized corrosion in pure magnesium. The electrochemical tests results do not show significant changes on corrosion behavior of magnesium alloys after processing by HPT.

Key words: Magnesium, Corrosion, Cytotoxicity, HPT, ECAP.

ESTRUTURA DA TESE

No capítulo 1, são apresentadas as considerações iniciais a respeito do uso do magnésio como matéria prima para a fabricação de implantes biodegradáveis e os objetivos que nortearam a execução dessa pesquisa.

No capítulo 2 é feita uma revisão de literatura tendo como tópicos principais: o processamento por deformação plástica severa, a corrosão dos metais em geral e do magnésio especificamente, as principais técnicas de medição da taxa de corrosão e por fim o uso do magnésio como material biodegradável.

Os manuscritos produzidos a partir dos resultados deste trabalho compõem os capítulos 3, 4 e 5. Um estudo sobre a evolução da microestrutura e da dureza em etapas sucessivas de processamento do magnésio por HPT, publicado em 2017 no periódico Materials Research, é descrito no capítulo 3.

Um segundo trabalho publicado em 2017 no periódico Journal of Materials Science é apresentado no capítulo 4. Nesse trabalho foi realizado um estudo sobre o efeito do processamento por deformação plástica severa no comportamento mecânico, na biocompatibilidade e na taxa de corrosão do magnésio.

Por sua vez, um terceiro artigo, recentemente submetido para publicação, é apresentado no capítulo 5. Esse artigo se refere a um estudo que compara o efeito do processamento por HPT na microestrutura, dureza e resistência à corrosão no magnésio puro e em ligas comerciais de magnésio.

No capítulo 6, são abordadas as considerações finais, as contribuições originais e as publicações relacionadas a essa pesquisa. Nessa parte do texto também são apresentadas sugestões para trabalhos futuros.

1. CAPÍTULO 1 – CONSIDERAÇÕES INICIAIS

1.1 Introdução

O magnésio é um material metálico que se enquadra em uma nova classe de materiais biodegradáveis então chamados metais biodegradáveis e tem ganhado uma atenção especial, pelo fato de apresentar uma boa combinação de características mecânicas, biológicas e eletroquímicas. A boa compatibilidade biológica e a capacidade de degradação em meio fisiológico faz com que o magnésio possa ser utilizado como matéria prima em implantes biodegradáveis. Além disso, ele apresenta uma boa relação resistência/peso e módulo de elasticidade com valor próximo aos dos ossos humanos (40 - 45) GPa o que é um fator favorável levando em consideração que materiais com módulo de elasticidade superiores podem causar perda de densidade óssea (osteoporose) na região implantada, devido a um fenômeno conhecido como *stress shielding*. Porém existem fatores adversos que limitam ou inviabilizam o uso desse material em implantes biodegradáveis. O magnésio puro apresentam propriedades mecânicas inferiores se comparado aos metais inertes normalmente utilizados em implantes. Ele apresenta baixa ductilidade e baixa resistência mecânica (tensão de escoamento ~ 20 MPa). Apesar da degradação ser desejável a elevada taxa de corrosão em meio fisiológico faz com que os implantes feitos à base de magnésio percam as suas características mecânicas prematuramente o que compromete a funcionalidade dos mesmos. Outro fator adverso esta relacionado a liberação de hidrogênio, que é um subproduto da corrosão. No uso em implantes ortopédicos, a elevada taxa de liberação de hidrogênio somada à baixa taxa de absorção pelo organismo, faz com esse gás que se acumule ao redor do implante o que pode desencadear reações fisiológicas indesejáveis.

Para melhorar as propriedades mecânicas dos metais puros muitas vezes são adicionados elementos de liga, porém no caso do magnésio a presença de elementos de liga pode aumentar a taxa de corrosão e dependendo da quantidade e do tipo de elementos utilizados a biocompatibilidade do material pode ser comprometida. A degradação das ligas de magnésio pode causar respostas fisiológicas adversas se os íons de magnésio e dos elementos de liga forem liberados a uma taxa muito alta e nessa

condição mesmo os elementos que normalmente estão presentes no organismo (ex: Zn, Ca, e Mn) podem ser tornar tóxicos.

Outra estratégia para melhorar as propriedades mecânicas e reduzir a taxa de degradação, que vem sendo utilizada, é o processamento por deformação plástica severa, SPD (*severe plastic deformation*) e se baseia no fato de que é possível modificar a cinética de corrosão por meio de mudanças na microestrutura do material sem alterar sua composição química. Dentre as técnicas de SPD disponíveis, podemos destacar o processo de prensagem em canal angular ECAP (*Equal channel angular pressing*) e a torção sobre alta pressão HPT (*High prssure torsion*). O processamento por SPD normalmente é utilizado para refinar a estrutura de grãos dos materiais metálicos e obter uma melhora nas propriedades mecânicas. Sendo assim, o processamento do magnésio por ECAP ou HPT abre uma possibilidade de se obter, simultaneamente, uma melhora das propriedades mecânicas e redução da taxa de corrosão desse material.

1.2 Objetivos

1.2.1 Geral

O objetivo desse trabalho é avaliar a influência do processamento por deformação plástica severa, no comportamento mecânico, eletroquímico e citotóxico do magnésio e das ligas AZ31, AZ91 e ZK60.

1.2.2 Específicos

- Processar o magnésio e as ligas por deformação plástica severa.

- Determinar a dureza e a resistência à tração de amostras de magnésio e ligas submetidas a processamento por deformação plástica severa.

- Determinar a taxa e o perfil de corrosão dos materiais em solução salina de 3,5 wt.% NaCl utilizando ensaios eletroquímicos, teste de evolução de hidrogênio e inspeção visual.

- Determinar a influência do tamanho de grão na citotoxidade dos materiais, em células de osteosarcoma humano (SAOS), utilizado os testes MTT (3-(4,5-dimetiltiazol-2yl)-2,5-difenil brometo de tetrazolina) e o teste LIVE/DEAD.

2. CAPÍTULO 2 - REVISÃO BIBLIOGRÁFICA

2.1 Deformação plástica severa

O processamento por deformação plástica severa, SPD (*severe plastic deformation*) é um processo de conformação mecânica em que todo o volume de uma amostra é submetido a um grau elevado de deformação sem produzir mudanças significativas nas dimensões da seção transversal e é feito com o intuito de criar estruturas com granulação ultrafina (tamanho médio de grão < 1μm) (VALIEV e LANGDON, 2006). Entre as técnicas de SPD mais utilizadas, pode se destacar a prensagem em canal angular ECAP (*equal channel angular pressing*) e a torção sobre alta pressão HPT (*high pressure torsion*).

2.1.1 ECAP

O ECAP é um tipo de processamento mecânico que consiste em pressionar uma amostra de determinado material contra uma matriz com dois canais de mesma seção transversal e que se interceptam em ângulo. É um tipo de processamento termo-mecânico em que as deformações impostas ao material acontecem por cisalhamento simples em uma pequena região no plano de interseção dos canais da matriz (SEGAL, 1995). A figura 2.1 apresenta o esquema de uma matriz de ECAP com ângulo de interseção entre canais Φ de 90°.

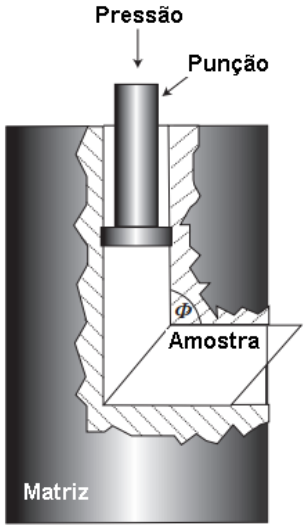

Figura 2.1 – esquema de uma matriz de ECAP com ângulo de interseção entre canais Φ de 90°.
Fonte: Adaptado de (VALIEV, 2004).

Poggiali *et al.* (2014) conseguiram refinar e homogeneizar a microestrutura do magnésio comercialmente puro realizando o processamento por ECAP. Amostras do material no estado fundido foram laminadas e, posteriormente, processadas por ECAP. O material no estado fundido apresentava microestrutura heterogenia e com tamanho médio de grão de aproximadamente 480μm. Após a laminação, a microestrutura foi parcialmente refinada e o material apresentava regiões com grãos finos com tamanho médio de 5μm e regiões mais grosseiras com grãos da ordem de dezenas de microns. Com o processamento por ECAP, a microestrutura foi completamente refinada e o tamanho médio de grão foi reduzido para 5μm. Na figura 2.2 são apresentadas as imagens das microestruturas do magnésio no estado fundido, laminado e processado por ECAP respectivamente.

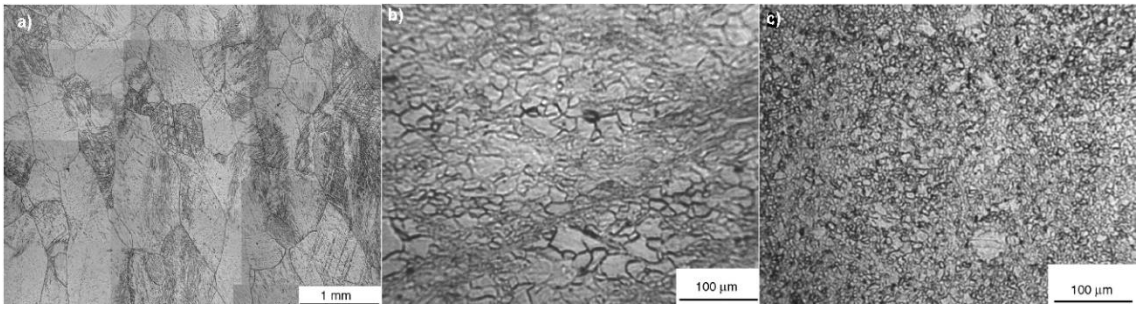

Figura 2.2 – Microstrutura do magnésio como fundido (a), processado por laminação (b) e laminação + ECAP (c)
Fonte: Adaptado de (POGGIALI, 2014).

2.1.2 HPT

No processamento por torção sobre alta pressão HPT, uma amostra de material em formato de disco é prensada entre dois cilindros e, após a aplicação da pressão, um dos cilindros executa um movimento de rotação com velocidade constante. A pressão aplicada ajuda a manter a integridade do material prevenindo o aparecimento de trincas e a grande diferença entre as dimensões do diâmetro do disco e sua espessura faz com que durante a rotação do punção o material acumule um elevado grau de deformação (FIGUEIREDO *et al.,* 2012). Na Figura 2.3 é apresentado de maneira esquemática o processamento por HPT.

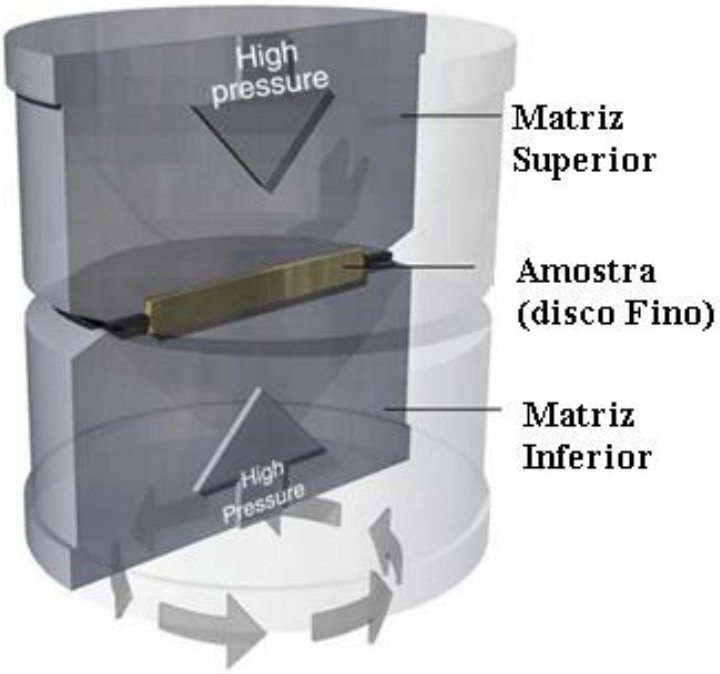

Figura 2.3 – Esquema do processamento por HPT.
Fonte: Adaptado de (SHARMAN *et al.*, 2015).

No processamento do magnésio e ligas por HPT é possível refinar os grãos até dimensões submicrométricas e obter materiais com estrutura nanocristalina. Com processamento da liga AZ61 por HPT, por exemplo, é possível refinar a microestrutura ao ponto de se obter materiais com tamanho médio de grão de 220nm e 110nm quando o processamento é realizado na temperatura de 423K e em temperatura ambiente, respectivamente. Inicialmente, o refino de grão é mais acentuado na borda do disco e com um aumento do número de voltas a microestrutura tende a ficar homogênea ao longo de toda a extensão do disco (HARAI *et al.*, 2008). As variações microestruturais na liga AZ61 processada por HPT a 423K registradas por microscopia óptica são apresentadas na figura 2.4 que mostra a microestrutura típica no centro, em posições próximas do centro do disco e nas bordas após o processamento por 1, 3, 5, e 7 voltas.

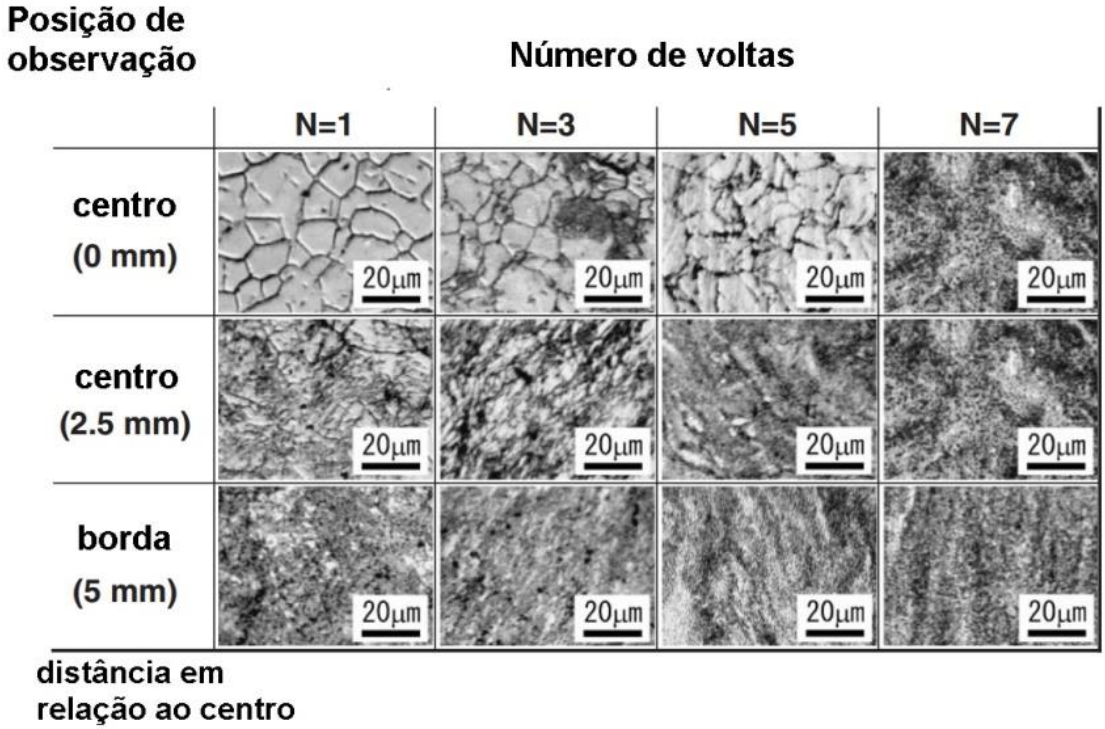

Figura 2.4 – Imagens ópticas mostrando a microestrutura após o processamento por HPT no centro, em posições intermediárias e na borda de cada disco processados por 1, 3, 5 e 7 voltas de HPT na temperatura de 423K.
Fonte: Adaptado de (Harai *et al.*, 2008).

2.2 Corrosão dos materiais metálicos

Segundo McCafferty (2010), a corrosão é um ataque destrutivo do metal devido à reação com o meio. O processo corrosivo geralmente não acontece devido a uma reação química direta entre o metal e o meio, mas sim por meio de duas reações de meia-pilha. Uma reação anódica (oxidação) em que os elétrons aparecem como um produto, e uma reação catódica (redução) na qual os elétrons aparecem como reagentes. A perda do material metálico acontece devido a uma reação anódica como da eq. (2.1) e que aparece representada de maneira esquemática na figura 2.5. A formação de hidrogênio gasoso na superfície do material é um exemplo de reação catódica eq. (2.2) predominante em meios ácidos. Essa reação pode ser esquematizada como na Figura 2.6.

$$\mathrm{Fe\,(s)} \rightarrow \mathrm{Fe^{2+}\,(aq)} + 2\mathrm{e^-} \qquad (2.1)$$

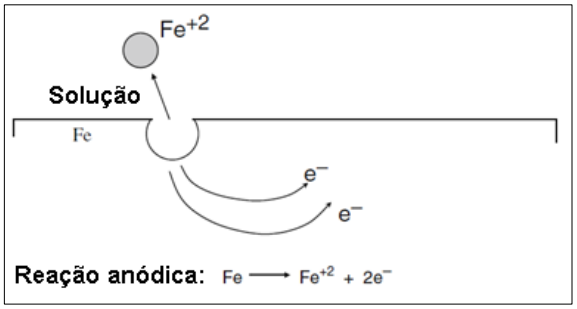

Figura 2.5 – Esquema da dissolução do ferro por meio de uma reação anódica.
Fonte: Adaptado de (McCAFFERTY, 2010).

$$2H^{+}(aq) + 2e^{-} \rightarrow H_2(g) \qquad (2.2)$$

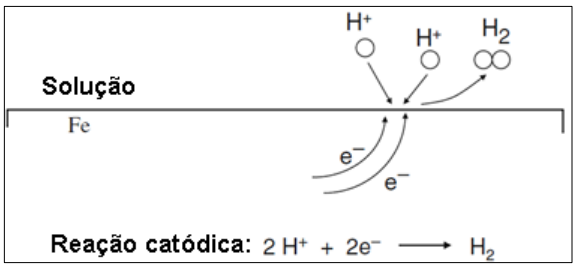

Figura 2.6 – Esquema da evolução de hidrogênio para o ferro imerso em solução ácida.
Fonte: Adaptado de (McCAFFERTY, 2010).

De acordo com McCafferty (2010), devido à natureza heterogênea das superfícies metálicas, é possível que as reações de meia-pilha (reação anódica e reação catódica) ocorram em uma mesma superfície metálica. A superfície dos metais policristalinos apresenta uma gama de regiões com diferentes valores de energia devido à existência de defeitos na estrutura cristalina (ex: deslocações, vacâncias, contornos de grão), defeitos na superfície do material (como cantos e quinas) e também a presença de impurezas (como átomos metálicos e íons adsorvidos da solução). Os átomos do metal localizados em regiões de alta energia possuem uma tendência maior de se dissolverem na solução. Durante o trabalho a frio e nos processos de conformação mecânica, algumas regiões da rede cristalina do metal são tensionadas e os átomos localizados nessas regiões tendem a sofrer uma dissolução mais rápida que os átomos das regiões não tensionadas. A partir do momento em que o processo de dissolução do metal se inicia, as posições das regiões anódicas e catódicas mudam de maneira aleatória e assim é possível ocorrer uma corrosão uniforme.

2.3 Corrosão do magnésio e suas ligas

2.3.1 Influência dos elementos de liga

O magnésio apresenta uma limitada resistência à corrosão em vários meios (MORDIKE e EBERT, 2001) e uma das causas é o fato do filme formado na superfície desse metal não ser estável (SONG e ATRENS, 2003). A estabilidade e espessura do filme formado na superfície do magnésio são influenciadas pela presença de impurezas e de elementos de liga sendo que o filme formado em amostras da liga AZ91D e de magnésio de alta pureza expostos a 0.1M de NaCl e 0.1M Na_2SO_4 possuem capacidade de passivação do substrato (HARA *et al.,* 2007). Os diversos elementos, adicionados para formar ligas ou presentes como impurezas, causam diferentes influências no comportamento em corrosão do magnésio. Alguns elementos como (Ni, Fe, Cu e Co) em concentrações menores que 0.2% causam perda acentuada de resistência à corrosão das ligas de magnésio e com aumento do nível desses elementos a taxa de degradação pode ser acelerada de 10 a 100 vezes (SONG e ATRENS, 2003). Sendo assim a redução do nível dessas impurezas é uma forma de aumentar a resistência à corrosão do magnésio e suas ligas. O magnésio de alta pureza apresenta um valor de taxa de corrosão bastante reduzido e por isso é utilizado como referência para avaliar o desempenho das ligas de magnésio (SONG *et al.,* 1999).

A presença da segunda fase influencia bastante no comportamento em corrosão do magnésio e alguns elementos só causam alguma influência mensurável quando essa fase é formada. Nas ligas de magnésio a matriz metálica (fase α) possui um potencial de corrosão mais negativo que a fase β, isso acontece porque a segunda fase é formada pela reação entre magnésio e outro metal menos reativo. A fase β apresenta uma grande resistência à corrosão se comparada à fase α e é inerte em soluções de NaCl. Devido a essas características a segunda fase apresenta duas influências principais no comportamento em corrosão das liga de magnésio. Quando presente em pequena quantidade a fase β serve como um catodo formando pares galvânicos com a matriz metálica e acelerando o processo de degradação, mas se a fração da segunda fase é grande ela pode agir como uma barreira inibindo a corrosão da liga em geral (SONG *et al.,* 1999). Na tabela 2.1 são apresentados os potenciais de corrosão do magnésio puro e

das fases alfa e beta na liga AZ91. Medidos após 2 h em solução desaerada de 5% de NaCl e saturada com $Mg(OH)_2$ e com (pH 10.5).

Tabela 2.1 – Valores típicos de potencial de corrosão para o magnésio e segunda fases de magnésio em solução de 5% de NaCl.
Fonte: (SONG *et al.*, 2003).

Metal	E_{corr}, V_{SCE}
Mg	-1.65
Mg_2Si	-1.65
Al_6Mn	-1.52
Al_4Mn	-1.45
Al_8Mn_5	-1.25
$Mg_{17}Al_{12}$ (β)	-1.20
Al_8Mn_5(Fe)	-1.20
Beta-Mn	-1.17
Al_4MM	-1.15
Al_6Mn(Fe)	-1.10
Al_6(MnFe)	-1.00
Al_3Fe(Mn)	-0.95
Al_3Fe	-0.74

2.3.2 Medidas da taxa de corrosão do magnésio

Um dos procedimentos mais utilizados para medir a taxa de corrosão dos metais é por meio de medidas de perda de massa. A medida de perda de massa ΔW expressa em ($mg.cm^{-2}.d^{-1}$) pode ser convertida para taxa de penetração P_W expressa em ($mm.ano^{-1}$) utilizando a seguinte relação (ZHAO *et al.*, 2009)

$$P_W = 3{,}65\,\Delta W / \rho \qquad (2.3)$$

onde ρ é a densidade do metal em ($g.cm^{-3}$). Para as ligas de magnésio, ρ é 1,74 $g.cm^{-3}$, e assim a equação (2.3) pode ser reescrita como:

$$P_W = 2{,}10\ \Delta W \tag{2.4}$$

Também é possível calcular a taxa de corrosão do magnésio estimando a densidade de corrente de corrosão, i_{Corr} ($mA.cm^{-2}$) por meio de ensaios eletroquímicos realizando um ajuste linear no ramo catódico da curva de polarização sobre os pontos da região de Tafel. O ensaio de polarização consiste em aplicar uma diferença de potencial elétrico entre o eletrodo de trabalho (amostra a ser estudada) e o eletrodo de referência e simultaneamente medir a corrente que flui entre o eletrodo de trabalho e um terceiro eletrodo chamado contra eletrodo, que deve ser feito de um material inerte (ex: platina).

A corrente de corrosão i_{Corr} pode ser relacionada à taxa de penetração P_w utilizando a eq. (2.5) (ZHAO *et al.*, 2009)

$$P_W = 22{,}85\ i_{Corr} \tag{2.5}$$

Combinando a eq. (2.4) com a eq. (2.5), é possível chegar a uma expressão para calcular a correspondente taxa de corrosão ΔW a partir da corrente de corrosão.

$$\Delta W = 10{,}88\ i_{Corr} \tag{2.6}$$

Existem vários problemas com medidas realizadas utilizando as técnicas eletroquímicas tradicionais, pois o mecanismo de corrosão tem implicações nas medidas da taxa de corrosão do magnésio e suas ligas (SONG e ATRENS, 2003). As taxas de corrosão das ligas de magnésio, calculadas a partir das curvas de polarização utilizando o método de extrapolação de Tafel, não condizem com os resultados obtidos por perda de massa ou evolução de hidrogênio. O desvio relativo da taxa de corrosão obtida por extrapolação de Tafel em relação aos resultados obtidos por perda de massa e evolução de hidrogênio varia de 48% a 96% (SHI *et al.*, 2010).

Uma maneira prática de medir a taxa de corrosão das ligas de magnésio em meio aquoso é por meio da quantidade de hidrogênio gerada (SONG *et al.*, 2001). De acordo com a equação geral de corrosão para o magnésio puro, eq. (2.7), para cada átomo do

metal que reage, uma molécula de hidrogênio gasoso é produzida (HAGIHARA *et al.*, 2016).

$$Mg\,(s) + 2\,H_2O\,(aq) \rightarrow Mg\,(OH)_2(s) + H_2(g) \quad \text{(reação geral)} \tag{2.7}$$

Sendo assim, para cada mol (24,32 g) de átomos de magnésio dissolvidos, um mol (22,4 L) de gás hidrogênio é produzido. Logo a taxa de evolução de hidrogênio V_H ($ml.cm^{-2}.d^{-1}$) pode ser convertida em perda de massa ΔW ($mg.\ cm^{-2}.d^{-1}$) utilizando a relação (ZHAO *et al.*, 2009)

$$\Delta W = 1{,}085\ V_H \tag{2.8}$$

Na Figura 2.7, é apresentado o esquema de uma montagem para medir a quantidade de hidrogênio liberada no processo de dissolução do magnésio. Nessa montagem, a amostra é mergulhada em um béquer com a solução (meio corrosivo) e coberta por um funil sobre o qual é colocada uma bureta cheia com a mesma solução.

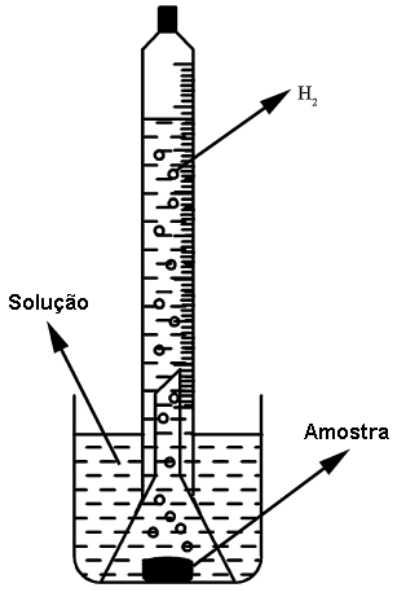

Figura 2.7 – Esquema da montagem para a medida da taxa de corrosão por meio da quantidade de hidrogênio gerada.
Fonte: Adaptado de (ZHAO *et al.*, 2015).

Song e Atrens (2003) compararam as taxas de corrosão do magnésio e de várias ligas medidas por perda de massa e por evolução de hidrogênio (Figura 2.8). Foi verificado que existe uma boa correlação entre as medidas realizadas com os dois métodos.

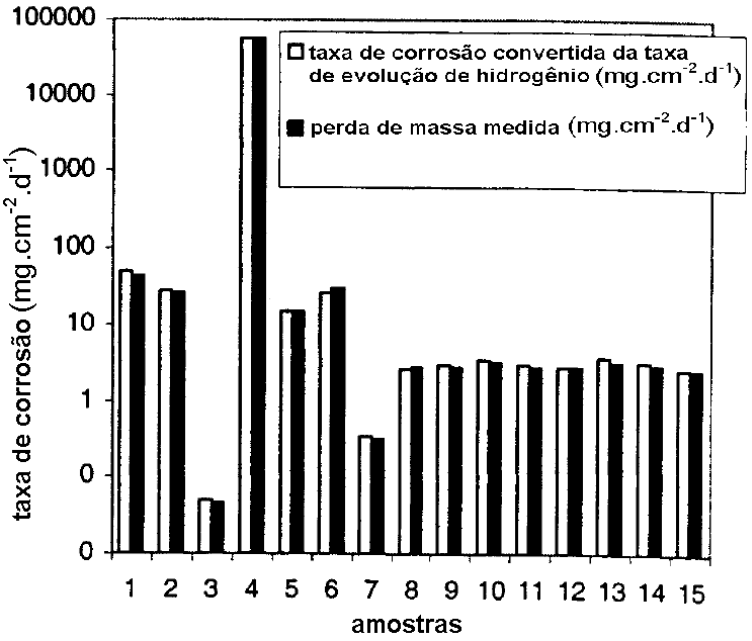

Figura 2.8 – Taxas de perda de massa e de evolução de hidrogênio para várias amostras.
A taxa de evolução de hidrogênio foi convertida para taxa de perda de massa considerando que a dissolução de um átomo de magnésio produz uma molécula de hidrogênio.
Fonte: Adaptado de (SONG e ATRENS, 2003).

2.3.3 Corrosão do magnésio processado por deformação plástica severa

Além da composição química, a taxa de corrosão do magnésio também é afetada pelo tamanho médio de grão, podendo sofrer influências antagônicas conforme o meio em que o material é testado. Segundo Hamu *et al.*, (2009) o processamento do magnésio por SPD afeta tanto a microestrutura quanto a resistência à corrosão. Os contornos de grão agem como uma barreira que ajudam a passivar a superfície do material e dificultam o processo de corrosão (AUNG e ZHOU, 2010). Para avaliaram a influência do tamanho médio de grão na taxa de corrosão, Birbilis *et al,*. (2010) processaram amostras de magnésio por deformação plástica severa. Nesse estudo, foram realizados ensaios eletroquímicos de corrosão em amostras de magnésio com diferentes tamanhos médio de grão imersas em solução de 0,1 M de NaCl. Amostras cilíndricas de magnésio comercialmente puro Mg (> 99,9%) com 10 mm de diâmetro foram processadas por ECAP a uma temperatura de 250ºC em uma matriz com ângulo de intercessão entre canais de 90º com 10000 lb in^{-2} de pressão contrária, seguindo a rota de processamento $B_{C.}$ O material retirado do lingote apresentava um tamanho médio de grão de 125 µm que foi gradativamente sendo reduzido ao longo dos passes pela matriz de ECAP. Após

o primeiro passe, o tamanho médio de grão foi reduzido para 25 μm e, após o oitavo passe, ficou menor que 2,6 μm. Segundo os pesquisadores, para tentar determinar a influência do tamanho médio de grão na taxa de corrosão foi necessário utilizar o metal com elevado grau de pureza, para isolar os efeitos da composição química. Foi percebida uma redução na taxa de corrosão à medida que o tamanho médio de grão diminui, ou seja, o refino de grão aumenta a resistência à corrosão. Na figura 2.9 são apresentados os resultados dos ensaios eletroquímicos em um gráfico em que aparece plotada a corrente de corrosão em função do tamanho médio de grão.

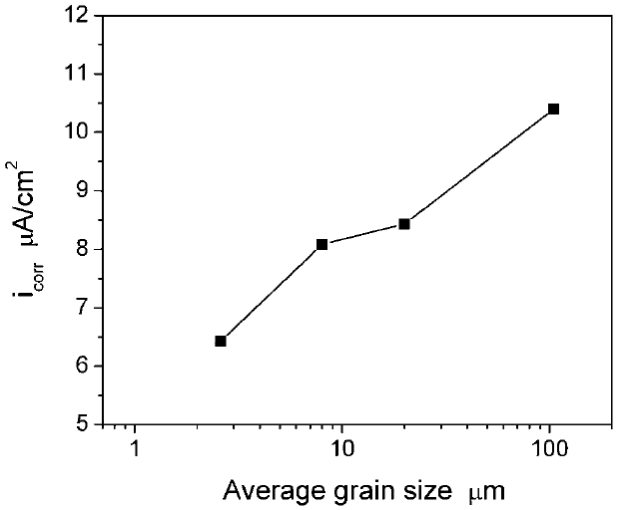

Figura 2.9 – Corrente de corrosão em função do tamanho médio de grão em solução de 0,1M de NaCl. Fonte: (BIRBILIS *et al*., 2010).

Para avaliar a influência das mudanças microestruturais na corrosão do magnésio comercialmente puro processado por ECAP, Song *et al.* (2010) fizeram testes de imersão com inspeção visual, medidas de perda de massa e testes eletroquímicos. Todos os experimentos foram realizados em solução de 3,5% de NaCl na temperatura ambiente. Foram ensaiadas amostras retiradas de um lingote em diferentes etapas de processamento, do material como recebido e após 1, 4 e 6 passes de ECAP. As figuras 2.10, 2.11 e 2.12 mostram a aparência das amostras após 1 min, 5 min e 2 h de imersão, respectivamente. Como pode ser visto na figura 2.10, o início da corrosão do magnésio comercialmente puro acontece por pite e resulta da dissolução do filme protetor. O nível de degradação do filme protetor pode ser avaliado pela quantidade e pelo tamanho dos pites formados. Para os diferentes tipos de amostra, o tamanho dos pontos de pite é similar, porém o número de pites formado inicialmente nas amostras processadas por

ECAP é maior se comparado com o material como recebido e esse número cresce juntamente com o número de passes de ECAP. Depois de 5 min de imersão, o tamanho dos pontos de pite aumenta e as amostras processadas por ECAP apresentam um maior aumento no tamanho dos pites que as amostras como recebidas, como mostra a figura 2.11.

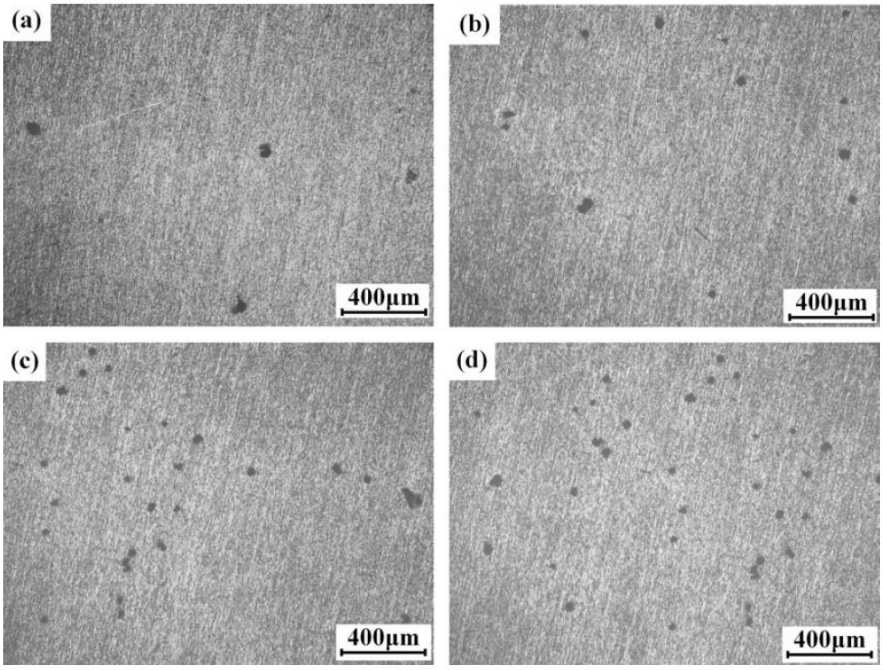

Figura 2.10 – Micromorfologia das amostras de magnésio mergulhadas em solução aquosa de NaCl a 3,5 wt.% após 1min de imersão: (a) como recebido; (b) após 1 passe; (c) 4 passes e (d) 6 passes de ECAP. Fonte: (SONG *et al*., 2010).

Depois de 5 min de imersão, o tamanho dos pites aumenta e as amostras processadas por ECAP apresentam um maior aumento no tamanho dos pites que as amostras como recebidas como mostra a Figura 2.11. Na Figura 2.12, é possível ver a macromorfologia das amostras após 2 h de imersão. As amostras processadas por ECAP apresentam mais áreas corroídas (áreas escuras) que a amostra como fundida evidenciando que as amostras processadas por ECAP possuem menor resistência à corrosão e uma tendência a sofrer corrosão preferencial nos contornos de grão.

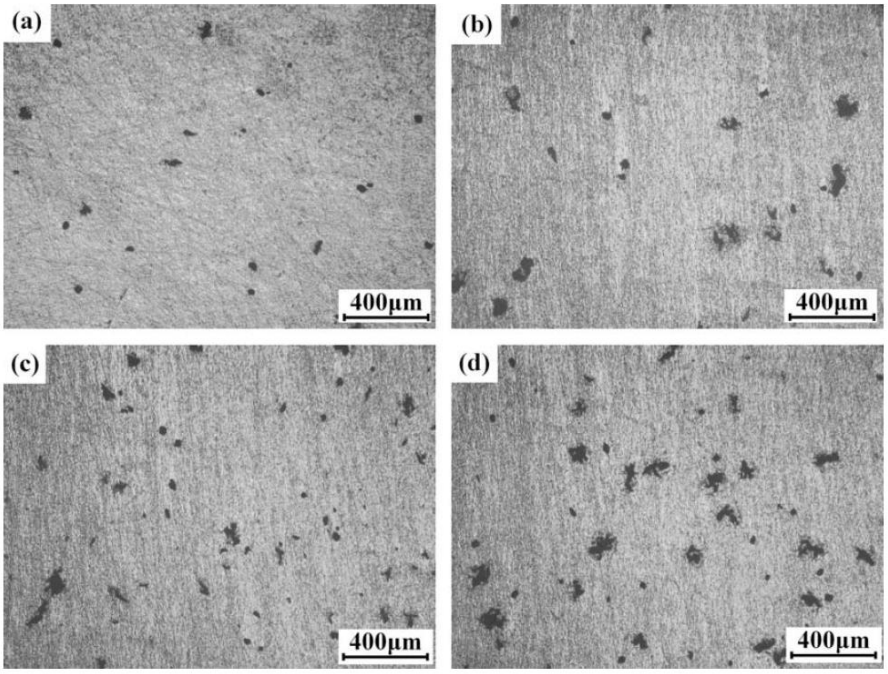

Figura 2.11 – Micromorfologia das amostras de magnésio mergulhadas em solução aquosa de NaCl a 3,5wt.% após 5min de imersão: (a) como recebido; (b) após 1 passe; (c) 4 passes e (d) 6 passes de ECAP.
Fonte: (SONG *et al*., 2010).

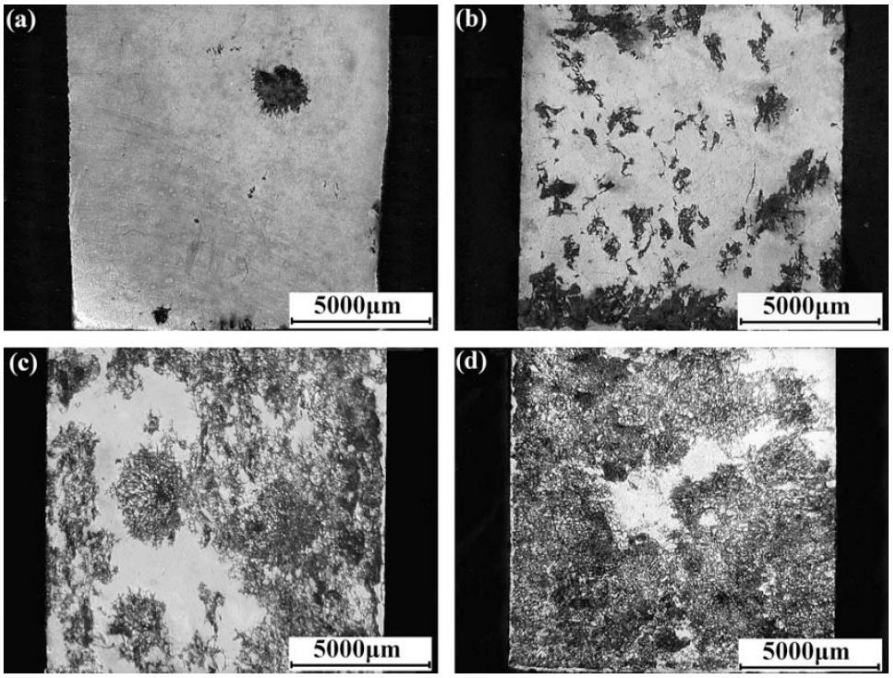

Figura 2.12 – Imagens ópticas macromorfológicas de amostras de magnésio como recebidas e processadas por ECAP, após imersão em solução aquosa de NaCl a 3,5 wt.% por 2h:
(a) como recebido; (b) após 1 passe; (c) 4 passes e (d) 6 passes de ECAP.
Fonte: (SONG et al., 2010).

Nesse mesmo trabalho, a taxa de corrosão expressa em perda de massa foi determinada para o material em etapas sucessivas do processamento por ECAP. Para efeito de comparação, também foi determinada a taxa de corrosão do material como recebido. A Figura 2.13Figura 2.13 ilustra a variação da taxa de corrosão com o tempo durante o teste de imersão das amostras de magnésio puro como recebidas e processadas por ECAP.

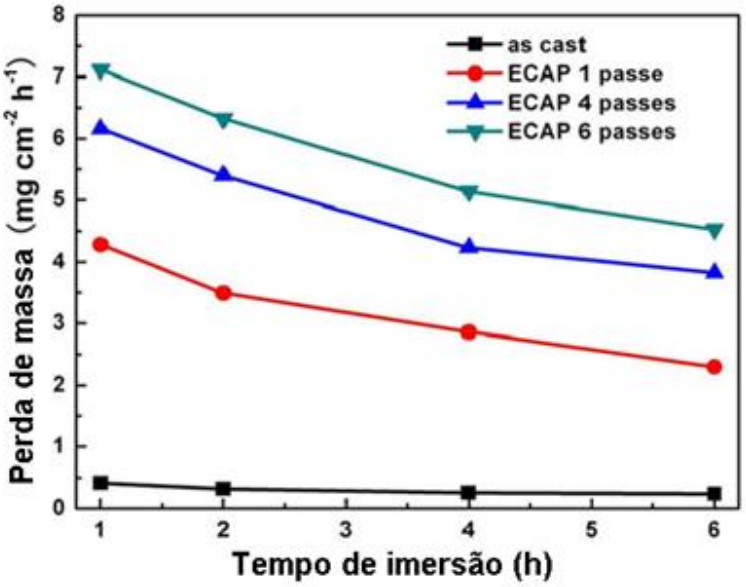

Figura 2.13 – Variação da taxa de perda de massa com o tempo para amostras de magnésio puro como recebidas e processadas por ECAP com diferentes número de passes pela matriz após imersão em solução de 3,5% de NaCl.
Fonte: (SONG *et al*., 2010).

Para avaliar a relação entre as taxas de corrosão do magnésio submetido a diferentes tipos de processamento, WANG *et al*, (2008) utilizaram amostras da liga AZ31 fundidas, amostras processadas por ECAP e amostras laminadas à quente identificadas como SC, ECAP e HR, respectivamente. Os ensaios de corrosão foram realizados em solução de Hank que simula parte da composição do plasma sanguíneo. A taxa de corrosão foi medida em massa por área superficial da amostra por tempo, os resultados foram convertidos em taxa de penetração em ($\mu m.d^{-1}$). A variação da taxa de corrosão com o tempo é apresentada na Figura 2.14.

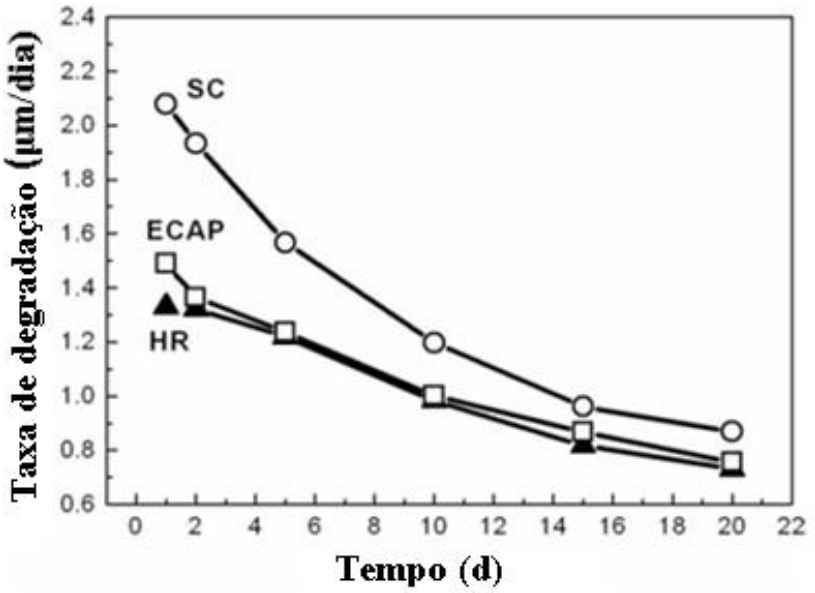

Figura 2.14 – Taxa de corrosão em solução de Hank de amostras da liga AZ31 submetidas a três tipos de processamento.
Fonte: (WANG *et al*., 2008).

Kim *et al.* (2014) avaliaram a influência do tamanho médio de grão na taxa de corrosão do magnésio comercialmente puro em solução de NaCl a 0,8 %. As amostras foram preparadas por moagem de alta energia seguida de sinterização por plasma pulsado. O tamanho médio de grão do pó de magnésio como recebido (atomizado) era de 600 µm e foi reduzido para 25 µm e 80 nm após 0,5 h e 20 h de moagem, respectivamente. Após 60 h de moagem, as amostram apresentavam um tamanho médio de grão maior que para 20 h. A corrente de corrosão foi determinada por meio de testes eletroquímicos utilizando o método de extrapolação de Tafel nas regiões lineares das curvas de polarização potenciodinâmica e a resistência de polarização foi determinada por ensaios de impedância eletroquímica. Os autores verificaram que a resistência de polarização diminui à medida que o tamanho médio de grão é reduzido. Na figura 2.15 são apresentados os resultados dos ensaios de impedância para diferentes tempos de imersão (a) após 0,5 h e (b) após 6 h. Também foi constatado que a corrente de corrosão aumenta à medida que o tamanho médio de grão diminui. A Figura 2.16 2.16 mostra a variação da corrente de corrosão i_{corr} com $d^{-0,5}$ (inverso da raiz quadrada do tamanho médio de grão).

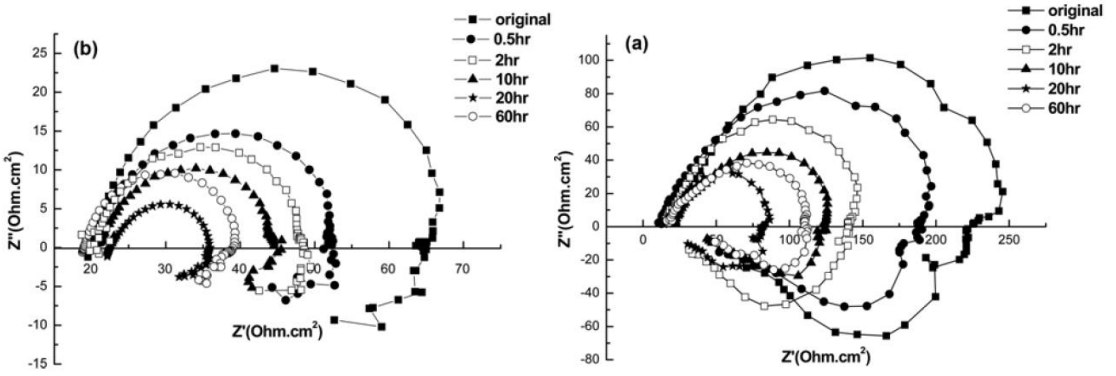

Figura 2.15 – Diagramas de impedância eletroquímica obtidos em diferentes tempos de imersão em NaCl. (a) após 0,5 h de imersão, (b) após 6 h de imersão.
Fonte: (KIM *et al*., 2014).

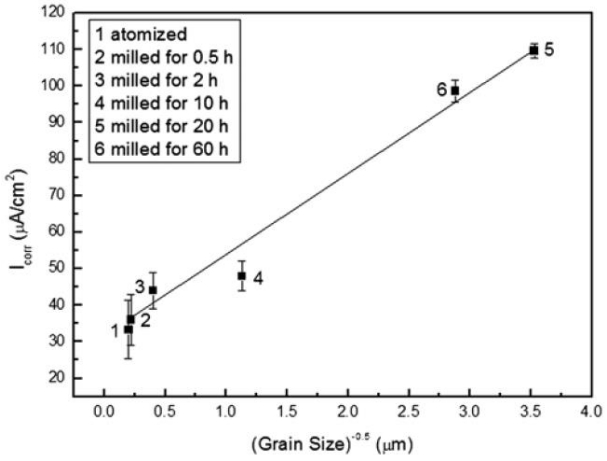

Figura 2.16 – Relação entre a corrente de corrosão e o tamanho médio de grão.
Fonte: (KIM *et al*., 2014).

Comparando os trabalhos que buscam elucidar a influência do tamanho médio de grão na taxa de corrosão do magnésio e suas ligas e tomando como exemplo resultados e as conclusões dos trabalhos de Birbilis *et al.* (2010) e Song *et al.* (2010) é possível notar uma contradição, pois, no primeiro caso, os pesquisadores concluíram que o refino de grão, causado pelo processamento por ECAP, diminui a corrente de corrosão ou seja aumenta a resistência a corrosão. Já no segundo, os pesquisadores concluíram que o processamento por ECAP diminui a resistência à corrosão. O comportamento pode variar conforme o meio em que o material é testado.

Ralston *et al.* (2010) analisaram os dados de vários trabalhos experimentais e propuseram uma explicação para os diferentes comportamentos apresentados. Segundo esses pesquisadores, para os metais com baixa taxa de corrosão (< 10μA.cm^{-2}) e com

algum grau de passivação em determinado meio, a resistência à corrosão aumenta com a redução do tamanho médio de grão. Um comportamento oposto, ou seja, a redução da resistência à corrosão com a redução do tamanho médio de grão é observado para metais que apresentam altas taxas de corrosão (> 10µA.cm^{-2}) e nenhum grau de passivação em determinado meio.

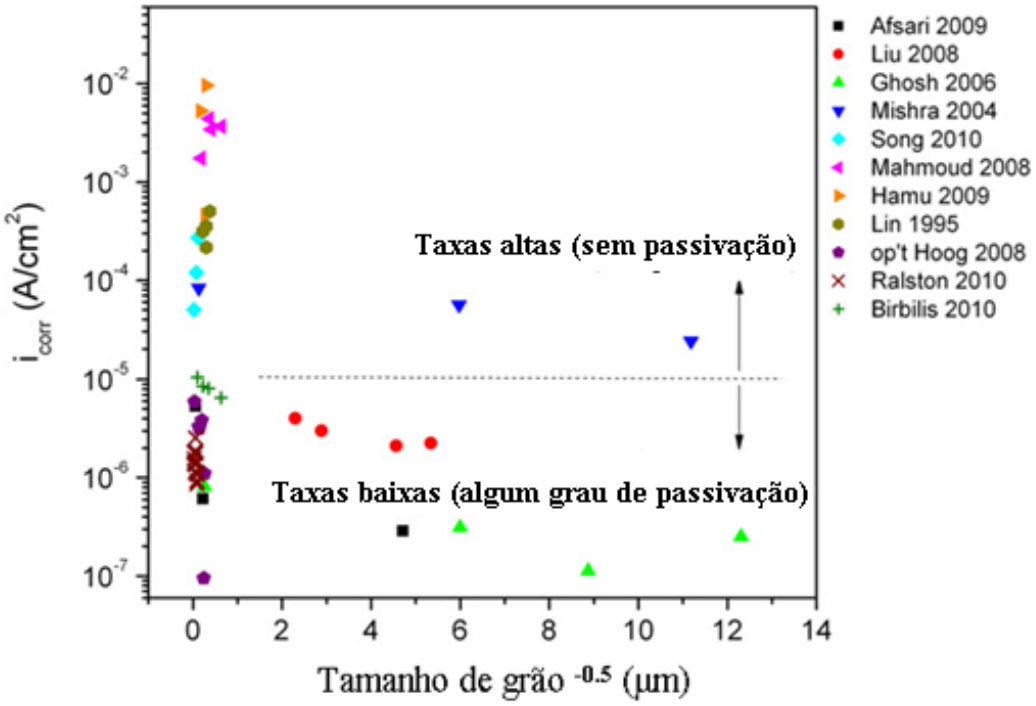

Figura 2.17 – O efeito do tamanho de grão na taxa de corrosão em diferentes materiais e meios. Os dados foram obtidos dos trabalhos seguintes:

Afshari *et al.* (2009) para o **Fe** em **10% NaOH**;

Liu and Duh (2008) para **$Ni_{50,5}Al_{49,5}$** em **0,9wt.% NaCl**;

Ghosh *et al.* (2006) para **Ni-Cu** em **3 wt.% NaCl desaerado**;

Mishra e Balasubramaniam (2004) para **Ni** em **1M H2SO4**;

Song *et al.* (2010) para **Mg (99,9%)** em **3,5 wt.% NaCl**;

Mahmoud *et al.* (2008) para **AA6063** em **1M HCl**;

Hamu *et al.* (2009) para **AZ31 Mg** em **3,5 wt. NaCl saturada com $Mg(OH)_2$ em pH 10,5**;

Lin *et al.* (1995) para **liga 600** em **sulfato ferrítico (31,25 g.l^{-1}) e 50% H_2SO_4**;

op´t Hoog *et al.* (2008) para **Mg (99,9%)** em **0,1M NaCl**;

Ralston *et al.* (2010) para **Al (99,999%)** em **0,1M NaCl**;

Birbilis *et al.* (2010) para **Mg (99,9%)** em **0,1M NaCl**

Fonte: (RALSTON *et al.*, 2010).

Na figura 2.17 são apresentados resultados de alguns trabalhos analisados por Ralston *et al.* (2010). Nas (Figura 2.18, 2.19 e 2.20) são apresentados os ajustes lineares feitos a partir dos dados experimentais analisados. A regressão linear foi feita para uma melhor visualização das tendências de aumento ou redução da resistência à corrosão com a redução do tamanho médio de grão.

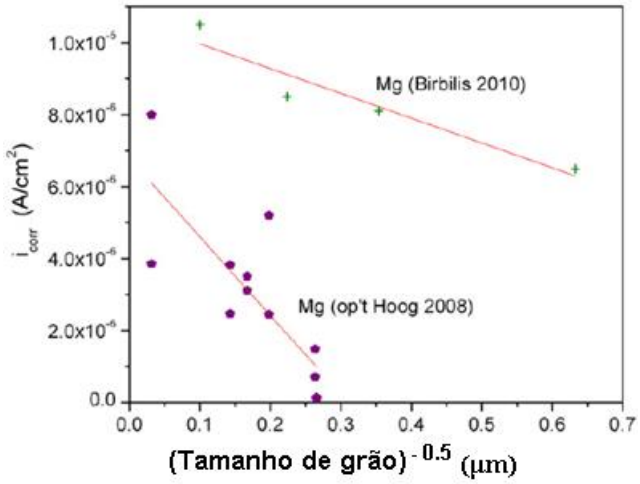

Figura 2.18 – Relação entre a corrente de corrosão (taxa de corrosão) e o tamanho médio de grão para correntes de corrosão baixas (amostras que apresentam certo grau de passivação).
Os dados foram extraídos dos trabalhos: Birbilis *et al.* (2010);op´t Hoog *et al.* (2008).
Fonte: (RALSTON *et al.*, 2010).

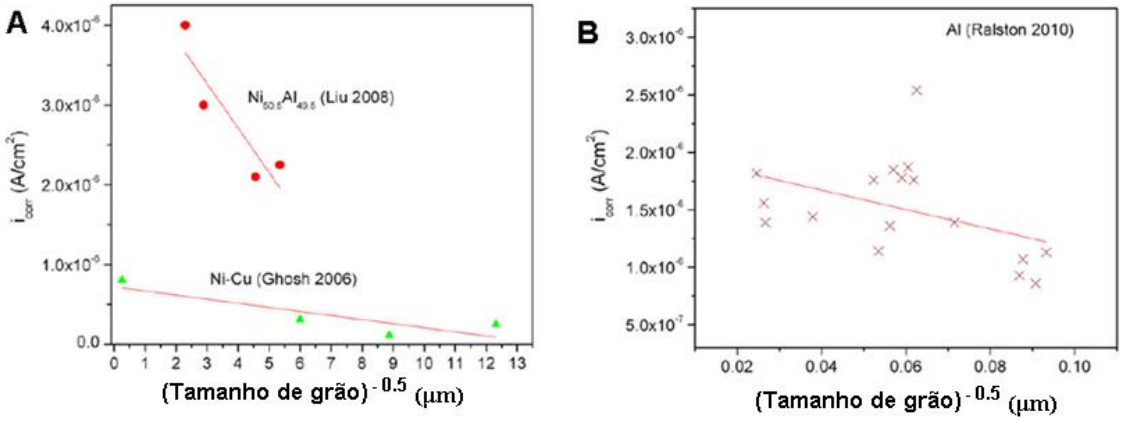

Figura 2.19 – (A) e (B) – Relação entre a corrente de corrosão (taxa de corrosão) e o tamanho médio de grão para correntes de corrosão baixas (amostras que apresentam certo grau de passivação).
Os dados foram extraídos dos trabalhos: Liu and Duh (2008); Ghosh *et al.* (2006); Ralston *et al.* (2010).
Fonte: (RALSTON *et al.*, 2010).

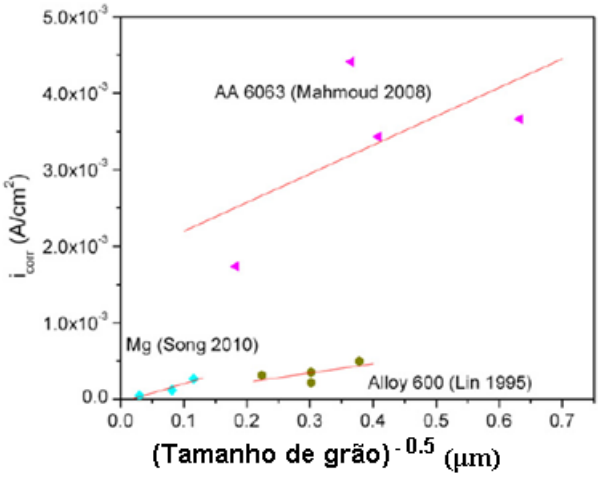

Figura 2.20 – Relação entre a corrente de corrosão (taxa de corrosão) e o tamanho médio de grão para correntes de corrosão altas (amostras que não apresentam passivação).
Os dados foram extraídos dos trabalhos: Mahmound *et al.* (2008); Song *et al.* (2010); Lin *et al.* (1995).
Fonte: (RALSTON *et al.*, 2010).

Na literatura é possível encontrar um grande número de trabalhos que avaliam a resistência à corrosão do magnésio e suas ligas, submetidos a diferentes tipos de processamento incluindo técnicas de SPD e imersos em diferentes meios. Para efeito de comparação são mostrados a seguir, de forma resumida, os resultados de alguns desses trabalhos. No sumário de dados de corrosão do magnésio e ligas, são apresentados os dados referentes à taxa de corrosão expressa em perda de massa e ou taxa de penetração e ou corrente de corrosão, extraídos da literatura. Também são descritos o tipo de material, o tipo de processamento, o meio corrosivo, o tempo de imersão e a temperatura.

Sumário de dados de corrosão do magnésio e ligas

Material	Processamento e tamanho médio de grão	Meio (eletrólito) e temperatura	Tempo de imersão e taxa de corrosão	Corrente de corrosão	Referência
3N-Mg (99,96%)	Lâmina injetada à quente	0,1 M NaCl a 25ºC	6,86 ($g.m^{-2}.h^{-1}$) 0,689 ($mg.cm^{-2}.h^{-1}$)	15,1 ($A.m^{-2}$) 1,51($mA.cm^{-2}$)	Hara *et al.* (2007)
6N-Mg (99,9999%)	Fundido	0,1 M NaCl a 25ºC	0,18 ($g.m^{-2}.h^{-1}$) 0,018 ($mg.cm^{-2}.h^{-1}$)	0,40 ($A.m^{-2}$) 0,040 ($mA.cm^{-2}$)	Hara *et al.* (2007)
AZ31B	Laminado à frio	0,1 M NaCl a 25ºC	0,24 ($g.m^{-2}.h^{-1}$) 0,024 ($mg.cm^{-2}.h^{-1}$)	0,53 ($A.m^{-2}$) 0,053 ($mA.cm^{-2}$)	Hara *et al.* (2007)
AZ91D	Laminado à frio	0,1 M NaCl a 25ºC	0,019 ($g.m^{-2}.h^{-1}$) 0,0019 ($mg.cm^{-2}.h^{-1}$)	0,042 ($A.m^{-2}$) 0,0042 ($mA.cm^{-2}$)	Hara *et al.* (2007)
AZ31	Squeeze cast	Solução de Hank´s + Glucose (pH7)	(1 dia) 2,08 ($\mu m.d^{-1}$) 0,35 ($mg.cm^{-2}.d^{-1}$) 0,0146 ($mg.cm^{-2}.h^{-1}$)	------	Wang *et al.* (2008)

AZ31	Laminado a quente	Solução de Hank´s + Glucose (pH7)	(1 dia) 1,3 (µm.d^{-1}) 0,12 (mg.cm^{-2}.d^{-1}) 0,005 (mg.cm^{-2}.h^{-1}) (20 dias) 0,74 µm.d^{-1} 0,12 (mg..cm^{-2}.d^{-1}) 0,005 (mg.cm^{-2}.h^{-1})	------	Wang *et al*. (2008)
AZ31	ECAP, taxa 5mm/min 4 passes, 200ºC, rota C	Solução de Hank´s + Glucose (pH7)	(1 dia) 1,5 (µm.d^{-1}) 0,12 (mg.cm^{-2}.d^{-1}) (20 dias) 0,74 µm.d^{-1} 0,12 (mg.cm^{-2}.d^{-1})	------	Wang *et al*. (2008)
Mg (99,9%)	Fundido (800-1500) µm	NaCl 3,5wt.% a 25ºC	(1 hora) 0,4 (mg.cm^{-2}.h^{-1}) (6 horas) 0,3 (mg.cm^{-2}.h^{-1})	0,05 (mA.cm^{-2})	Song *et al*. (2010)
Mg (99,9%)	ECAP Φ=90º, taxa 0,5mm.s^{-1} 1 passe, T = 300ºC, (100-200) µm	NaCl 3,5wt.% a 25ºC	(1 hora) 4,3 (mg.cm^{-2}.h^{-1}) (6 horas) 2,3 (mg.cm^{-2}.h^{-})	0,12 (mA.cm^{-2})	Song *et al*. (2010)

Mg (99,9%)	ECAP Φ=90º, taxa 0,5mm.s^{-1} 4 passes, 300ºC, rota C (----------) µm	NaCl 3,5wt.% a 25ºC	(1 hora) 6,2 (mg.cm^{-2}.h^{-1}) (6 horas) 4,1 (mg.cm^{-2}.h^{-1})	0,19 (mA.cm^{-2})	Song *et al*. (2010)
Mg (99,9%)	ECAP Φ=90º, taxa 0,5 mm.s^{-1} 6 passes, 300ºC, rota C (50-100) µm	NaCl 3,5 wt.% a 25ºC	(1 hora) 7,2 (mg.cm^{-2}.h^{-1}) (6 horas) 4,8 (mg.cm^{-2}.h^{-1})	0,27 (mA.cm^{-2})	Song *et al*. (2010)
Mg (99,9%)	----------	1N NaCl (pH6)	50 (mg.cm^{-2}.d^{-1}) 2,08 (mg.cm^{-2}.h^{-1})	------	Song *et al*. (2001)
Mg (99,9%)	----------	1N NaCl (pH11)	32 (mg.cm^{-2}.d^{-1}) 1,33 (mg.cm^{-2}.h^{-1})	------	Song *et al*. (2001)
Mg (99,9%)	----------	1N Na(OH)	0,03 (mg.cm^{-2}.d^{-1}) 0,001 (mg.cm^{-2}.h^{-1})	------	Song *et al*. (2001)
Mg (99,9%)	----------	1N HCl	63 (g.cm^{-2}.d^{-1}) 2,63 (mg.cm^{-2}.h^{-1})	------	Song *et al*. (2001)
Mg (99,9%)	----------	5% NaCl	16 (mg.cm^{-2}.d^{-1}) 0,67 (mg.cm^{-2}.h^{-1})	------	Song *et al*. (2001)
AZ21	----------	1N NaCl (pH11)	0,31 (mg.cm^{-2}.d^{-1}) 0,013 (mg.cm^{-2}.h^{-1})	------	Song *et al*. (2001)

AZ91D diecast	----------	1N NaCl (pH11)	3 ($mg.cm^{-2}.d^{-1}$) 0,125 ($mg.cm^{-2}.h^{-1}$)	------	Song *et al*. (2001)
Mg (>99,9%)	Fundido (125 - 1000) µm	0,1M NaCl a 25ºC	----------	11 ($\mu A.cm^{-2}$) 0,011 ($mA.cm^{-2}$)	Birbilis *et al*. (2010)
Mg (> 99,9%)	ECAP1 passe, 250ºC Pressão contrária 10000 $lb.in^{-2}$ (~25) µm	0,1M NaCl a 25ºC	----------	~ 8,5 ($\mu A.cm^{-2}$) 0.0085 ($mA.cm^{-2}$)	Birbilis *et al*. (2010)
Mg (> 99,9%)	ECAP 4 passe, 250ºC, rota B_C Pressão contrária 10000 $lb.in^{-2}$ (~8) µm	0,1M NaCl a 25ºC	----------	~ 8 ($\mu A.cm^{-2}$) 0.008 ($mA.cm^{-2}$)	Birbilis *et al*. (2010)
Mg (> 99,9%)	ECAP 8 passe, 250ºC, rota B_C Pressão contrária 10000 $lb.in^{-2}$ (~2,6) µm	0,1M NaCl a 25ºC	----------	~ 6 ($\mu A.cm^{-2}$) 0.006 ($mA.cm^{-2}$)	Birbilis *et al*. (2010)

Mg (99,97%)	Fundido (~1000) µm	HBSS a 37,4ºC	(5 min.) 1,64 (mm/ano)	~ 71,78 (µA.cm^{-2}) 0.0718 (mA.cm^{-2})	Saha *et al*. (2015)
Mg – 0,25Zr	Fundido (~425) µm	HBSS a 37,4ºC	(5 min.) 0,31 (mm/ano)	~ 13,71 (µA.cm^{-2}) 0.0137 (mA.cm^{-2})	Saha *et al*. (2015)
Mg – 1Zr	Fundido (~80) µm	HBSS a 37,4ºC	(5 min.) 0,11 (mm/ano)	~ 4,87 (µA.cm^{-2}) 0.0049 (mA.cm^{-2})	Saha *et al*. (2015)

2.4 O uso do magnésio como material biodegradável

O surgimento de uma nova classe de materiais biodegradáveis então chamados de metais biodegradáveis BMs (*biodegradable metals*) quebrou o paradigma de que os biomateriais metálicos deveriam apresentar uma elevada resistência à corrosão em meio corporal (ZHENG *et al.*,2014). O termo metal biodegradável é definido como metal que sofre corrosão gradual *in vivo*, com uma resposta fisiológica apropriada desencadeada pelos produtos da corrosão, sem deixar resíduos. Sendo assim, os principais componentes de um BM devem ser elementos que possam ser metabolizados pelo corpo humano, e que, em meio fisiológico, possuam taxas e mecanismos de degradação apropriados (ZHENG *et al.*,2014).

Para uso em implantes biológicos é essencial que o material tenha uma biocompatibilidade adequada e que, portanto, seja capaz de executar uma função específica no organismo hospedeiro com uma resposta fisiológica satisfatória (WITTE *et al.*, 2008). Os testes de citotoxidade são indicadores preliminares para avaliar a biocompatibilidade das ligas. Teoricamente todos os metais apresentam uma dosagem limite acima da qual apresentam algum grau de toxidade no corpo humano. A biocompatibilidade das ligas é influenciada pela taxa de liberação dos íons metálicos que por sua vez tem relação com a taxa de corrosão no meio em que essas ligas serão utilizadas. O magnésio é um metal que reconhecidamente apresenta uma boa biocompatibilidade no corpo humano, entretanto níveis de magnésio no sangue superiores a 1 $mmol.L^{-1}$, podem desencadear reações fisiológicas como: paralisia muscular, hipotensão e desconforto respiratório. Em situações extremas o magnésio em níveis sanguíneos severamente altos de 6-7 $mmol.L^{-1}$ pode causar parada cardíaca (STAIGER *et al.*, 2006).

A influência dos elementos (X= Al, Ag, In, Mn, Si, Sn, Y, Zn and Zr) na citotoxidade das ligas binárias de magnésio Mg – 1X (wt.%) contendo 99 wt.% de magnésio e 1 wt.% de elemento de liga foi avaliada por Gu *et al.*, (2008) . Os testes de citotoxidade indicaram que os extratos feitos a partir das ligas Mg-1Al, Mg-1Sn e Mg-Zn não causaram uma redução significativa na viabilidade celular em fibroblastos (L-929 e NIH3T3) e os extratos das ligas Mg–1Al, Mg–1Si, Mg–1Sn, Mg–1Y, Mg–1Zn e

Mg–1Zr não indicaram nenhum comportamento citotóxico em células de osteoblastos (MC3T3-E1).

Testes de citoxidade de ligas de magnésio WE43, WZ21 e ZW21 aparecem descritos no trabalho de Hänzi *et al.*, (2010). Foram realizados testes do tipo indireto utilizando extratos produzidos a partir da imersão do material em uma solução de fluído corporal simulado. Após a imersão esse extrato foi adicionado em diferentes quantidades às culturas de célula. Foram realizadas medidas da viabilidade e da atividade metabólica das células em contato com diferentes quantidades de extratos das três ligas de magnésio e soluções de controles positivo e negativo. A partir dos resultados obtidos figura 2.21 é possível inferir que a viabilidade e a atividade metabólica das células diminuem quando o volume de extrato adicionado é superior a 20µl para as ligas ZW21 e WZ21. De maneira similar também podemos observar que para a liga WE43 e para o controle SBF (Negativo) a viabilidade e a atividade metabólica das células diminuem quando o volume de extrato adicionado é superior a 100 µl. Dentre as ligas de magnésio avaliadas a que apresenta melhor biocompatibilidade é a liga WE43, pois para esse material a taxa de queda da viabilidade e metabolismo celular é menor que para as outras duas ligas.

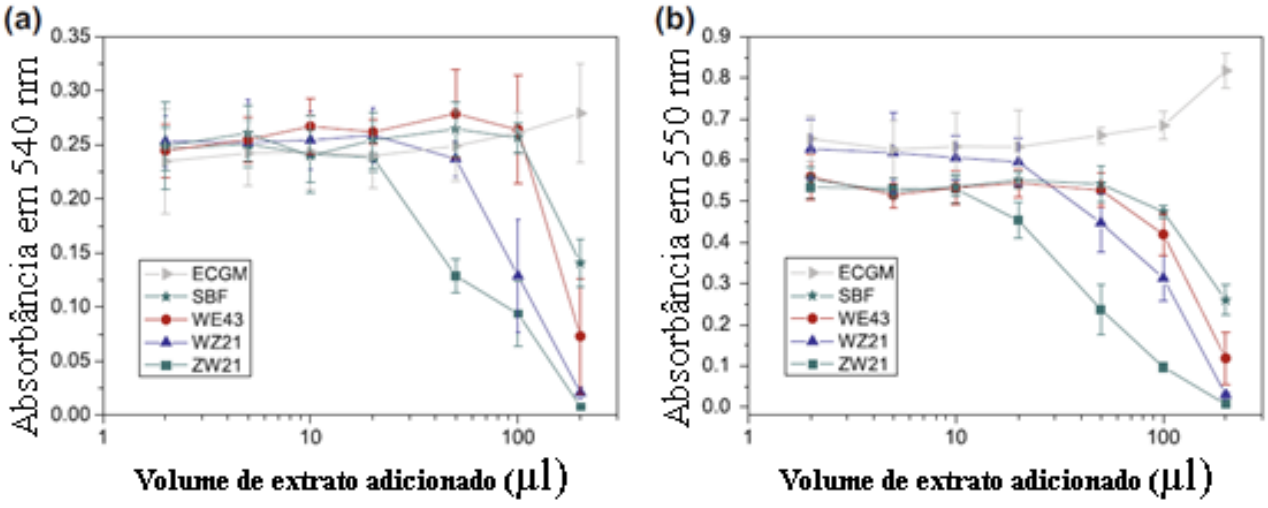

Figura 2.21 – Citotoxidade indireta após 7 dias: a) viabilidade e b) atividade metabólica. Vários volumes de extrato (2, 5, 10, 50, 100 e 200 µl) das ligas ZW21, WZ21, WE43 e controles SBF (T) e ECGM foram adicionados a 500 µl do meio de cultura das células.
Fonte: (HÄNZI *et al.*,2009).

2.5 Referências Bibliográficas

Valiev, R. Z.; Langdon, T. G. Principles of equal-channel angular pressing as a processing tool for grain refinement. Progress in Materials Science. V. 51, p. 881-981, 2006.

Segal, V.M. A materials processing by simple shear. Materials Science and Engeneering A. v. 197, p. 157-164, 1995.

Valiev, R. Nanostructuring of metals by severe plastic deformation for advanced properties. Nature Materials, V. 3, p. 551-516, 2004.

Poggiali, F. S. J.; Silva, C. L. P.; Pereira, P. H. R.; Figueiredo, R. B. Cetlin, P. R. Determination of mechanical anisotropy of magnesium processed by ECAP. Journal of Materials research and Technology, V. 3, P. 331-337, 2014.

Figueiredo, R. B.; PereirA, P.H.R.; AguilaR, M.T.P.; Cetlin, P.R.; Langdon, T.G. Using finite element modeling to examine the temperature distribution in quasi-constrained high-pressure torsion. Acta Materialia. V.60, p. 3190-3198, 2012.

Sharman, K., Bazarnik, P., BrynK, T., Bulutsuz, A. G., Lewandowska, M., Huang, Y., & Langdon, T. G. Enhancement in mechanical properties of a β-titanium alloy by high-pressure torsion. Journal of Materials Research and Technology, v. 4, n. 1, p. 79-83, 2015.

Harai, Y.; Kai, M.; Kanelo, K.; Horita, K.; Langdon, T. G. Microstructural and Mechanical Characteristics of AZ61 magnesium alloy processed by high-pressure torsion. Materials Transactions, V. 49, p. 76-83, 2008.

McCafferty, E. Introduction to corrosion science. New York: Springer, 2010, 576 p.

Mordike, B. L.; Ebert, T. Magnesium: Properties – applications – potential. Materials Science and Engineering A. V.302, p. 37–45, 2001.

Song, G.; Atrens, A. Understanding magnesium corrosion. Advanced Engineering Materials. V. 12, p. 837–858, 2003.

Birbilis, N.; Ralston, K.D.; Virtanen, S.; Fraser, H.L.; Davies, H.J. Grain character influences on corrosion of ECAPed pure magnesium. Corrosion Engineering, Science and Technology. V.45, p.224-230, 2010.

Song, D.; Ma, A.B.; Jiang, J.H.; Lin, P.H.; Yang, D.H.; Fan, J.F. Corrosion behaviour of equal-channel-angular-pressed pure magnesium in NaCl aqueous solution. Corrosion Science. V.52, p.481-490, 2010.

Zhao, M.; Schmutz, P.; Brunner, S.; Liu, M.; Song, G.; Atrens, A. An exploratory study of the corrosion of Mg alloys during interrupted salt spray testing. Corrosion Science. V. 51, p. 1277-1292, 2009.

Shi, Z.; Liu, M.; Atrens, A. Measurement of the corrosion rate of magnesium alloys using Tafel extrapolation. Corrosion science. V.52, p.579–588, 2010.

Song, G.; Atrens, A.; StJohn, D. An hydrogen evolution method for estimation of the corrosion rate of magnesium alloys. Magnesium Technology. Ed. John N. Hryn, TMS, p. 255–262, 2001.

Hagihara, K., Okubo, M., Yamasaki, M., Nakano, T. Crystal-orientation-dependent corrosion behaviour of single crystals of a pure Mg and Mg-Al and Mg-Cu solid solutions. Corrosion Science, 109, 68–85, 2016.

Zhao, Y.; HuanG, G.; Wang, G.; Han, T.; Pan, F. Influence of Grain Orientation on the Corrosion Behavior of Rolled AZ31 Magnesium Alloy. Acta Metallurgica Sinica (English Letters). V. 8, P. 1387-1393, 2015.

Hamu, G.; Eliezer, D.; Wagner, L. The relation between severe plastic deformation microstructure and corrosion behavior of AZ31 magnesium alloy. Journal of Alloys and Compounds. V. 468, p. 222, 2009.

Aung, N. N.; Zhou, W. Effect of grain size and twins on corrosion behavior of AZ31B magnesium alloy. Corrosion Science, V. 52(2), p. 589-594, 2010.

Wang, H.; Estrin, Y.; Fu, H.; Song, G.; Zuberová, Z. Bio-corrosion of a magnesium alloy with different processing histories. Materials Letters. V.62, p.2476-2479, 2008.

Kim, K. R.; Ahn, J. W.; Kim, J. H.; Han, J. H.; Cho, K. K.; Roh, J.; Kim, W. J.; Kim, H. S. Corrosion behavior of magnesium fabricated by high-energy ball milling and spark plasma sintering. Met. Mater. Int. V. 20, p. 1095-1101, 2014.

Ralston, K. D.; Birbilis, N.; Davies, C. H. J. Revealing the relationship between grain size and corrosion rate of metals. Scripta Materialia. V.63, p.1201–1204, 2010.

Hara, N.; Kobayashi, Y.; Kagaya, D,; Akao, N. Formation and breakdown of surface films on magnesium and its alloys in aqueous solutions. Corrosion Science. V.49, p. 166-175, 2007.

Saha, P.; Roy, M.; Datta, M. K.; Lee, B.; Kumta, P. N. Effects of grain refinement on the biocorrosion and vitro bioactivity of magnesium. Materials Science and Engeneering C. V.57, p.294-303, 2015.

Zheng, Y. F.; Gu, X. N., Witte, F. Biodegradable metals. Materials Science and Enginnering R. V. 77, p. 1-34, 2014.

Witte, F., Hort, N., Vogt, C., Cohen, S., Kainer, K. U., Willumeit, R., Feyerabend, F. Degradable biomaterials based on magnesium corrosion. Current Opinion in Solid State and Materials Science, V. 12, p. 63-72, 2008.

Staiger, M. P.; Pietak, A. M.; Huadmai, J.; Dias, G. Magnesium and its alloys as orthopedic biomaterials: a review. Biomaterials. V. 27, p. 1728–34, 2006.

Gu, X.; Zheng, Y.; Cheng, Y.; Zhong, S.; Xi, T. In vitro corrosion and biocompatibility of binary magnesium alloys. Biomaterials V.30, p. 484-498, 2008.

Hänzi, A. C.; Gerber, I.; Schinhammer, M.; Löffler, J. F.; Uggowitzer P. J. On the in vitro and in vivo degradation performance and biological response of new biodegradable Mg–Y–Zn alloys. Acta Biomaterialia. V.6, p. 1824–1833, 2010.

3. CAPÍTULO 3 – MICROSTRUCTURE AND HARDNESS EVOLUTION IN MAGNESIUM PROCESSED BY HPT

Cláudio L. P. Silva[1], Isabela C. Tristão[2], Shima Sabbaghianrad[3], Seyed A. Torbati-Sarraf[3], Roberto B. Figueiredo[4,*], Terence G. Langdon[5]

[1]Department of Metallurgical and Materials Engineering, Universidade Federal de Minas Gerais, Belo Horizonte 31270-901, Brazil

[2]Department of Mechanical Engineering, Universidade Federal de Minas Gerais, Belo Horizonte 31270-901, Brazil

[3]Departments of Aerospace and Mechanical Engineering & Materials Science, University of Southern California, Los Angeles, CA 90089-1453, U.S.A.

[4]Department of Materials Engineering and Civil Construction, Universidade Federal de Minas Gerais, Belo Horizonte 31270-901, Brazil

[5]Materials Research Group, Faculty of Engineering and the Environment, University of Southampton, Southampton SO17 1BJ, UK

[*]Corresponding author: figueiredo@demc.ufmg.br

Abstract

High pressure torsion provides an opportunity to process materials with low formability such as magnesium at room temperature. The present work shows the microstructure evolution in commercially pure magnesium processed using a pressure of 6.0GPa up to 10 turns of rotation. The microstructure evolution is evaluated using electron microscopy and the hardness is determined using dynamic hardness testing. The results show that the grain refinement mechanism in this material differs from materials with b.c.c. and f.c.c. structures. The mechanism of grain refinement observed at high temperatures also applies at room temperature. The hardness distribution is heterogeneous along the longitudinal section of the discs and is not affected by the amount of deformation imposed to the material.

Keywords: high-pressure torsion; magnesium; EBSD

3.1 Introduction

High-pressure torsion (HPT)[1, 2]is a metal processing technique in which a sample is subjected to torsion under elevated pressure. The pressure leads to high hydrostatic compressive stresses and severe plastic deformation is introduced by torsion increasing significantly the amount of crystalline defects in the material structure. Thus, a high dislocation density and an increased area of grain boundaries are observed in processed metallic materials leading to high strength and refined grain structures.

High pressure torsion has been widely used to process magnesium and its alloys at room temperature despite their low formability. Many papers have reported the formation of ultrafine grained structures in pure magnesium [3-6] and AZ31 [7-11], AZ61 [12], AZ80 [13], AZ91 [14-16], ZK60 [17-19], Mg-Zn-Y [20, 21], Mg-Gd-Y-Zr[22, 23], Mg-Zn-Ca [24-27] and Mg-Dy-Al-Zn-Zr[28]alloys. The processed alloys exhibit improved strength but also some papers report superplastic behaviour [16, 19, 22, 29, 30], improved hydrogen storage properties [3, 31-35] and improved corrosion resistance [24, 27, 36].

Formation of ultrafine grained structures and improved strength are also observed in other metallic materials processed by HPT. However, the evolution of the microstructure and the distribution of hardness in processed discs of magnesium and its alloys seem to differ from other f.c.c. and b.c.c. materials.It is expected that the amount of strain imposed to the disc during HPT processing is proportional to the distance from the center due to the torsional deformation. Thus, hardness variations along the sample radius are expected in the early stage of processing when the material has not reached hardness saturation. However, the amount of strain and the hardness are not expected to vary along the sample thickness and this has been confirmed by experiments in pure aluminium [37, 38] and iron[39]. Minor variations in distribution of strain along the sample

thickness has been predicted by finite element modelling [40, 41] due to friction and variations in hardness distribution have been reported in samples with low diameter to thickness ratio [39, 42]. However, experiments have shown significant heterogeneity in hardness distribution along the disc thickness in a magnesium alloy in samples with high diameter to thickness ratio[43, 44].

Moreover, it is known that the high amount of defects introduced by plastic deformation leads to the formation of low angle boundaries in the early stage of processing and the misorientation of these boundaries increase with continuing processing. Therefore, a large fraction of low angle boundaries are expected in the early stage of HPT processing and a gradual transition towards a larger fraction of high angle boundaries is expected at later stages. This has been confirmed by experiments in aluminium [45, 46] and in pure iron [47]. However, the mechanism of grain refinement in magnesium and its alloys differs from f.c.c. and b.c.c. materials. A mechanism in which new refined grains are formed along coarse grains boundaries has been proposed [48-50] based on experimental evidence of microstructure evolution for high temperature processing.

The understanding of the distribution of plastic deformation and evolution of structure during HPT processing is of key importance to future production of components of magnesium alloys with superior strength, superplastic properties, enhanced hydrogen storage kinetics or improved corrosion resistance. The present paper aims to clarify the distribution of hardness along the disc longitudinal plane using dynamic hardness measurements at different stages of HPT processing and to determine the evolution of grain boundary misorientation distribution.

3.2 Experimental material and procedures

The material used in the present work was commercial purity magnesium provided by RIMA (Bocaiúva / Brazil) as a cast slab. The material was machined into a billet with 10 mm diameter and 100 mm length. Discs with 1 mm thickness were cut using a low speed diamond coated saw and were ground to ~0.85 mm thickness using abrasive papers.

The discs were processed by HPT using quasi-constrained anvils and a nominal pressure of 6.0GPa. The rotation rate was 1 rpm which is expected to lead to ~10 K temperature rise during processing (considering a flow stress of 200 MPa) [51, 52]. Discs were processed to 1/8, 1/2, 2 and 10 turns.

The distribution of hardness was determined on the longitudinal section of the discs. A low speed diamond coated saw was used to cut the discs and the samples were mounted using room temperature curing resin. The samples were ground and polished to a mirror-like finish. Figure 1 illustrates the section and the location of indentations. A Shimadzu DUH-211s dynamic hardness tester with a Berkovich indenter was used for testing. The maximum applied load was 200 mN, the loading rate was ~70 mN/s and the dwell time was set to 0 s in order to avoid room temperature creep which has been shown to take place in magnesium processed by HPT [6]. The values of hardness were plotted as colour coded maps as a function of the indentation position. Also, the average hardness for indentations at similar distance from the center were plotted as a function of the effective strain which was determined by the following equation [53, 54].

$$\varepsilon = \frac{2\pi N r}{t\sqrt{3}} \qquad (1)$$

where N is the number of turns, r is the distance to the center and t is the sample thickness.

The microstructure was determined at mid-radius position (see Fig. 3.1) using EBSD. The samples were polished to a mirror-like finish using diamond paste and the final polishing step used colloidal silica in a Vibromet equipment. The equipment used for EBSD characterization was a JEOL JSM-7001F scanning electron microscope operating at 7 kV. The step size was 0.1 μm. The images were cleaned up using grain confidence index (CI) standardization, neighbor CI correlation and grain dilation procedures.

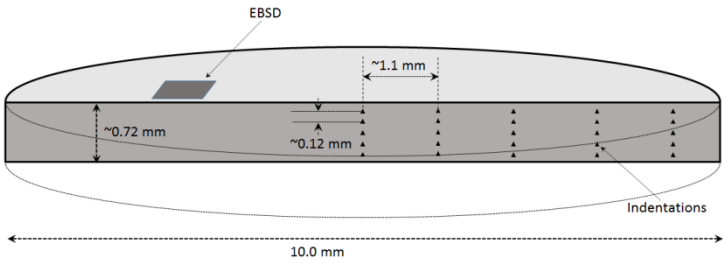

Figure 3.1 – Illustration of the section used for hardness testing, location of indentations and the location for EBSD characterization of the microstructure.

3.3 Results and discussion

3.3.1 Microstructure

Figure 3.2 shows representative images of the grain structure of samples processed by 1/8, 1/2 and 10 turns of HPT. Different colours are used to set apart low angle (red) and high angle (black) boundaries. Grains sizes with over one order of magnitude difference are clearly observed in the sample processed by 1/8 turn. The smaller grains are typically located between coarse grains suggesting they are formed along grain boundaries. The microstructure of the material processed by 1/2 turn exhibits grains with different sizes although the size difference between the small and coarse grains is reduced significantly. Also, the area fraction occupied by the coarse grains decreased significantly by comparison to the material processed by 1/8 turn.Finally, the microstructure of the material processed by 10 turns of HPT continues to exhibit a few coarse grains although it is apparent that the area fraction of the coarse grains is

reduced. This is in agreement with transmission electron microscopy characterization of magnesium processed by HPT in which some coarser grains are observed in the microstructure even after multiple turns of processing [3, 6, 55]. Therefore, a mix of ultrafine grains and grains with a few microns of diameter seems to be a stable microstructure in pure magnesium processed by HPT.

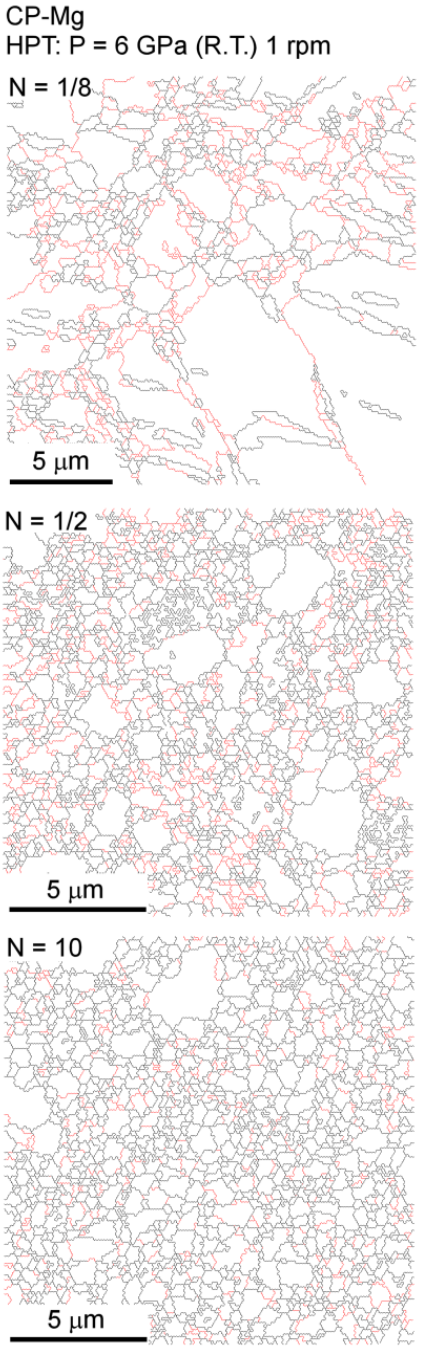

Figure 3.2 – Distribution of low angle (red) and high angle (black) boundaries in samples processed by 1/8, 1/2 and 10 turns of HPT.

In order to determine the area fraction occupied by coarse and fine grains at the different stages of processing, the cumulative distribution of grain sizes in samples processed by 1/8, 1/2 and 10 turns of HPT is shown in Fig. 3.3. It is observed that most of the microstructure is composed of grains larger than 1 micron in the sample processed by 1/8 turn. Processing to 1/2 turn increases significantly the area occupied by ultrafine grains and decreases the size of the largest grains. Further processing up to 10 turns does not change the distribution of the very fine grains (<0.6 μm) but increased the fraction of grains in the range 0.6 μm ~ 1.0 μm and reduced the fraction of coarser grains. This is in agreement with the trend observed in magnesium processed by Equal-Channel Angular Pressing at high temperatures in which the new grains nucleate along grain boundaries and slowly consume the coarse grains [48-50].

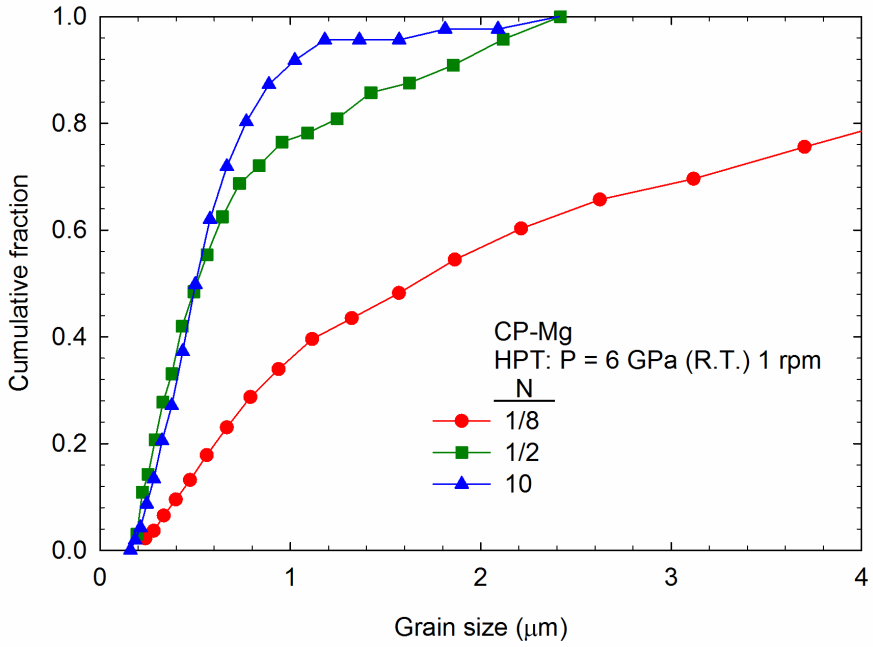

Figure 3.3 – Cumulative fraction of grain sizes at different stages of processing.

Figure 3.4 shows the distribution of misorientation angles of the grain boundaries for the different samples. A large fraction (~0.41) of grain boundaries exhibit misorientations lower than 15º after only 1/8 turn but the frequency of low angle boundaries is decreased significantly after only 1/2 turn (~0.27). An additional decrease in frequency of low angle boundaries is observed after 10 turns which ultimately stabilizes in ~0.15. The frequency of low angle boundaries in magnesium is

significantly lower than observed in other metallic materials [46, 47]. It is also worth noting a peak of frequency of boundaries between 85º ~ 90º which is associated with twinning [56] and a peak at ~30º which is associated with a basal texture [57].

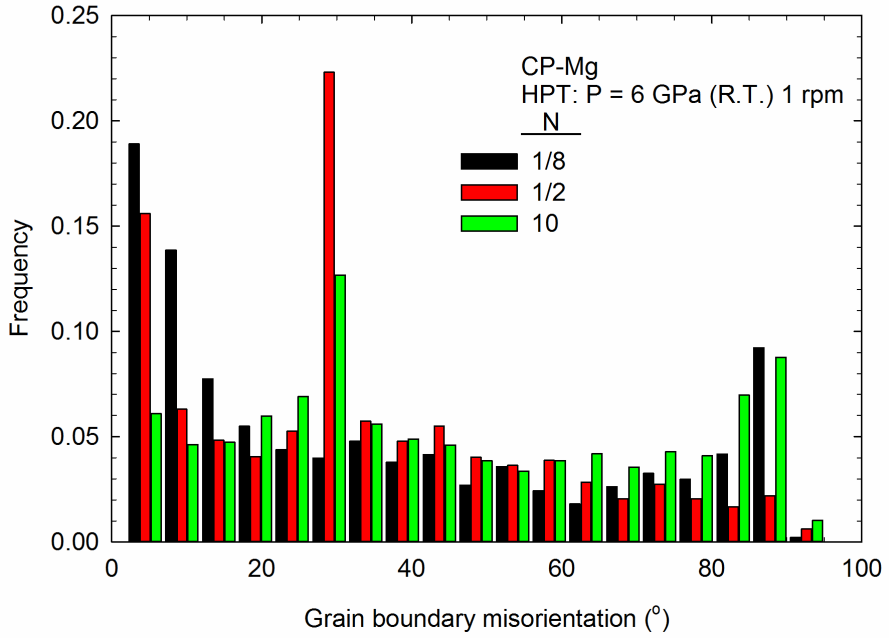

Figure 3.4 – Frequency distribution of misorientation angles of grain boundaries.

3.3.2 Hardness

Figure 3.5 shows colour-coded distribution of hardness at the longitudinal sections of samples processed to 1/8, 1/2, 2 and 10 turns of HPT. It is observed that the hardness does not vary notably with the distance from the center and also does not vary with the number of turns although the amount of plastic strain imposed to the material by torsion increases linearly with increasing distance from the center and with the number of turns. The hardness maps show substantial variations in hardness without a clear trend. Areas with low hardness (~50 kgf mm^{-2}) and areas with high hardness (~65 kgf mm^{-2}) are observed throughout the longitudinal sections of the samples at the different stages of processing. This heterogeneous distribution of hardness differs from reports in pure aluminum[38] and in pure iron [39] where homogeneous distributions of hardness have been reported along the sample thickness and a clear trend is observed at different distances from the center.

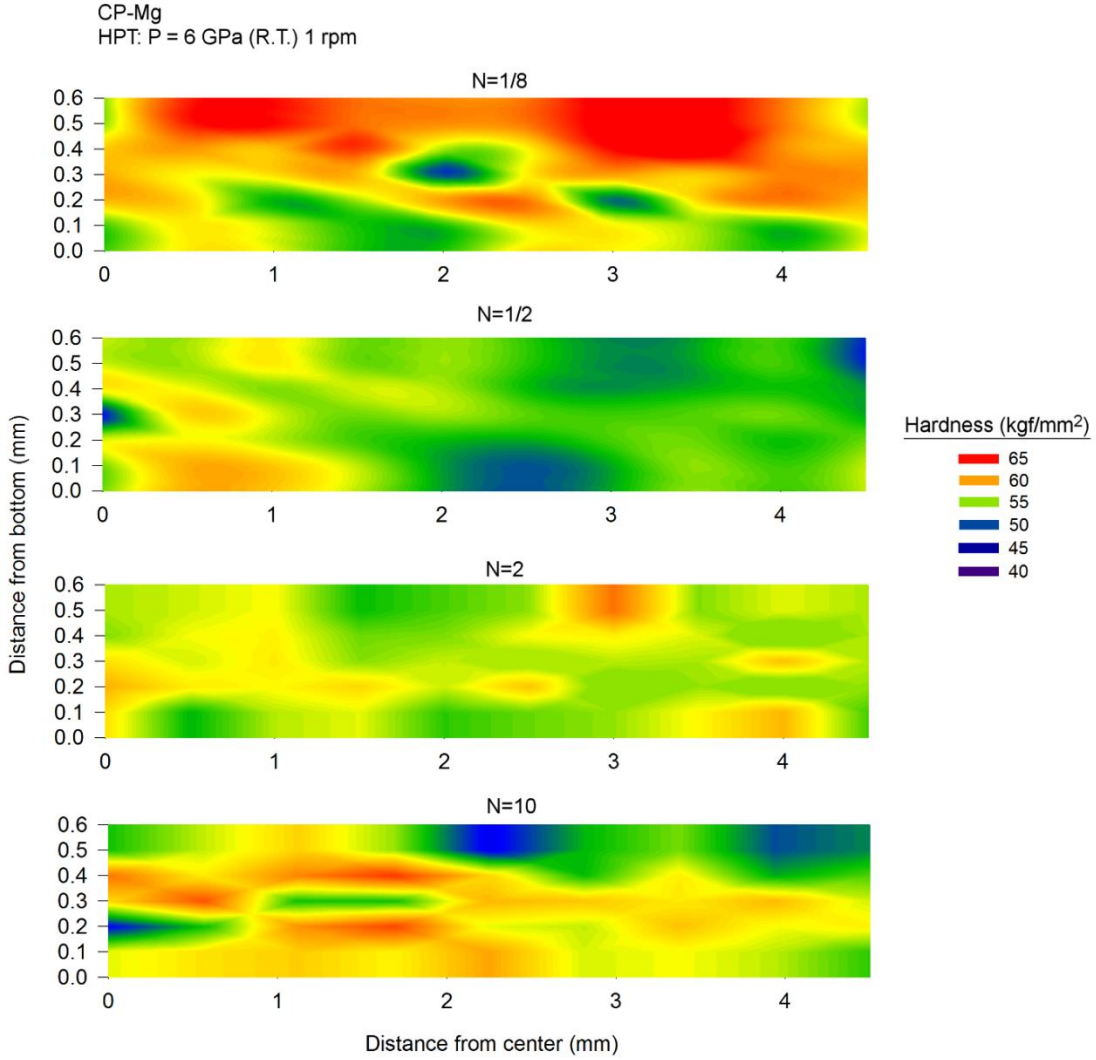

Figure 3.5 – Distribution of hardness at the longitudinal section of discs processed by HPT to 1/8, 1/2, 2 and 10 turns.

Figure 3.6 shows the average hardness plotted as a function of the effective strain. It is observed that the hardness does not vary significantly with the amount of effective strain. Hardness values in the range 55 ~ 60kgf mm^2 are observed at strains in the range 0.3 ~ 200. This disagrees with a report in the literature of a peak hardness at low strains followed by slight softening and saturation [3]. The softening observed at intermediate values of strain in pure magnesium is usually attributed to the occurrence of recovery and recrystallization in this material [3]. However, the present results show that this may not be the case since softening was not observed in the present experiments. Recent reports have showed that pure magnesium exhibit an inverse Hall-Petch relation at very small grain sizes [58] and a change in deformation mechanism [6, 58] takes place at levels of

strain in which the softening effect is usually observed. Grain boundary sliding starts to play a role in deformation leading to an apparent softening effect. Thus, the decrease in hardness is attributed to creep by grain boundary sliding during dwell time in conventional hardness testing. The indentations in the present work were controlled and the dwell time was removed in order to prevent creep and therefore the softening effect was not observed.

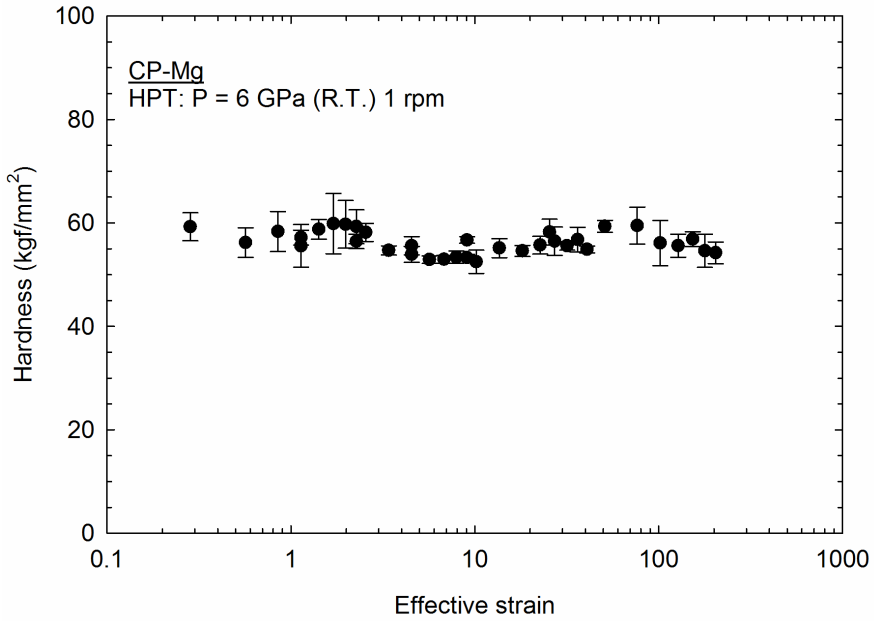

Figure 3.6 – Distribution of hardness as a function of the imposed effective strain in HPT.

3.4 Summary and conclusions

1-High-pressure torsion was used to introduce severe plastic deformation in pure magnesium. EBSD characterization revealed the formation of small grains along grain boundaries of coarse grains. The fine grains gradually consume the coarse grains with increasing imposed strain.

2-The gradual increase in fraction of ultrafine grains and the fast evolution of the distribution of grain boundary misorientation towards high angles differs from other metallic materials and agrees with a model of grain refinement for magnesium processed at high temperatures.

3-The distribution of hardness is heterogeneous along the longitudinal plane of the processed disc which also differs from other metallic materials.
4-The average hardness does not vary with the amount of imposed effective strain during HPT. The softening effect reported in the literature is attributed to the onset of grain boundary sliding and creep during dwell time in conventional hardness testing.

3.5 Acknowledgements

The authors acknowledge support from CNPq, FAPEMIG and CAPES. One of the authors acknowledges support from the European Research Council under ERC Grant Agreement No. 267464-SPDMETALS (TGL).

3.6 References

1. Zhilyaev AP, Langdon TG. Using high-pressure torsion for metal processing: Fundamentals and applications. Progress in Materials Science. 2008;53(6):893-979.

2. Figueiredo RB, Cetlin PR, Langdon TG. Using finite element modeling to examine the flow processes in quasi-constrained high-pressure torsion. Materials Science and Engineering: A. 2011;528(28):8198-204.

3. Edalati K, Yamamoto A, Horita Z, Ishihara T. High-pressure torsion of pure magnesium: Evolution of mechanical properties, microstructures and hydrogen storage capacity with equivalent strain. Scripta Materialia. 2011;64(9):880-3.

4. Figueiredo RB, Aguilar MTP, Cetlin PR, Langdon TG. Processing magnesium alloys by severe plastic deformation. In: Beausir B, Bouaziz O, Bouzy E, Grosdidier T, Toth LS, editors. 6th International Conference on Nanomaterials by Severe Plastic Deformation. IOP Conference Series-Materials Science and Engineering. 632014.

5. Figueiredo RB, Poggiali FSJ, Silva CLP, Cetlin PR, Langdon TG. The influence of grain size and strain rate on the mechanical behavior of pure magnesium. Journal of Materials Science. 2016;51(6):3013-24.

6. Figueiredo RB, Sabbaghianrad S, Giwa A, Greer JR, Langdon TG. Evidence for exceptional low temperature ductility in polycrystalline magnesium processed by severe plastic deformation. Acta Materialia. 2017;122:322-31.

7. Huang Y, Figueiredo RB, Baudin T, Brisset F, Langdon TG. Evolution of Strength and Homogeneity in a Magnesium AZ31 Alloy Processed by High-Pressure Torsion at Different Temperatures. Advanced Engineering Materials. 2012;14(11):1018-26.

8. Huang Y, Figueiredo RB, Baudin T, Helbert AL, Brisset F, Langdon TG. Microstructure and Texture Evolution in a Magnesium Alloy During Processing by High-Pressure Torsion. Materials Research-Ibero-American Journal of Materials. 2013;16(3):577-85.

9. Serre P, Figueiredo RB, Gao N, Langdon TG. Influence of strain rate on the characteristics of a magnesium alloy processed by high-pressure torsion. Materials Science and Engineering: A. 2011;528(10-11):3601-8.

10. Stráská J, Janeček M, Gubicza J, Krajňák T, Yoon EY, Kim HS. Evolution of microstructure and hardness in AZ31 alloy processed by high pressure torsion. Materials Science and Engineering: A. 2015;625:98-106.

11. Xu J, Wang X, Shirooyeh M, Xing G, Shan D, Guo B, et al. Microhardness, microstructure and tensile behavior of an AZ31 magnesium alloy processed by high-pressure torsion. Journal of Materials Science. 2015;50(22):7424-36.

12. Harai Y, Kai M, Kaneko K, Horita Z, Langdon TG. Microstructural and Mechanical Characteristics of AZ61 Magnesium Alloy Processed by High-Pressure Torsion. MATERIALS TRANSACTIONS. 2008;49(1):76-83.

13. Alsubaie SA, Bazarnik P, Lewandowska M, Huang Y, Langdon TG. Evolution of microstructure and hardness in an AZ80 magnesium alloy processed by high-pressure torsion. Journal of Materials Research and Technology. 2016;5(2):152-8.

14. Al-Zubaydi A, Figueiredo RB, Huang Y, Langdon TG. Structural and hardness inhomogeneities in Mg-Al-Zn alloys processed by high-pressure torsion. Journal of Materials Science. 2013;48(13):4661-70.

15. Al-Zubaydi ASJ, Zhilyaev AP, Wang SC, Kucita P, Reed PAS. Evolution of microstructure in AZ91 alloy processed by high-pressure torsion. Journal of Materials Science. 2016;51(7):3380-9.

16. Al-Zubaydi ASJ, Zhilyaev AP, Wang SC, Reed PAS. Superplastic behaviour of AZ91 magnesium alloy processed by high-pressure torsion. Materials Science and Engineering: A. 2015;637:1-11.

17. Galiyev A, Kaibyshev R. Microstructural Evolution in ZK60 Magnesium Alloy during Severe Plastic Deformation. MATERIALS TRANSACTIONS. 2001;42(7):1190-9.

18. Lee H-J, Lee SK, Jung KH, Lee GA, Ahn B, Kawasaki M, et al. Evolution in hardness and texture of a ZK60A magnesium alloy processed by high-pressure torsion. Materials Science and Engineering: A. 2015;630:90-8.

19. Torbati-Sarraf SA, Langdon TG. Properties of a ZK60 magnesium alloy processed by high-pressure torsion. Journal of Alloys and Compounds. 2014;613:357-63.

20. Basha DA, Sahara R, Somekawa H, Rosalie JM, Singh A, Tsuchiya K. Interfacial segregation induced by severe plastic deformation in a Mg–Zn–Y alloy. Scripta Materialia. 2016;124:169-73.

21. Jenei P, Gubicza J, Yoon EY, Kim HS. X-ray diffraction study on the microstructure of a Mg–Zn–Y alloy consolidated by high-pressure torsion. Journal of Alloys and Compounds. 2012;539:32-5.

22. Alizadeh R, Mahmudi R, Ngan AHW, Huang Y, Langdon TG. Superplasticity of a nano-grained Mg–Gd–Y–Zr alloy processed by high-pressure torsion. Materials Science and Engineering: A. 2016;651:786-94.

23. Dobatkin SV, Rokhlin LL, Lukyanova EA, Murashkin MY, Dobatkina TV, Tabachkova NY. Structure and mechanical properties of the Mg-Y-Gd-Zr alloy after high pressure torsion. Materials Science and Engineering: A. 2016;667:217-23.

24. Gao JH, Guan SK, Ren ZW, Sun YF, Zhu SJ, Wang B. Homogeneous corrosion of high pressure torsion treated Mg–Zn–Ca alloy in simulated body fluid. Materials Letters. 2011;65(4):691-3.

25. Kulyasova OB, Islamgaliev RK, Zhao Y, Valiev RZ. Enhancement of the Mechanical Properties of an Mg–Zn–Ca Alloy Using High-Pressure Torsion. Advanced Engineering Materials. 2015;17(12):1738-41.

26. Kulyasova O, Islamgaliev R, Zhao Y, Valiev R. Microstructure and mechanical properties of ultrafinegrained Mg-Zn-Ca alloy. IOP Conference Series: Materials Science and Engineering. 2014;63(1):012142.

27. Zhang CZ, Zhu SJ, Wang LG, Guo RM, Yue GC, Guan SK. Microstructures and degradation mechanism in simulated body fluid of biomedical Mg–Zn–Ca alloy processed by high pressure torsion. Materials & Design. 2016;96:54-62.

28. Kocich R, Kunčická L, Král P, Lowe TC. Texture, deformation twinning and hardening in a newly developed Mg–Dy–Al–Zn–Zr alloy processed with high pressure torsion. Materials & Design. 2016;90:1092-9.

29. Kai M, Horita Z, Langdon TG. Developing grain refinement and superplasticity in a magnesium alloy processed by high-pressure torsion. Materials Science and Engineering: A. 2008;488(1–2):117-24.

30. Matsunoshita H, Edalati K, Furui M, Horita Z. Ultrafine-grained magnesium–lithium alloy processed by high-pressure torsion: Low-temperature superplasticity and potential for hydroforming. Materials Science and Engineering: A. 2015;640:443-8.

31. Gajdics M, Calizzi M, Pasquini L, Schafler E, Révész Á. Characterization of a nanocrystalline Mg–Ni alloy processed by high-pressure torsion during hydrogenation and dehydrogenation. International Journal of Hydrogen Energy. 2016;41(23):9803-9.

32. Grill A, Horky J, Panigrahi A, Krexner G, Zehetbauer M. Long-term hydrogen storage in Mg and ZK60 after Severe Plastic Deformation. International Journal of Hydrogen Energy. 2015;40(47):17144-52.

33. Hongo T, Edalati K, Arita M, Matsuda J, Akiba E, Horita Z. Significance of grain boundaries and stacking faults on hydrogen storage properties of Mg2Ni intermetallics processed by high-pressure torsion. Acta Materialia. 2015;92:46-54.

34. Leiva DR, Jorge AM, Ishikawa TT, Huot J, Fruchart D, Miraglia S, et al. Nanoscale Grain Refinement and H-Sorption Properties of MgH2 Processed by High-Pressure Torsion and Other Mechanical Routes. Advanced Engineering Materials. 2010;12(8):786-92.

35. Soyama J, Floriano R, Leiva DR, Guo Y, Jorge Junior AM, Pereira da Silva E, et al. Severely deformed ZK60 + 2.5% Mm alloy for hydrogen storage produced by two different processing routes. International Journal of Hydrogen Energy. 2016;41(26):11284-92.

36. Silva CLP, Oliveira AC, Costa CGF, Figueiredo RB, de Fátima Leite M, Pereira MM, et al. Effect of severe plastic deformation on the biocompatibility and corrosion rate of pure magnesium. Journal of Materials Science. 2017:in press.

37. Kawasaki M, Figueiredo RB, Langdon TG. An investigation of hardness homogeneity throughout disks processed by high-pressure torsion. Acta Materialia. 2011;59(1):308-16.

38. Kawasaki M, Figueiredo RB, Langdon TG. Twenty-five years of severe plastic deformation: recent developments in evaluating the degree of homogeneity through the thickness of disks processed by high-pressure torsion. Journal of Materials Science. 2012;47(22):7719-25.

39. Hohenwarter A, Bachmaier A, Gludovatz B, Scheriau S, Pippan R. Technical parameters affecting grain refinement by high pressure torsion. Int J Mater Res. 2009;100(12):1653-61.

40. Figueiredo RB, Aguilar MTP, Cetlin PR, Langdon TG. Analysis of plastic flow during high-pressure torsion. Journal of Materials Science. 2012;47(22):7807-14.

41. Figueiredo RB, de Faria GCV, Cetlin PR, Langdon TG. Three-dimensional analysis of plastic flow during high-pressure torsion. Journal of Materials Science. 2013;48(13):4524-32.

42. Sakai G, Nakamura K, Horita Z, Langdon TG. Developing high-pressure torsion for use with bulk samples. Materials Science and Engineering: A. 2005;406(1–2):268-73.

43. Figueiredo RB, Langdon TG. Heterogeneous Flow During High-Pressure Torsion. Materials Research-Ibero-American Journal of Materials. 2013;16(3):571-6.

44. Figueiredo RB, Langdon TG. Development of structural heterogeneities in a magnesium alloy processed by high-pressure torsion. Materials Science and Engineering: A. 2011;528(13-14):4500-6.

45. Xu C, Horita Z, Langdon TG. Microstructural Evolution in Pure Aluminum in the Early Stages of Processing by High-Pressure Torsion. MATERIALS TRANSACTIONS. 2010;51(1):2-7.

46. Ito Y, Horita Z. Microstructural evolution in pure aluminum processed by high-pressure torsion. Materials Science and Engineering: A. 2009;503(1–2):32-6.

47. Ivanisenko Y, Valiev RZ, Fecht HJ. Grain boundary statistics in nano-structured iron produced by high pressure torsion. Materials Science and Engineering: A. 2005;390(1–2):159-65.

48. Figueiredo RB, Langdon TG. Grain refinement and mechanical behavior of a magnesium alloy processed by ECAP. Journal of Materials Science. 2010;45(17):4827-36.

49. Figueiredo RB, Langdon TG. The nature of grain refinement in equal-channel angular pressing: a comparison of representative fcc and hcp metals. Int J Mater Res. 2009;100(12):1638-46.

50. Figueiredo RB, Langdon TG. Principles of grain refinement in magnesium alloys processed by equal-channel angular pressing. Journal of Materials Science. 2009;44(17):4758-62.

51. Figueiredo RB, Pereira PHR, Aguilar MTP, Cetlin PR, Langdon TG. Using finite element modeling to examine the temperature distribution in quasi-constrained high-pressure torsion. Acta Materialia. 2012;60(6-7):3190-8.

52. Pereira PHR, Figueiredo RB, Huang Y, Cetlin PR, Langdon TG. Modeling the temperature rise in high-pressure torsion. Materials Science and Engineering: A. 2014;593:185-8.

53. Jonas JJ, Ghosh C, Toth LS. The equivalent strain in high pressure torsion. Materials Sci ence and Engineering: A. 2014;607:530-5.

54. Valiev RZ, Ivanisenko YV, Rauch EF, Baudelet B. Structure and deformaton behaviour of Armco iron subjected to severe plastic deformation. Acta Materialia. 1996;44(12):4705-12.

55. Bonarski BJ, Schafler E, Mingler B, Skrotzki W, Mikulowski B, Zehetbauer MJ. Texture evolution of Mg during high-pressure torsion. Journal of Materials Science. 2008;43(23):7513.

56. Partridge PG. The crystallography and deformation modes of hexagonal close-packed metals. Metallurgical Reviews. 1967;12(1):169-94.

57. del Valle JA, Pérez-Prado MT, Ruano OA. Distribución de ángulos de desorientación en la aleación de Mg laminada AZ31. 2002. 2002;38(5):5.

58. Somekawa H, Mukai T. Hall-Petch Breakdown in Fine-Grained Pure Magnesium at Low Strain Rates. Metallurgical and Materials Transactions A. 2015;46A(2):894-902.

4. CAPÍTULO 4 – EFFECT OF SEVERE PLASTIC DEFORMATION ON THE BIOCOMPATIBILITY AND CORROSION RATE OF PURE MAGNESIUM

Cláudio L. P. Silva[1], Ana Celeste Oliveira[1], Cíntia G. F. Costa[2],

Roberto B. Figueiredo[3,*], Maria de Fátima Leite[4], Marivalda M. Pereira[1],

Vanessa F. C. Lins[2], Terence G. Langdon[5,6]

[1] Department of Metallurgical and Materials Engineering, Universidade Federal de Minas Gerais, Belo Horizonte 31270-901 MG, Brazil
[2] Department of Chemical Engineering, Universidade Federal de Minas Gerais, Belo Horizonte 31270-901 MG, Brazil
[3] Department of Materials Engineering and Civil Construction, Universidade Federal de Minas Gerais, Belo Horizonte 31270-901 MG, Brazil
[4] Department of Physiology and Biophysics, Universidade Federal de Minas Gerais, Belo Horizonte 31270-901 MG, Brazil
[5] Materials Research Group, Faculty of Engineering and the Environment, University of Southampton, Southampton SO17 1BJ, U.K.
[6] Departments of Aerospace & Mechanical Engineering and Materials Science, University of Southern California, Los Angeles, CA 90089-1453, U.S.A.

*Corresponding author: figueiredo@demc.ufmg.br

Abstract

It is well established that magnesium has a considerable potential for use as a biodegradable material. This report describes the effect of processing by severe plastic deformation (SPD) on the grain refinement, mechanical behavior, biocompatibility and corrosion behavior of commercial purity (CP) magnesium. The material was received as cast slabs and processed by rolling, equal-channel angular pressing and high-pressure torsion to produce samples with average grain sizes in the range of ~0.5 - 300 μm. The results show that severe plastic deformation does not affect the biocompatibility. However, the corrosion behavior is affected by the processing route. Specifically, SPD processing leads to general corrosion as opposed to localized corrosion in the as-cast and hot-rolled condition.

Keywords: biocompatibility; corrosion; equal-channel angular pressing; high-pressure torsion; magnesium

4.1 Introduction

Magnesium and its alloys are attracting significant attention among potential biomaterials due to their good mechanical, biological and electrochemical behavior [1,2]. Experiments show that magnesium alloys can degrade in vivo and exhibit a good biological response [1,3]. However, the high corrosion rate of this metal in a physiological environment may lead to the premature failure of implants. Also the high rate of hydrogen formation, which is a byproduct of the corrosion of magnesium, may produce an accumulation of this gas around the implant and trigger adverse physiological reactions [4]. Alloying is used to reduce the corrosion rate of magnesium but this procedure may lead to undesirable effects in the biocompatibility depending on the type and amount of alloying elements [1]. The high corrosion rate of magnesium can lead also to a fast delivery of alloying elements and even common elements such as Zn, Ca and Mn can become toxic [5].

Another strategy to control the corrosion rate of magnesium and its alloys is through the use of thermo-mechanical processing since changes in the microstructure affect the corrosion behavior. For example, it has been reported that texture may affect the corrosion rate. Thus, samples cut parallel to the extrusion direction exhibit lower corrosion rates than samples cut perpendicular [6] and it was reported also that the corrosion rate decreases with an increase in the intensity of basal planes parallel to the surface [7]. Decreasing the grain size [8,9] and homogenizing the second phase particle distribution [10] also reduces the corrosion rate. Among the thermo-mechanical processing techniques, severe plastic deformation (SPD) processes [11] are gaining significant attention because of their potential for producing fully-dense bulk samples with exceptionally small grain sizes. Also, processing by SPD can improve the homogeneity of the distribution of impurities and second phase particles.

The most attractive SPD techniques are equal-channel angular pressing (ECAP) [12] and high-pressure torsion (HPT) [13]. The former can produce samples with larger dimensions but the low ductility of magnesium prevents ECAP processing at low

temperatures. As a consequence, processing of magnesium is usually carried out at high temperatures and the final grain sizes are in the range of a few micrometers [14-17]. By contrast, high hydrostatic pressures are generated during HPT and this permits the processing of materials with low ductility including magnesium [18]. As a consequence, the final grain sizes after HPT are generally smaller than after other thermo-mechanical processing techniques [19,20] and there is also a higher fraction of grain boundaries having high angles of misorientation [21].

Many reports have shown that SPD significantly modifies the properties of magnesium and its alloys. For example, ECAP introduces exceptional superplastic properties at high temperatures [22] and increases the hardness at low temperatures [23]. These improved mechanical properties are attractive for biomedical applications. Thus, a recent report demonstrated the fabrication of a biodegradable stent from a magnesium alloy processed by ECAP followed by extrusion and laser cutting [24]. In addition, HPT processing also shows the development of superplasticity and improved hardness in magnesium alloys and a recent report described the development of exceptional ductility in pure magnesium at room temperature after processing by HPT [25].

Although it is known that SPD improves the mechanical behavior of magnesium and its alloys, its effect on the corrosion behavior is not yet clearly defined because reports have demonstrated different trends. For example, a weaker corrosion resistance, more and deeper corrosion pits and a higher rate of mass loss in a 3.5 wt.% NaCl solution was reported in pure magnesium after processing by ECAP compared to the as-cast material [26]. On the other hand, a reduced degradation rate in Hank´s solution was reported in a magnesium AZ31alloy processed by ECAP by comparison with the squeeze-cast counterpart [27]. An improved corrosion resistance in an AZ31 alloy after processing by ECAP was also reported in NaCl and phosphate-buffer solution-PBS and this was attributed to the early formation of a protective layer of corrosion products [28]. It was also reported that HPT processing improved the corrosion resistance of a Mg-2 wt.% Zn-0.24 wt.% Ca alloy [10]. A recent report [29] showed that grain refinement can lead to a higher corrosion rate in materials in which the corrosion current is high, >10-5 A.cm2, but the presence of grain boundaries may help in developing a passive layer in materials with a low corrosion current, <10-5 A.cm2, and

this suggests that grain refinement may improve the corrosion resistance. Accordingly, the present investigation was initiated to determine the effect of different thermo-mechanical processing operations, including SPD techniques, on the mechanical behavior, biocompatibility and corrosion behavior of pure magnesium.

4.2 Experimental material and procedures

Commercial purity (CP) magnesium (99.7% purity) was provided by RIMA (Bocaiúva-MG) in the form of as-cast slabs. Plate samples of 5 mm thickness were cut, heated to 673 K and subjected to 7 passes of rolling. These sheets were re-heated to 673 K between each pass and the reduction per pass was ~20% leading to a final sheet thickness of ~1.0 mm. Some hot-rolled samples were annealed for 1 h at 523 K and others were cut into 60 × 10 × 1 mm3 sheets which were stacked and wrapped in copper foil for processing by ECAP. The ECAP die had a channel angle of 135º, a 10 × 10 mm2 square cross-section and electric resistances for heating. This channel angle imposes a strain on the billet of ~0.5 in each pass through the die [30]. The samples were processed by 4 passes at 473 K using route C in which the billets are rotated by 180º between passes [31]. Discs of 10 mm diameter and 0.8 mm thickness were cut from the as-cast material and processed by HPT under a pressure of 6.0 GPa up to 10 turns.

The microstructures of the as-cast material and the material processed by hot-rolling and hot-rolling followed by annealing were investigated by optical microscopy after conventional metallographic sample preparation. The samples were cut, embedded in resin, ground and polished to mirror-like finishes and then etched in a 0.05% nitric acid solution in ethanol to reveal the grain boundaries. Samples of the material processed by hot-rolling followed by ECAP were prepared following a similar procedure but the microstructure was investigated by scanning electron microscopy (SEM) in order to obtain a higher magnification and permit observations of the smaller grains. The ultrafine-grained (UFG) microstructure of the material processed by HPT was examined by transmission electron microscopy (TEM) in which discs of 3 mm diameter were cut from the HPT-processed samples, ground to thicknesses of ~0.1 mm and then polished to perforation using a double jet electro-chemical polisher.

Tensile tests were carried out at room temperature using dog-bone specimens with an initial strain rate of 10-3 s-1. An electronic extensometer was used to record strain data for all samples except for the material processed by HPT due to the reduced size of the tensile specimens.

In this work, a human osteosarcoma cell line (SAOS-2), obtained from Rio de Janeiro Cell Bank (BCRJ, Brazil), was used to assess the cytotoxicity of Mg-based materials. Firstly, the mitochondrial metabolic activity was quantitatively determined using 3-(4,5-dimethylthiazolyl-2)-2,5-diphenyltetrazolium bromide (MTT) (Sigma-Aldrich, St. Louis, MO, USA). This test consisted of the reduction of MTT to an insoluble purple formazan by cleavage of the tetrazolium ring by dehydrogenase enzymes, expressing cell functionality. Secondly, vital status and cell morphology were qualitatively evaluated using a LIVE/DEAD® Viability/Cytotoxicity Kit (Molecular Probes, Eugene, OR, USA). This assay is based on plasma membrane integrity and esterase activity, indicating cell viability. Dulbecco's modified Eagle's medium (DMEM) was used as negative control with 1% Triton-X 100 (Sigma-Aldrich, St. Louis, MO, USA) as positive control. CP magnesium samples with 48 mm2 area, processed by five different methods (as-cast, hot-rolled, hot-rolled + annealing, hot-rolled + ECAP and HPT), were rinsed in 70% ethanol for 5 min, washed three times in distilled water, dried and sterilized by ultraviolet radiation.

To perform the MTT assay, 3 x 104 cells/mL were seeded per well in a 24-well plate with DMEM containing 10% fetal bovine serum (FBS), 1% antibiotic-antimycotic and maintained for 24 h in a controlled 5% CO2 95% humidified incubator at 37ºC. After 24 h of cell culture, cells were directly exposed to materials for 24 h. After the exposure period, materials were removed and 210 μL of fresh medium was added in each well. Then, 170μL of MTT solution (5 mg mL-1) was added and the cells were incubated for 4 h. Afterwards, 170 μL of SDS solution/4% HCl was placed and incubated for 12 h. Absorbance was quantified at 595 nm in a spectrophotometer. For each experimental condition, three different measures were taken. All values were normalized to the controls and expressed as a percentage of the cell function. Negative control (functional cells) was considered as 100%. The statistical analysis performed was one way/ANOVA/Bonferroni (GraphPad Prism software, San Diego, CA, USA) and significant differences were considered for $p<0.05$.

Significantly, 6 x 104 SAOS cells were seeded on glass coverslips in 6-well plates with 2 mL of DMEM containing 10% FBS and 1% antibiotic-antimycotic, maintained for 24 h in a controlled 5% CO2 95% humidified incubator at 37ºC, and then exposed to materials for 24 h. After exposure, the materials were removed, the cells were rinsed twice with phosphate-buffered saline (PBS) and their vital status was observed using the LIVE/DEAD® kit according to the manufacturer´s protocol. Cells were examined under a fluorescent confocal microscope (Zeiss LSM 510, Thornwood, NY) with an excitation at 488 nm and observations at 505 nm to detect calcein, and excitation at 555 nm and observations at 605 nm to detect ethidium homodimer 1.

Electrochemical corrosion tests were carried out using a Princeton Applied Research potentiostat model Versat 3 with 3 electrodes: Ag/AgCl as a reference, platinum as counter-electrode and the magnesium samples as the work electrode. The corrosion solution was NaCl 3.5 wt.%. The scan rate for the polarization tests was 5 mV/s, the frequency range was 10 mHz to 10 kHz and the amplitude was 10 mV in relation to the open circuit potential in the electrochemical impedance spectroscopy tests. The NaCl solution was used to provide the opportunity to compare the results with the literature since this is the most common corrosion environment for testing pure magnesium.

The rate of mass loss was determined in 3.5 wt.% NaCl solution using the rate of H2 formation following a procedure described elsewhere [32].The samples for these tests were ground to #4000 SiC paper and immersed in the solution. A funnel was used to collect H2 and the volume of gas was tracked up to 6 h for all conditions of processing. The as-cast material and the materials processed by ECAP and HPT were subjected to longer testing of up to 48 h.

4.3 Experimental results

Representative images of the microstructures of the magnesium after different processing routes are shown in Fig. 4.1. It is apparent that the material has a coarse grain structure in the as-cast condition. Hot-rolling promotes significant grain refinement but the grain structure becomes heterogeneous so that there are bands of finer grains (<10 μm) intermixed with larger grains in the range of tens of microns, thereby suggesting the occurrence of concentrations of deformation. Annealing at 523 K

for 1 h after hot-rolling promotes homogenization of the grain size distribution without any significant grain growth whereas processing by ECAP after hot-rolling leads to excellent grain refinement throughout the sample volume. An ultrafine grain structure was also observed after HPT processing. Measurements showed that the average grain sizes were ~480 μm in the as-cast condition, ~16 μm after hot-rolling, ~24 μm after hot-rolling and annealing, ~3.2 μm after hot-rolling and ECAP and ~0.56 μm after HPT.

The engineering stress vs. strain curves obtained from tensile testing are shown in Fig. 4.2 for all five experimental conditions. The as-cast material exhibited low strength and low ductility with a yield stress of ~34 MPa and an elongation of ~5%. Hot rolling increased the yield stress to ~110 MPa but with no overall improvement in the ductility. The material subjected to annealing after hot-rolling also exhibited a yield stress of ~110 MPa but the final elongation increased slightly to ~7% and the material processed by ECAP after hot rolling exhibited the highest yield stress of ~140 MPa and displayed a reasonable elongation of ~8%. By contrast, the stress-strain curve after HPT exhibited a different behavior with a relatively low strength, a yield stress of ~80 MPa, but with an exceptional ductility to an elongation of ~130%.

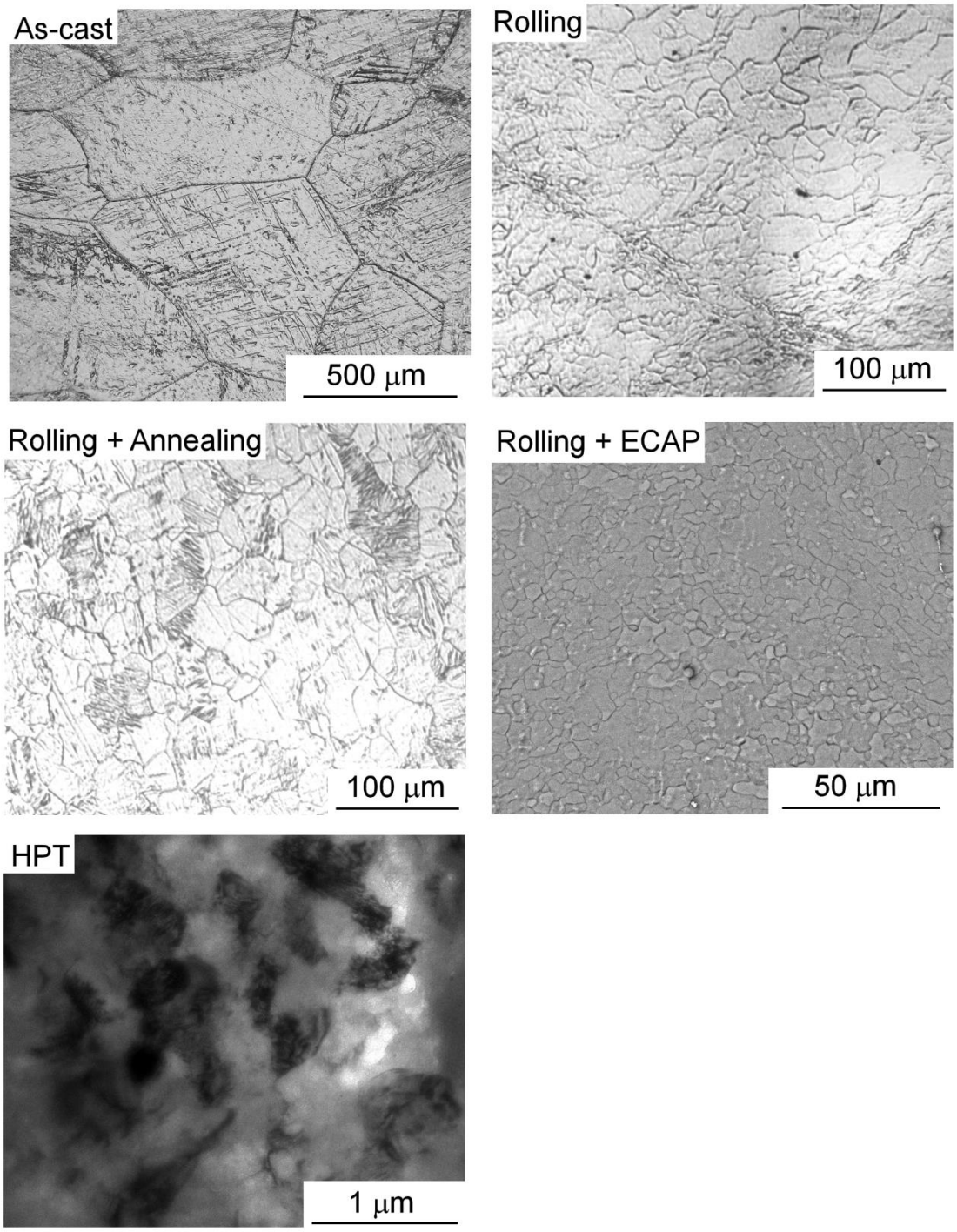

Figure 4.1 – Microestruture of magnesium with different processing history.

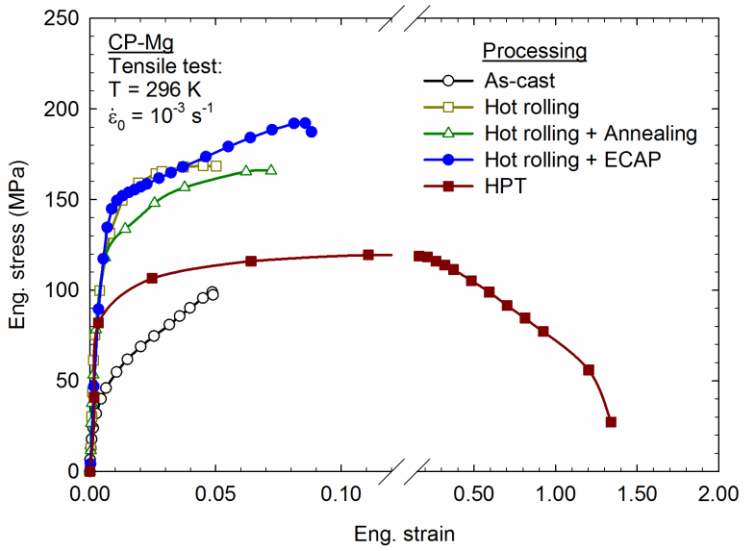

Figure 4.2 – Stress vs strain curves determined for the material with different processing history.

The cytotoxicity evaluation using MTT and LIVE/DEAD assays demonstrated that magnesium with different processing histories (as-cast, rolling, rolling and annealing, rolling and ECAP, HPT) generated a non-cytotoxic environment. As shown in Fig. 3, the cytotoxic analyses determined quantitatively by the MTT test demonstrated that SAOS cells exposed to magnesium samples for 24 h presented no significant alterations in their mitochondrial metabolic activity when compared to the control group ($p<0.05$), thereby indicating high levels of cell viability. The experimental groups produced levels of cell function above 50%.

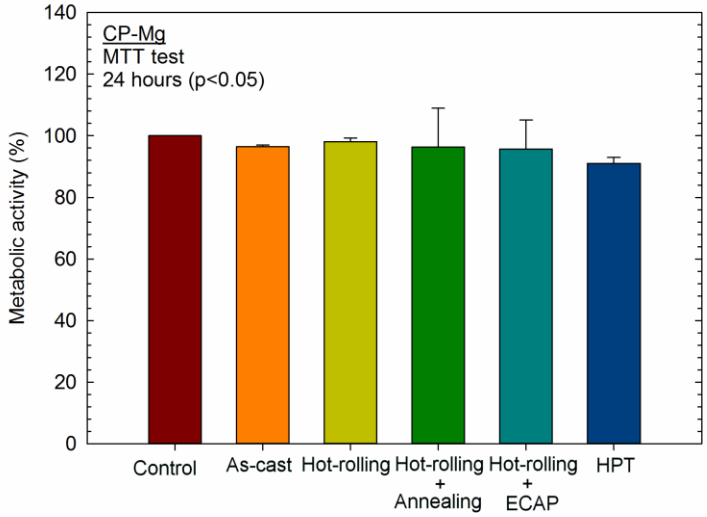

Figure 4.3 – Cell metabolic activity of SAOS exposed for 24 h to magnesium with different processing history (as-cast, rolling, rolling and annealing, rolling and ECAP, and HPT).

The cytotoxicity analysis using the LIVE/DEAD assay revealed qualitatively that the cells exposed to Mg-based materials for 24 h maintained suitable cell viability. Figure 4.4 shows live cells stained with green fluorescence and dead cells stained with red fluorescence. Live cells were clearly observed in all groups, indicating that the LIVE/DEAD results are consistent with the MTT findings. Additionally, the live cells exhibited cell morphologies similar to the control cells with typical cell spreading.

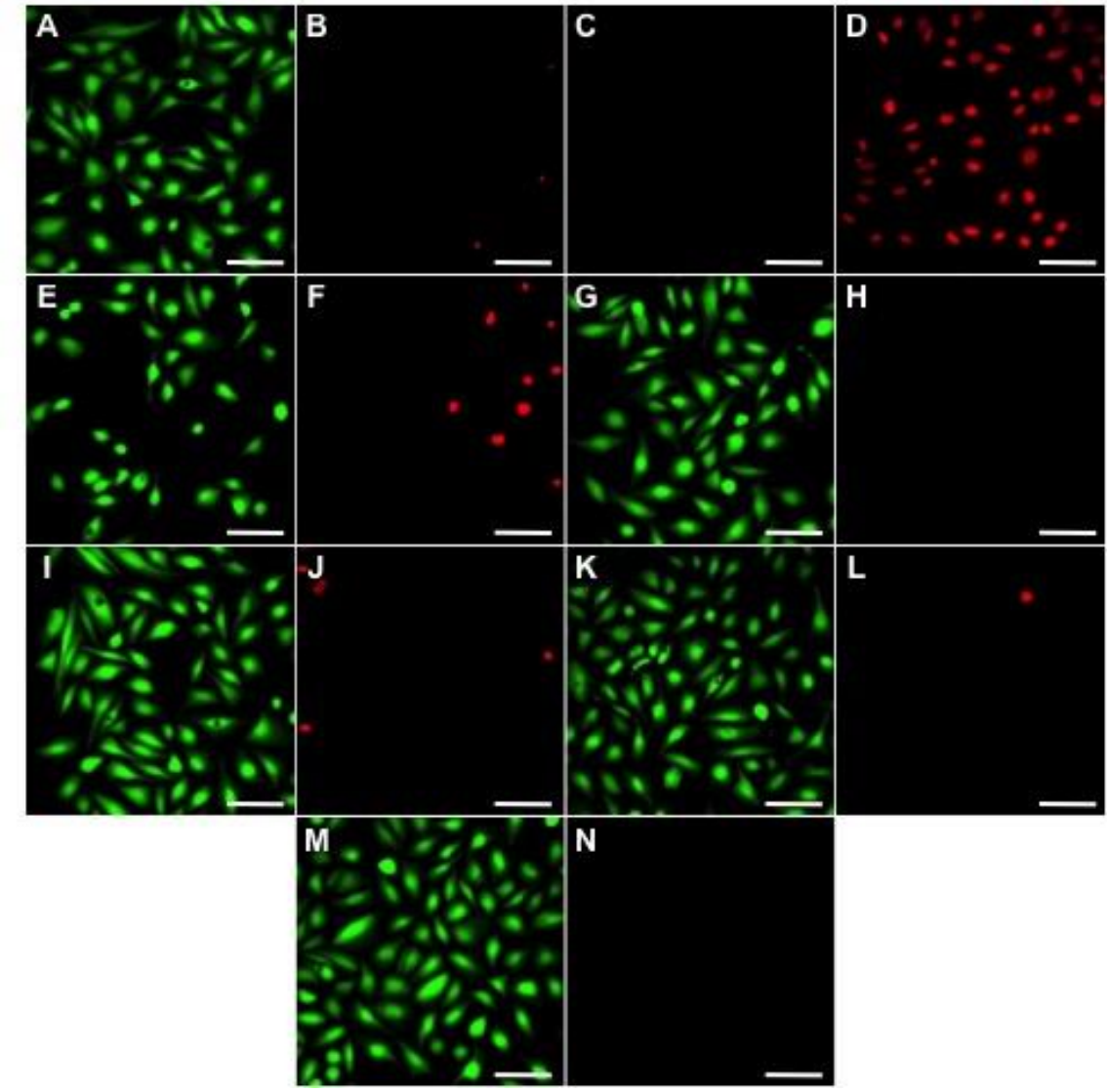

Figure 4.4 – Vital status of SAOS cells exposed to Mg-based materials determined by LIVE/DEAD assay, indicating green fluorescence (viable cells) and red fluorescence (dead cells) images. Negative control (A and B), positive control (C and D), magnesium with different processing history: HPT (E and F), as-cast (G and H), rolling (I and J), rolling and annealing (K and L), rolling and ECAP (M and N).

Figure 4.5 shows the potentiodynamic polarization curves for the samples with different processing histories. It is observed that the as-cast material exhibits a higher open circuit potential and lower corrosion current density which suggests a higher resistance against corrosion. The materials processed by hot-rolling and hot-rolling followed by annealing exhibit a lower open circuit potential and the highest corrosion current density which suggests a lower resistance against corrosion in an aqueous solution of NaCl 3.5 wt.%. It is also apparent that the material processed by SPD exhibits better corrosion resistance than after hot-rolling. The polarization curves of the material processed by hot-rolling and ECAP exhibit an open circuit potential which is almost as high as the as-cast material and the corrosion current density is higher than the current of the as-cast material but significantly lower than the hot-rolled condition. The polarization curve of the material processed by HPT is similar to the curve of the as-cast material, thereby suggesting this provides the best corrosion resistance.

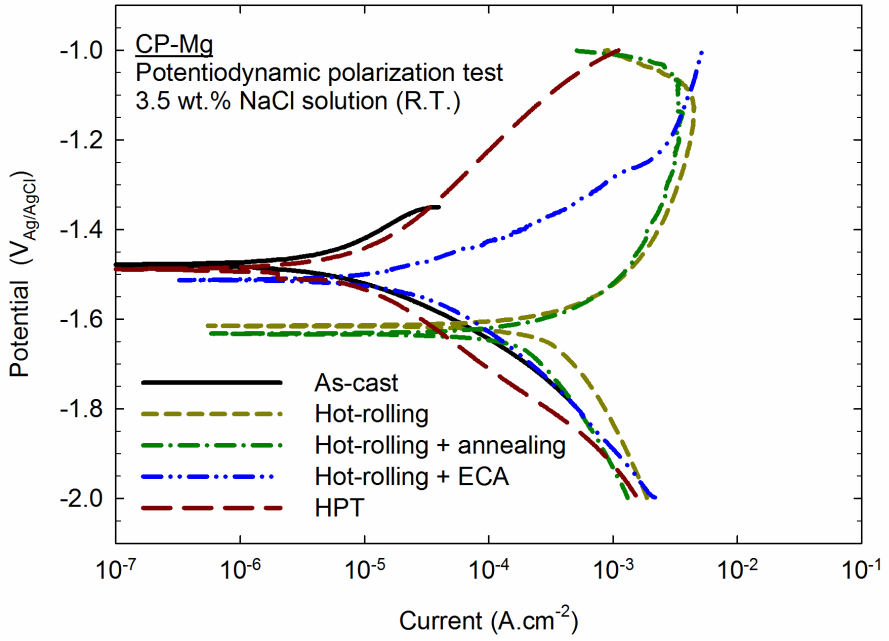

Figure 4.5 – Polarization curves determined in NaCl solution for magnesium with different processing history.

The Nyquist diagrams for the different samples are shown in Fig. 4.6 where Zim and Zre represent the imaginary and the real impedances, respectively. All samples exhibited a capacitive arc suggesting metal dissolution but the diameter of the arc, which directly denotes the resistance to corrosion, differs significantly depending upon

the processing history. The diameter of the arc of the samples processed by hot-rolling with and without annealing are smaller than for the as-cast material suggesting they have a poorer corrosion resistance. The lowest corrosion resistance was observed for the hot-rolled condition where the microstructure was more heterogeneous and with a greater deformation concentration than in the hot-rolled and annealed condition. It is reasonable to assume that the heterogeneous microstructure of the hot-rolled condition generates potential gradients which serve to accelerate the metal corrosion and this is in agreement with the polarization curves. However, the samples processed by SPD exhibit higher polarization resistance compared to the as-cast material indicating a higher corrosion resistance. The largest diameter is observed in the material processed by HPT and all curves, except for the HPT material, exhibit an inductive arc in addition to a capacitive arc. It is known that this inductive behavior is associated with the adsorbed species or with pit formation during corrosion [33,34].

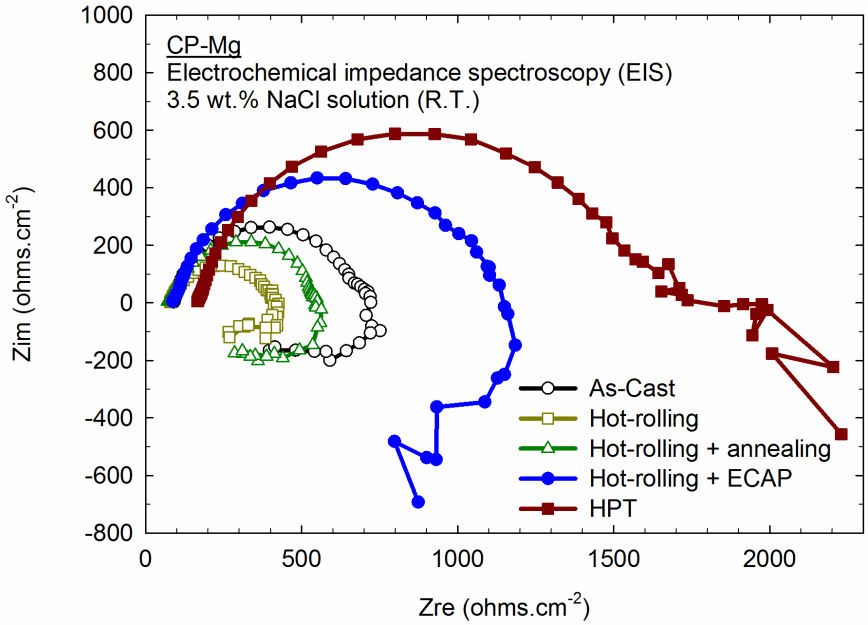

Figure 4.6 – Nyquist curves determined in NaCl solution for magnesium with different processing history.

The mass loss rate is documented in Fig. 4.7 for all samples up to immersion times of 6 h and for the as-cast material and the material processed by SPD up to 48 h. Thus, a lower mass loss rate is observed in the material processed by hot-rolling and annealing. The as-cast material exhibits the second lowest rate while the hot-rolled material and the

material processed by hot-rolling and ECAP exhibit larger rates. The largest rate of mass loss is observed in the material processed by HPT in the first 6 h. This is in disagreement with the results reported by the potentiodynamic polarization curves and the Nyquist diagrams where the HPT processed material exhibits higher corrosion resistance. Nevertheless, long exposure for more than 6 h led to a significant decrease in the mass loss rate of the material processed by HPT and ultimately this became the condition having the lowest mass loss rate.

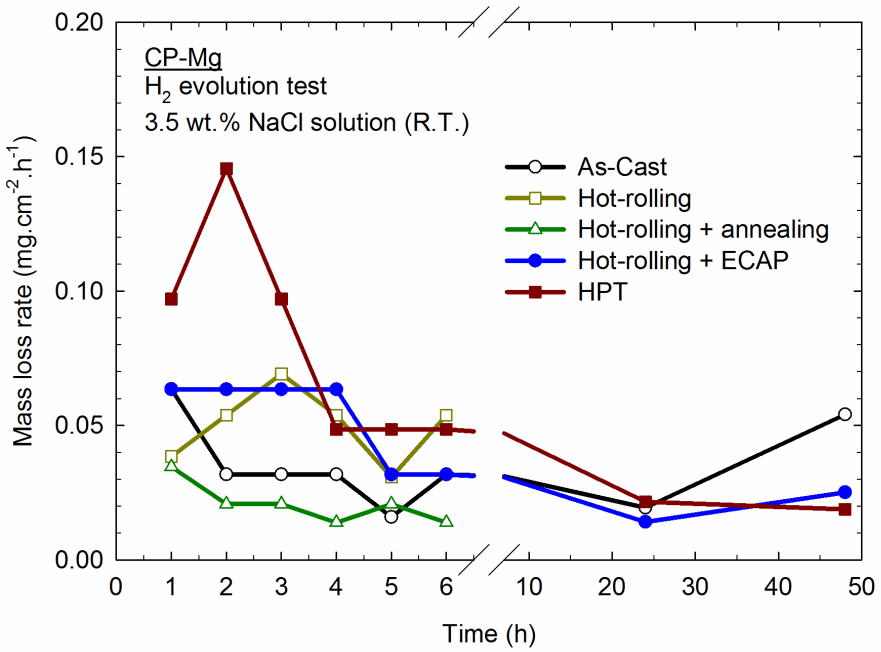

Figure 4.7 – Mass loss rate determined by the evolution of H_2 in NaCl solution for magnesium with different processing history.

Table 4.1 shows a summary of the grain size, d, the electrochemical potential and current, and the estimated mass loss rate based on the electrochemical experiments using an average hydrogen evolution rate for the first 6 h of immersion. The yield stress, σy, and elongation to failure, ΔL/Lo%, are also shown in Table 1. It is noted that there is a significant difference between the values of the estimated mass loss rates using the electrochemical tests and the hydrogen evolution tests. This difference was also reported in earlier experiments and it was shown that the best agreement with the mass loss rate measured by the variation of mass of the sample was obtained by hydrogen evolution [32,35]. It is worth noting that the HPT-processed material exhibited a corrosion current $<10^{-5}$ A.cm^2 and therefore the refinement in grain size is expected to

lower the corrosion rate [29]. This is in very good agreement with the decrease in corrosion rate observed after 48 h of immersion as shown in Fig. 4.7.

Table 4.1 – Summary of grain size, *d*, yield stress (σ_y), corrosion potential (E_{Corr}), corrosion current (I_{Corr}), predicted corrosion rate based on electrochemical testing (ΔW_i) and corrosion rate calculated from the evolution of H_2 (ΔW_H) during the initial 6 h of testing and after 48 h of exposure in 3.5 wt.% NaCl solution.

Processing	d (μm)	σ_y (MPa)	$\Delta L/L_0$ (%)	E_{Corr} (V)	I_{Corr} (mA.cm^{-2})	ΔW_i (mg.cm^{-2}.h^{-1})	ΔW_H (6 h) (mg.cm^{-2}.h^{-1})	ΔW_H (48 h) (mg.cm^{-2}.h^{-1})
As-cast	480	34	5	-1.48	0.007	0.003	0.027	0.054
Hot-rolling	16	110	5	-1.61	0.350	0.159	0.050	-
Hot-rolling + annealing	24	110	7	-1.63	0.210	0.095	0.021	-
Hot-rolling + ECAP	3.2	140	8	-1.51	0.040	0.018	0.065	0.025
HPT	0.56	80	130	-1.49	0.008	0.004	0.055	0.019

It is important to note that there was a change in the overall macroscopic corrosion behavior with the processing conditions. It was noted that localized corrosion occurred in the as-cast material and in the material processed by hot-rolling while there was a more generalized corrosion in the material processed by SPD. The appearances of the corroded surfaces of samples of the as-cast material and the material processed by HPT are shown in Fig. 4.8 for several different exposure periods up to a maximum of 48 h. It is observed that only a fraction of the surface of the as-cast material shows evidence of corrosion after 6 h of immersion whereas the whole surface of the HPT-processed material shows this evidence. This is in agreement with the higher corrosion rate observed in the HPT-processed material in the earliest stages of immersion. A longer immersion period led to the formation of a thick layer of corrosion product in the area of localized corrosion in the as-cast material. By contrast the material processed by HPT exhibited only a thin layer of corrosion products throughout the sample surface even after 48 h of immersion.

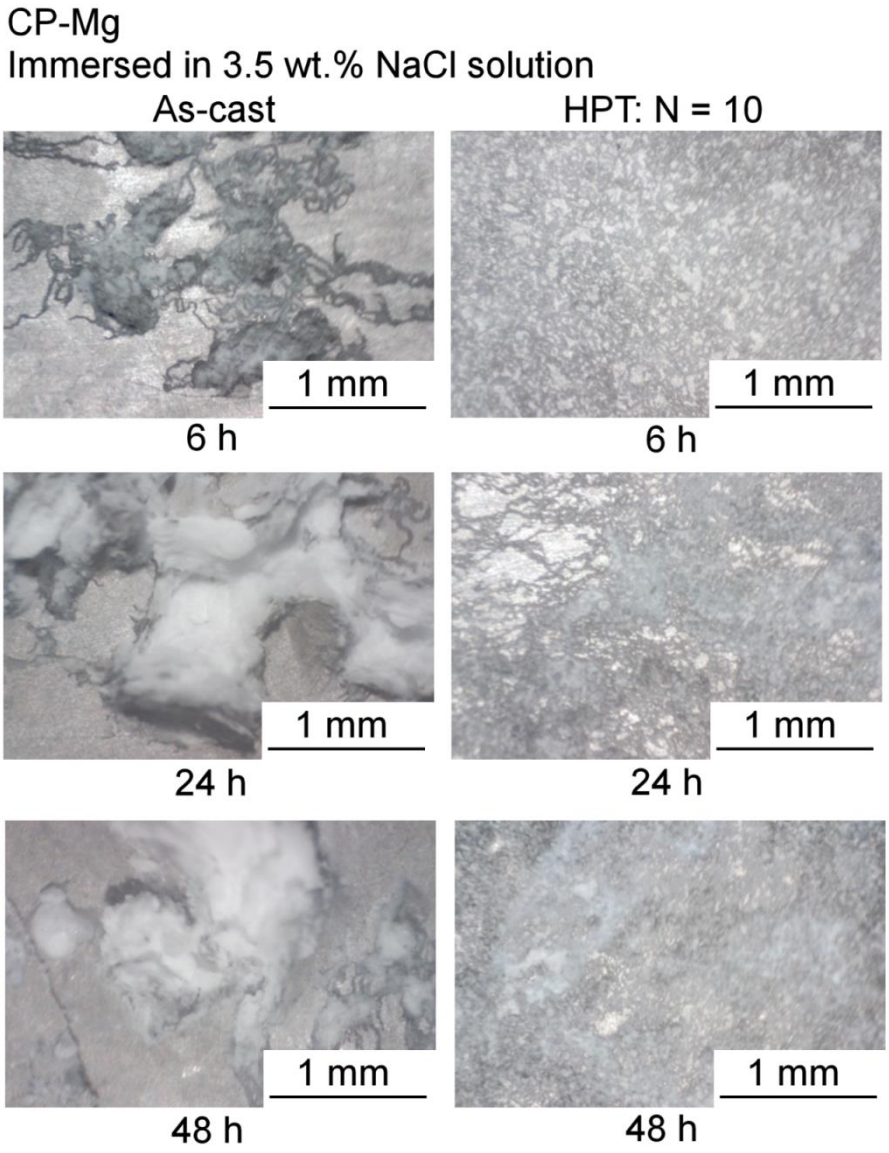

Figure 4.8 – Appearance of surface of samples from the as-cast material and the material processed by HPT after immersion in NaCl solution for different amount of time.

4.4 Discussion

The results obtained in this investigation show that the mechanical properties and the corrosion behavior of pure magnesium are significantly affected by the thermo-mechanical processing. A control of these properties, allied to the good biocompatibility, provides an opportunity to use pure magnesium as biodegradable implants with superior performance. It is apparent that the best combinations of properties are attained through processing by SPD.

4.4.1 Mechanical properties

Pure magnesium usually exhibits poor mechanical properties. Specifically, this material exhibits a low yield stress and low ductility in the coarse-grained condition. Conventional thermo-mechanical processing by hot-rolling improves the strength but does not improve the ductility. However, a moderate ductility is required in many applications. For example, coronary stents are plastically deformed *in situ* and may withstand more plastic deformation during their lifetime. Therefore the material used in their fabrication must display a reasonable ductility [36]. Also, strength is required for bio-implants with structural functions and this becomes even more important for biodegradable implants since the load-bearing area of the product decreases with time. The present results show that ECAP processing leads to the highest yield stress and also displays a good elongation. The improved strength is attributed to the grain refinement while the good elongation is attributed to texture effects. Earlier reports showed that the processing of magnesium alloys by ECAP can lead to a preferential orientation of grains with the basal planes favorably aligned for tensile deformation [37,38]. Thus, the present results demonstrate improvements in both strength and ductility in the material processed by ECAP compared to the as-cast and the hot-rolled conditions.

The mechanical properties of the HPT-processed material exhibits an unexpected low strength compared to the coarser-grained counterparts and an exceptionally high elongation for magnesium at room temperature. The decrease in yield strength of magnesium at very fine grain sizes was reported earlier [39,40] and it was attributed to the onset of grain boundary sliding as a deformation mechanism. Recent reports have shown that fine-grained magnesium can exhibit improved ductility [15] and this is due to a combination of grain boundary sliding and basal slip propagation through grain boundaries having low misorientations [25]. Therefore, HPT processing may be used to produce ductile magnesium with moderate strength. It is worth noting also that the strength of the HPT-processed material is strongly dependent on the strain rate and it may be increased by an appropriate annealing treatment [25].

4.4.2 Cytocompatibility

A previous report documented good cytocompatibility of the elluates of magnesium alloys WE43, WZ21 and ZW21 dissolved in various physiological media. Also, *in vivo* experiments showed that implants from these alloys degrade and lead to the formation of gas bubbles but this does not compromise the physiological functionality of the tissue [1]. Similarly, a degradation of implants made of magnesium alloys AZ31, AZ91, WE43 and LAE442 and gas bubble formation was reported previously [3]. The metallic implants were compared to a biodegradable polymer and the results suggested an osteoblastic response with increased bone mass surrounding the magnesium implants [3]. These reports demonstrate that alloying magnesium with Al and rare earth elements does not compromise the biocompatibility of the material. Also, earlier work demonstrated that changes in the texture of extruded rods of pure magnesium induced no cytotoxicity on a mouse osteoblast cell line by using indirect methods [6]. Additionally, cytotoxicity tests of magnesium-based alloys (Mg-2Ag and Mg-10Gd) and pure magnesium, used as extruded materials, showed that human osteoblasts were mostly alive by LIVE/DEAD staining after 4 or 14 days of exposure and pure magnesium showed moderate cell damage compared with two other alloys studied using these tests [41].

For medical applications, it is extremely important to determine whether the cell behavior is affected by the biomaterials. In this work, a direct contact method was used and both cytotoxic tests MTT and LIVE/DEAD showed clearly that pure magnesium caused no cytotoxic effects on cells. Furthermore, the present results confirm this same result for all processing conditions including when using SPD.

4.4.3 Corrosion behavior

It is apparent that, in addition to the improved mechanical properties, SPD processing improves the corrosion behavior. The electrochemical tests show that the materials processed by ECAP or HPT exhibit higher corrosion potentials compared to their hot-rolled counterpart and a higher impedance compared to the as-cast and the hot-rolled material in an aqueous solution of NaCl 3.5 wt.% . These results suggest a higher resistance against pitting in the SPD materials.

In practice, however, the most important observation is the change in the macroscopic corrosion behavior. Magnesium exhibits localized corrosion in the as-cast condition but HPT processing produces a homogeneous corrosion surface. This is in agreement with the Nyquist diagrams in which the HPT-processed material exhibited the highest polarization resistance without an inductive arc. This result is attributed to the pronounced grain refinement that appears to stimulate the formation of a denser protective layer of corrosion product. It is worth noting also that a decrease in the corrosion rate and an increase in the polarization resistance was observed in an Mg-Y-RE alloy and this was attributed to the grain refinement produced by friction stir processing [8].

An early report described a poorer corrosion resistance in pure magnesium processed by ECAP compared to a squeeze-cast condition [26]. The apparent disagreement with the present results is probably due to the processing conditions and final microstructure. Thus, ECAP processing at 573 K from the cast condition was not effective in refining the grain structure so that grain sizes in the range of ~100-200 μm were produced by ECAP [26]. By contrast, in the present experiments the magnesium was first processed by hot-rolling to achieve a partially-refined microstructure and then processed by ECAP to further refine the grain size. It is known that billet failure during ECAP and the final microstructure depends on the initial grain structure [42]. In practice the initial processing by hot-rolling allows a decrease in the ECAP processing temperature of magnesium without billet failure and this prevents grain growth and thus leads to a finer microstructure. Furthermore, the grain size of ~3.2 μm for the ECAP-processed material in the present experiments was almost two orders of magnitude lower than in the material processed from the cast condition [26] and this changed the corrosion behavior.

A decrease in the corrosion current rate in the NaCl solution with decreasing grain size was reported earlier [14] for magnesium processed by ECAP. In that work, the ECAP processing was carried out with a back-pressure to prevent billet failure and the final grain size was ~2.6 μm. The resistance against corrosion with decreasing grain size was attributed to the increase in grain boundaries with high angles of misorientation that promote a more coherent oxide layer [14]. This hypothesis is in agreement with the

reduction in corrosion rate observed in the present experiments in the samples with very fine grain sizes.

4.5 Summary and conclusions

1. Samples of CP magnesium in the as-cast condition and processed by hot-rolling, hot-rolling and annealing, hot-rolling and ECAP and HPT were used to evaluate the effect of processing on the mechanical behavior, the citotoxicity and the corrosion behavior in NaCl solution.
2. Processing by SPD improves the mechanical properties of magnesium. A higher yield strength and ductility were attained by ECAP compared to the as-cast material and the material processed by hot-rolling. Exceptional ductility and moderate strength were achieved by HPT processing. The biocompatibility was not affected either by the processing history or by the grain size of the magnesium.
3. The corrosion rate was strongly affected by the processing history. A lower corrosion potential and reduced polarization resistance were observed after hot-rolling and after hot-rolling and annealing compared to the as-cast material. Material processed by ECAP or HPT exhibited similar corrosion potentials to the as-cast material and the largest polarization resistance. All materials exhibited an inductive arc except after HPT processing which was associated with the development of more uniform corrosion.
4. The material processed by HPT exhibits the formation of an homogeneous layer of corrosion product that protects the material and decreases the mass loss rate after long immersion times.

4.6 Acknowledgements

The authors acknowledge Prof. A.M. Goes of the Department of Immunology and Biochemistry (UFMG) for providing the human osteosarcoma cell line used in this work. The authors acknowledge support from CNPq, FAPEMIG and PPGEM. One of the authors acknowledges support from the European Research Council under ERC Grant Agreement No. 267464-SPDMETALS (TGL).

4.7 References

1. Hanzi AC, Gerber I, Schinhammer M, Loffler JF, Uggowitzer PJ (2010) On the in vitro and in vivo degradation performance and biological response of new biodegradable Mg-Y-Zn alloys. Acta Biomaterialia 6:1824-1833

2. Witte F, Hort N, Vogt C, Cohen S, Kainer KU, Willumeit R, Feyerabend F (2008) Degradable biomaterials based on magnesium corrosion. Current Opinion in Solid State and Materials Science 12:63-72

3. Witte F, Kaese V, Haferkamp H, Switzer E, Meyer-Lindenberg A, Wirth CJ, Windhagen H (2005) In vivo corrosion of four magnesium alloys and the associated bone response. Biomaterials 26:3557-3563

4. Zberg B, Ugowitzer PJ, Loffler JF (2009) MgZnCa glasses without clinically observable hydrogen evolution for biodegradable implants. Nature Materials 8 (11):887-891

5. Kirklan NT (2012) Magnesium biomaterials: past, present and future. . Corrosion Engineering, Science and Technology 47:322-328

6. Bahl S, Suwas S, Chatterjee K (2014) The control of crystallographic texture in the use of magnesium as a resorbable biomaterial. RSC Advances 4:55677-55684

7. Xin R, Li B, Li L, Liu Q (2011) Influence of texture on corrosion rate of AZ31 Mg alloy in 3.5 wt.% NaCl. Materials and Design 32:4548-4552

8. Argade GR, Panigrahi SK, Mishra RS (2012) Effects of grain size on the corrosion resistance of wrought magnesium alloys containing neodymium. Corrosion science 58:145-151

9. Saha P, Roy M, Datta MK, Lee B, Kumta PN (2015) Effects of grain refinement on the biocorrosion and in vitro bioactivity of magnesium. Materials Science and Engineering C 57:294-303

10. Gao JH, Guan SK, Ren ZW, Sun YF, Zhu SJ, Wang B (2011) Homogeneous corrosion of high pressure torsion treated Mg–Zn–Ca alloy in simulated body fluid. Materials Letters 65:691-693

11. Valiev RZ, Islamgaliev RK, Alexandrov IV (2000) Bulk nanostructured materials from severe plastic deformation. Progress in Materials Science 45:103-187

12. Valiev RZ, Langdon TG (2006) Principles of equal-channel angular pressing as a processing toold for grain refinement. Progress in Materials Science 51:881-981

13. Zhilyaev AP, Langdon TG (2008) Using high-pressure torsion for metal processing: Fundamentals and applications Progress in Materials Science 53 (6):893-979

14. Birbilis N, Ralston KD, Virtanen S, Fraser HL, Davies CHJ (2010) Grain character influences on corrosion of ECAPed pure magnesium. Corrosion Engineering, Science and Technology 45:224-230

15. Figueiredo RB, Poggiali FSJ, Silva CLP, Cetlin PR, Langdon TG (2016) The influence of grain size and strain rate on the mechanical behavior of pure magnesium. Journal of Materials Science 51:3013-3024

16. Gan WM, Zheng MY, Chang H, Wang XJ, Qiao XG, Wu K, Schwebke B, Brokmeier H-G (2009) Microstructure and tensile property of the ECAPed pure magnesium. Journal of Alloys and Compounds 470:256-262

17. Yamashita A, Horita Z, Langdon TG (2001) Improving the mechanical properties of magnesium and a magnesium alloy through severe plastic deformation. Materials Science and Engineering A 300:142-147

18. Huang Y, Figueiredo RB, Baudin T, Brisset F, Langdon TG (2012) Evolution of Strength and Homogeneity in a Magnesium AZ31 Alloy Processed by High-Pressure Torsion at Different Temperatures. Advanced Engineering Materials 14 (11):1018-1026

19. Zhilyaev AP, Kim B-K, Nurislamova GV, Baró MD, Szpunar JA, Langdon TG (2002) Orientation imaging microscopy of ultrafine-grained nickel. Scripta Materialia 46 (8):575-580

20. Zhilyaev AP, Nurislamova GV, Kim B-K, Baró MD, Szpunar JA, Langdon TG (2003) Experimental parameters influencing grain refinement and microstructural evolution during high-pressure torsion. Acta Materialia 51 (3):753-765

21. Wongsa-Ngam J, Kawasaki M, Langdon TG (2013) A comparison of microstructures and mechanical properties in a Cu–Zr alloy processed using different SPD techniques. Journal of Materials Science 48 (13):4653-4660

22. Figueiredo RB, Langdon TG (2008) Record Superplastic Ductility in a Magnesium Alloy Processed by Equal-Channel Angular Pressing. Advanced Engineering Materials 10:37-40

23. Xia K, Wang JT, Wu X, Chen G, Gurvan M (2005) Equal channel angular pressing of magnesium alloy AZ31. Materials Science and Engineering A 410-411:324-327

24. Ge Q, Dellasega D, Demir AG, Vedani M (2013) The processing of ultrafine-grained Mg tubes for biodegradables stents. Acta Biomaterialia 9:8604-8610

25. Figueiredo RB, Sabbaghianrad S, Giwa A, Greer JR, Langdon TG (2017) Evidence for exceptional low temperature ductility in polycrystalline magnesium processed by severe plastic deformation. Acta Materialia 122:322-331.

26. Song D, Ma A, Jiang J, Lin P, Yang D, Fan J (2010) Corrosion behavior of equal-channel-angular-pressed pure magnesium in NaCl aqueous solution. Corrosion science 52:481-490

27. Wang H, Estrin Y, Fu H, Song G, Zúberová Z (2007) The Effect of Pre-Processing and Grain Structure on the Bio-Corrosion and Fatigue Resistance of Magnesium Alloy AZ31. Advanced Engineering Materials 9 (11):967-972

28. Alvarez-Lopez M, Pereda MD, del Valle JA, Fernandez-Lorenzo M, Garcia-Alonso MC, Ruano OA, Escudero ML (2010) Corrosion behaviour of AZ31 magnesium alloy with different grain sizes in simulated biological fluids. Acta Biomaterialia 6:1763-1771

29. Ralston KD, Birbilis N, Davies CHJ (2010) Revealing the relationship between grain size and corrosion rate of metals. Scripta Materialia 63:1201-1204

30. Iwahashi Y, Wang J, Horita Z, Nemoto M, Langdon TG (1996) Principle of equal-channel angular pressing for the processing of ultra-fine grained materials. Scripta Materialia 35 (2):143-146

31. Furukawa M, Iwahashi Y, Horita Z, Nemoto M, Langdon TG (1998) The shearing characteristics associated with equal-channel angular pressing. Materials Science and Engineering A 257 (2):328-332

32. Song G, Atrens A, StJohn D (2001) An hydrogen evolution method for the estimation of the corrosion rate of magnesium alloys. Magnesium Technology 2001:255-262

33. Metikoš-Hukovic M, Babic R, Grubac Z, Brinic S (1994) Impedance spectroscopic study of aluminium and Al-alloys in acid solution: inhibitory action of nitrogen containing compounds. Journal of Applied Electrochemistry 24:772-778

34. Farias CA, Lins VFC (2011) Corrosion Resistance of Steels Used in Alcohol and Sugar Industry. Chemical Engineering & Technology 34 (9):1393-1401

35. Shi Z, Liu M, Atrens A (2010) Measurement of the corrosion rate of magnesium alloys using Tafel extrapolation. Corrosion science 52:579-588

36. Hermawan H, Dubé D, Mantovani D (2010) Developments in metallic biodegradable stents. Acta Biomaterialia 6:1693-1697

37. Agnew SR, Horton JA, Lillo TM, Brown DW (2004) Enhanced ductility in strongly textured magnesium produced by equal channel angular processing. Scripta Materialia 50:377-381

38. Mukai T, Yamanoi M, Watanabe H, Higashi K (2001) Ductility enhancement in AZ31 magnesium alloy by controlling its grain structure. Scripta Materialia 45:89-94

39. Somekawa H, Mukai T (2015) Hall–Petch Breakdown in Fine-Grained Pure Magnesium at Low Strain Rates. Metallurgical and Materials Transactions 46A:894-902

40. Li J, Xu W, Wu X, Ding H, Xia K (2011) Effects of grain size on compressive behaviour in ultrafine grained pure Mg processed by equal channel angular pressing at room temperature. Materials Science and Engineering A 528:5993-5998

41. Agha NA, Willumeit-Römer R, Laipple D, Luthringer B, Feyerabend F (2016) The Degradation Interface of Magnesium Based Alloys in Direct Contact with Human Primary Osteoblast Cells. PLoS ONE 11 (6):e0157874

42. Figueiredo RB, Langdon TG (2010) Grain refinement and mechanical behavior of a magnesium alloy processed by ECAP. Journal of Materials Science 45:4827-4836

5. CAPÍTULO 5 – THE EFFECT OF HIGH-PRESSURE TORSION ON MICROSTRUCTURE, HARDNESS AND CORROSION BEHAVIOR FOR PURE MAGNESIUM AND DIFFERENT MAGNESIUM ALLOYS

Claudio P. Silva[a], Renata B. Soares[b], Pedro Henrique R. Pereira[a,c],

Roberto B. Figueiredo[a,*], Vanessa F. C. Lins[b], Terence G. Langdon[c]

[a] Department of Metallurgical and Materials Engineering, Universidade Federal de Minas Gerais, Belo Horizonte, MG 31270-901, Brazil
[b] Department of Chemical Engineering, Universidade Federal de Minas Gerais, Belo Horizonte, MG 31270-901, Brazil.
[c] Materials Research Group, Department of Mechanical Engineering, University of Southampton, Southampton SO17 1BJ, UK.
*Corresponding author: figueiredo@demet.ufmg.br

Abstract

Severe plastic deformation by high pressure torsion (HPT) was used to process and refine the grain structure of commercial purity magnesium and AZ31, AZ91 and ZK60 magnesium alloys. Transmission electron microscopy showed that the microstructure of pure magnesium was characterized by a bi-modal grain size distribution with grains in the range of a few microns and ultrafine grains after HPT whereas the magnesium alloys displayed a homogeneous ultrafine grain structure after processing. X ray diffraction analysis revealed that the AZ91 alloy displayed the largest lattice microstrain and this alloy also exhibited the highest hardness after processing. The processed AZ31 and the ZK60 alloys showed similar microstructures and maximum values of hardness. Contrary to earlier reports of significant improvements in the corrosion resistance of magnesium alloys in biological environments, the present results showed that processing by HPT had no significant effect on the corrosion behavior of magnesium alloys in a 3.5% NaCl solution. By contrast, pure magnesium exhibited an increased corrosion resistance after HPT.

Keywords: corrosion; hardness; high pressure torsion; magnesium; microstructure.

5.1 Introduction

There are many reports showing that grain refinement by severe plastic deformation (SPD) changes significantly the properties of magnesium and its alloys. Pure magnesium becomes extremely ductile at room temperature after processing using the SPD procedures of equal-channel angular pressing (ECAP) [1] or high pressure torsion (HPT) [2]. There is also some evidence that ECAP and HPT may affect the corrosion behavior. Thus, coarse-grained pure magnesium exhibits localized corrosion in NaCl whereas the fine-grained and ultrafine-grained (UFG) material displays more general corrosion [3]. Homogeneous corrosion in simulated body fluid was also reported in a Mg-Zn-Ca alloy processed by HPT [4, 5]. The processing technique of HPT increases the hardness of diverse magnesium alloys to values over 100 Hv [6-13] which are higher than the hardnesses observed after conventional thermo-mechanical processing.

Although many reports describe the microstructural and hardness evolution of different magnesium alloys after processing by HPT, a direct comparison between pure magnesium and representative different alloys is not yet available. Thus, the effects of the amount and type of the alloying elements on the microstructural refinement and hardness are not fully understood. Also, the corrosion behavior of different magnesium alloys in an aggressive media has not been reported to date. Accordingly, the objective of the present investigation was to make a direct comparison between the microstructural evolution, the hardness distribution and the corrosion properties in a 3.5% NaCl solution using pure magnesium and magnesium alloys with zinc (ZK60) and different amounts of aluminum (AZ31 and AZ91) as the main alloying elements.

5.2 Experimental materials and procedures

The materials used in this investigation were commercial purity magnesium (99.7% purity) and the AZ31, AZ91 and ZK60 alloys. The CP-Mg and the AZ91 alloy were received as cast ingots and the AZ31 and ZK60 alloys were received as extruded bars having diameters of 10 mm. The AZ91 alloy was subjected to a solution treatment at 693 K for 24 hours followed by water quenching to reduce the amount of second phase particles. The grain structures of these four materials, determined by conventional

metallographic procedure, are presented in Fig. 5.1. The cast CP-Mg exhibited a coarse structure with grains in the range of hundreds of micrometers including some grains in the millimeter range. The solution treatment was effective in reducing the amount of second phase and homogenization in the AZ91 alloy. The AZ31 and the ZK60 alloys exhibited refined grain structure as expected from the prior extrusion treatment. The average grain sizes, determined by the mean linear intercept method, were ~1 mm for the CP-Mg and ~16 μm for AZ31, ~110 μm for AZ91 and ~2.9 μm for the ZK60 alloy.

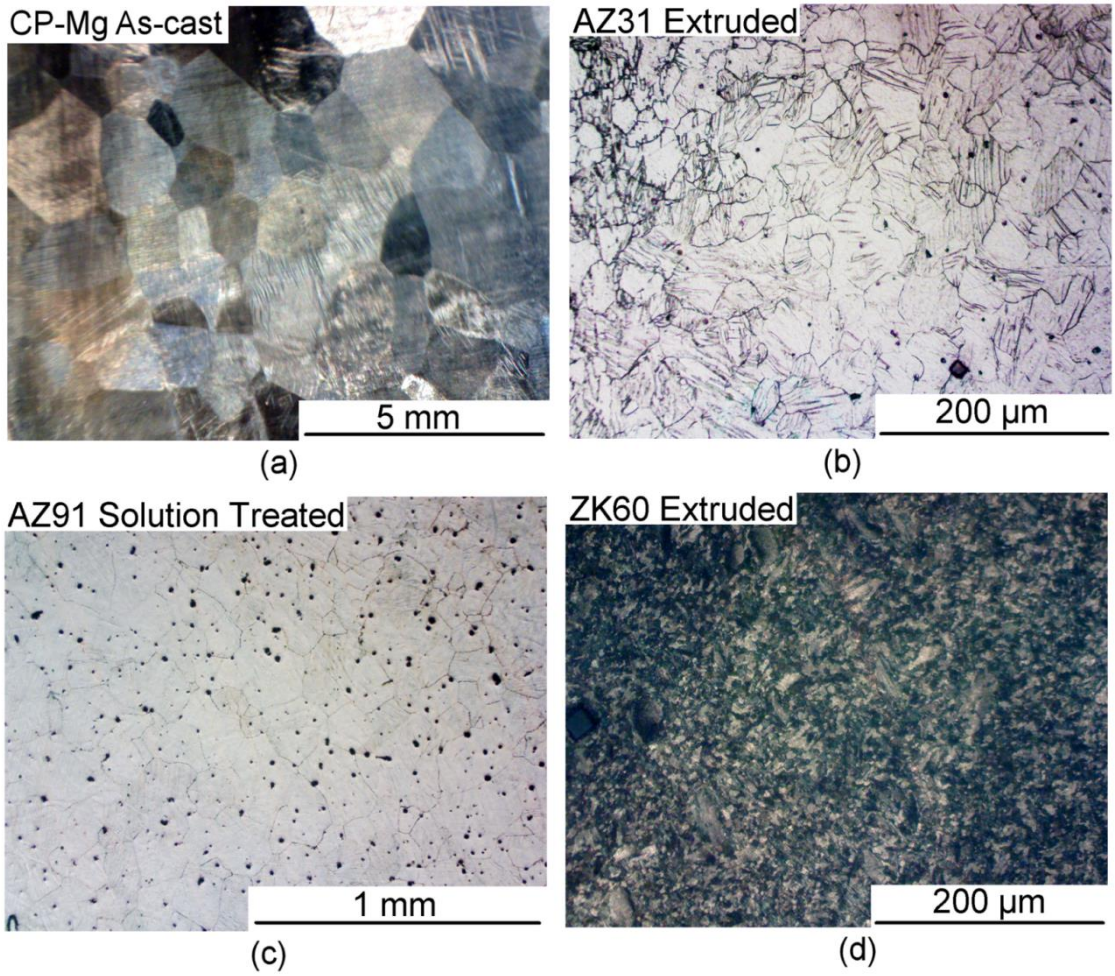

Figure 5.1 – Grain structure of the (a) as-cast CP-Mg and (b) extruded AZ31, (c) solution treated AZ91 and (d) extruded ZK60 alloys before processing by HPT.

Bars with 10 mm diameter were machined from the CP-Mg and the AZ91 alloy. Discs with ~0.9 mm thickness were cut from the bars of the four different materials and ground with #600 paper to final thicknesses of ~0.85 mm. These discs were used for

HPT processing to different number of turns at room temperature at a nominal pressure of 6.0 GPa. The thicknesses of the samples were reduced to 0.5 ~ 0.6 mm due to processing. The rotation rate was maintained constant at 2 rpm since this effectively limits the heating of the sample to less than ~50 K [14]. The HPT was conducted under quasi-constrained conditions where there is a small outflow of material around the periphery of the disc during the processing operation [15].

The microstructure of the processed material was investigated by transmission electron microscopy (TEM) and x ray diffraction (XRD) analysis. TEM samples from the CP-Mg and the AZ31 and ZK60 alloys were prepared by electro-polishing to perforation using a Tenupol. A solution of 5% perchloric acid and ethanol at T = 30 °C was used for the polishing. Despite several attempts, including the use of different solutions, the electro-polishing technique failed to provide a good transparent area in the AZ91 alloy. Therefore, a TEM sample of this alloy was prepared using the focused ion beam technique leading to a smaller area for investigation. All samples were prepared from the mid-radius positions of the processed discs. All samples were prepared from the mid-radius positions of the processed discs. The samples were observed in an FEI Tecnai G2-20 microscope operating at 200 kV. Samples for XRD were prepared by grinding with #600, #1200 and #2500 grit papers and polishing to 1 μm diamond paste. The whole surface of the disc was prepared and the analysis was carried out with a Philips PW1710 diffractometer using Cu Kα radiation and a graphite monochromatic crystal with a wavelength of 1.5406 Å. The MAUD software was used to analyze the diffraction profile and to determine the crystallite size and microstrain through Rietveld refinement. The agreement between the simulated profile and the experimental data was monitored through the goodness of fitness (Sig in MAUD software) which was smaller than 3 in all conditions.

Previous reports have shown that the hardness distributions may be heterogeneous in magnesium alloys processed by HPT [16, 17]. Therefore the hardness distribution was determined along the through-thickness and radial planes to evaluate the degree of homogeneity along the thickness of each sample. The hardness measurements were taken using a dynamic hardness tester SHIMADZU DUH-211 with a Berkovich indenter, a loading rate of ~70 mN/s and a maximum load of 200 mN. A

grid with 50 indentations was used to determine the hardness distribution map for each sample.

The corrosion behavior of the different alloys before and after HPT processing was evaluated by electro-chemical polarization and impedance spectroscopy tests in a 3.5 wt% NaCl solution. An Autolab potentiostat model PGSTAT 100N with 3 electrodes (Ag/AgCl as a reference, platinum as counter-electrode and the samples as the work electrode) was used for the tests. The disc samples for corrosion testing were ground with #4000 grit paper and the samples were immersed in the solution for 600 s in order to stabilize the potential before testing. A scan rate of 1 mV s^{-1} was used for the polarization tests and an amplitude of 10 mV in relation to the open circuit potential was used in the spectroscopy impedance tests in the frequency range of 10 kHz – 10 mHz.

5.3 Experimental results

5.3.1 Microstructure

Figure 2 shows representative images of the grain structures of the different materials after processing by HPT. The CP-Mg in Fig. 2(a) is characterized by grains having different sizes such that areas of grains of hundreds of nanometers and areas of grains larger than a micrometer are clearly distinguished. A similar bimodal grain structure was reported earlier in other experiments on pure magnesium [18-20] and can be attributed to recrystallization [19]. A dark field image is also shown in the right column to facilitate the distinction of some of the ultrafine grains. Selected area electron diffraction revealed a ring shaped pattern indicating a high misorientation between the grains. The dark field image was obtained by selecting (100) plane family reflections. The average grain size, determined as the average of the individual grains, was ~510 nm and this is slightly larger than the value of the mean linear intercept length (~320 nm) determined by EBSD in a similar material [2]. The grain sizes of the magnesium alloys processed by HPT are significantly smaller than CP-Mg. Thus, the AZ31 alloy in Fig. 2(b) exhibits a homogeneous distribution of ultrafine grains and the bright field image reveals grains in the range of ~100 ~ 500 nm. A dark-field image shows one grain with ~200 nm of size. The average grain size in this alloy was determined as ~130 nm and this is consistent with earlier reports of the grain structure in the AZ31 alloy processed

by HPT [6, 7]. Despite the small transparent area available in the sample of AZ91, it was possible to distinguish grains having different sizes. It was also apparent that grains smaller than ~100 nm and larger than ~100 nm co-existed in the same area. The average grain size was not easily determined for the AZ91 alloy due to the small amount of available data but nevertheless it was estimated as ~100 nm. Energy dispersive X-ray spectroscopy (EDS) was used to estimate the compositions at different locations in the AZ91 and the results showed a composition of Mg-9 wt.% Al at point 2 in Fig. 2(c) and Mg-22 wt.% Al at point 1. This suggests that a small second phase particle is present near point 1. The grain structure of the ZK60 alloy was reasonably homogeneous after HPT with an average grain size of ~160 nm. Some very small second phase particles were homogeneously distributed at the grain boundaries and within the grains as shown in the higher magnification image in Fig. 2(d). Similar particles were observed after severe plastic deformation by ECAP in a similar alloy [21]. The high stresses and severe plastic deformation can break up second phase leading to the formation of smaller particles.

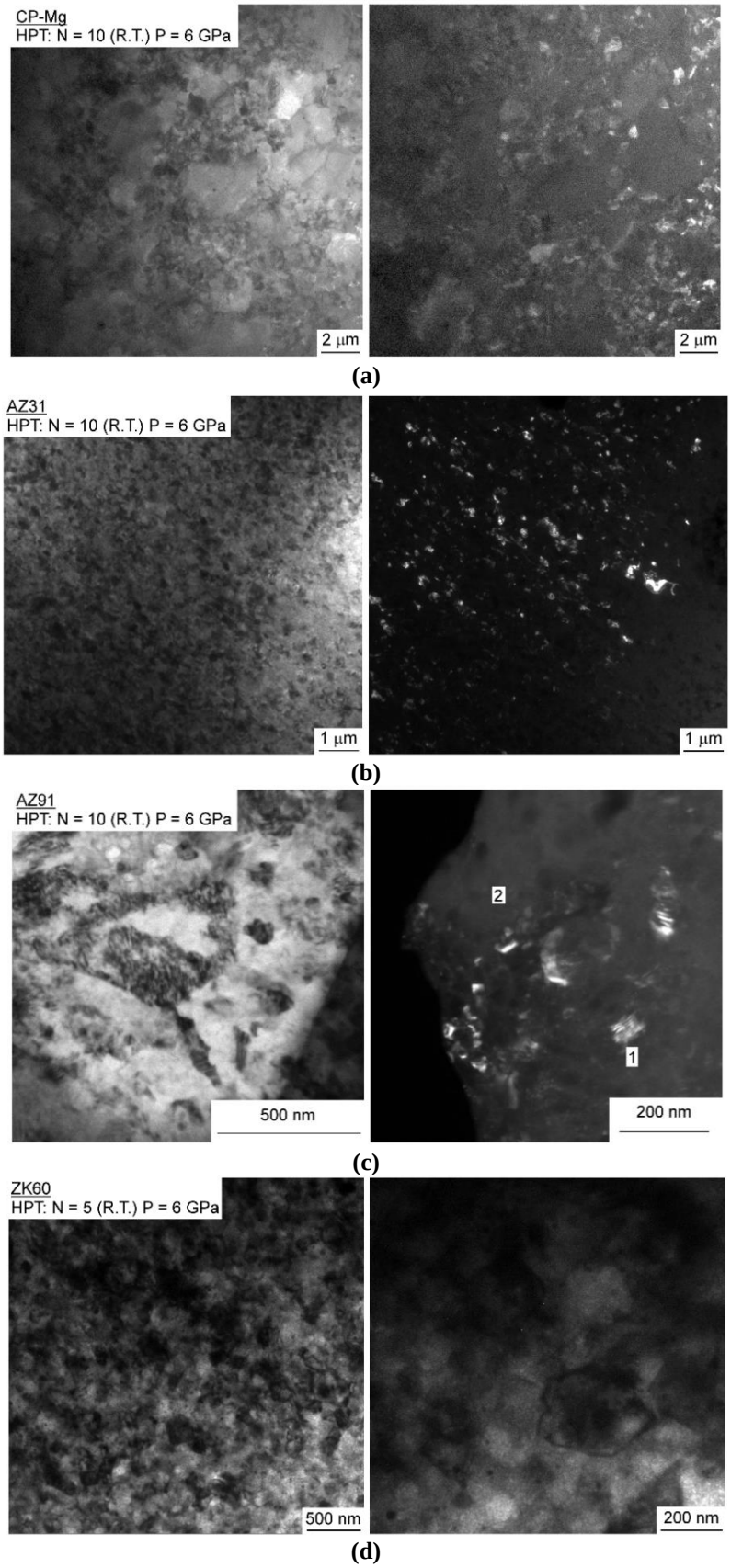

Figure 5.2 – Grain structure of the (a) CP-Mg and the (b) AZ31, (c) AZ91 and (d) ZK60 alloys after processing by HPT.

The XRD profiles of the samples before and after different numbers of HPT turns are shown in Fig. 5.3 where the upper profiles in each plot labeled $N = 0$ denote measurements taken in the unprocessed material. The planes associated with the various peaks may be described with reference to the CP-Mg data since it is readily apparent from Fig. 5.3(a) that the positions of the peaks for CP-Mg are not significantly affected by the HPT processing. By contrast, the magnesium alloys in Figs 5.3(b-d) show a very significant broadening of the peaks after HPT which is directly attributed to a reduction in the crystallite size and an increase in the microstrain within the lattice. These effects were also simulated using the MAUD software and the simulated diffraction profiles are also plotted as continuous lines together with the experimental data shown as open symbols. The agreement between the simulated and experimental data is clearly seen in a magnified plot over the 2Θ range of 30~40° for the AZ31 alloy in Fig. 5.3(b). The AZ31 and the ZK60 alloys exhibit higher intensities for the (100) peaks before HPT processing and this is due to texture effects that are a direct consequence of the earlier processing by extrusion. The HPT processing promotes an increase in intensity of the (002) and (101) peaks in all samples and minor peaks associated with a second phase are visible in the AZ91 and ZK60 alloys. Examination shows that these peaks agree with the expected patterns for the $Al_{12}Mg_{17}$ and $MgZn_2$ phases, respectively. It should be noted that the $Al_{12}Mg_{17}$ peaks were very small in the AZ91 alloy before processing but their intensity increased after HPT, thereby indicating that the solution treated alloy undergoes precipitation during HPT. An earlier report documented precipitation during SPD by ECAP in a solution-treated AZ91 alloy [22].

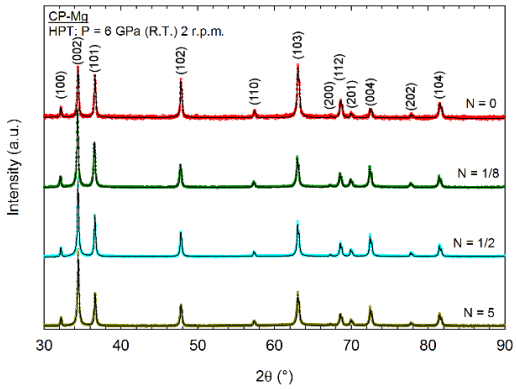

(a)

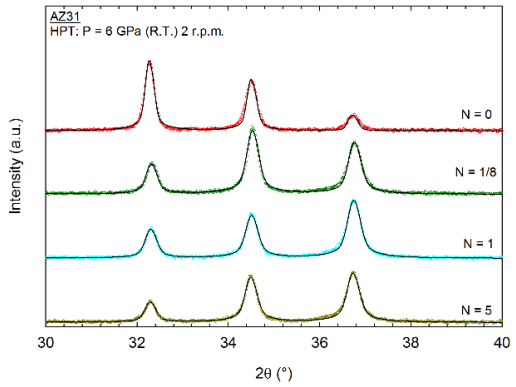

(b)

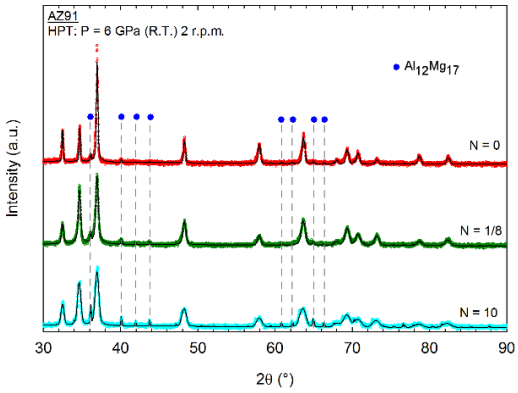

(c)

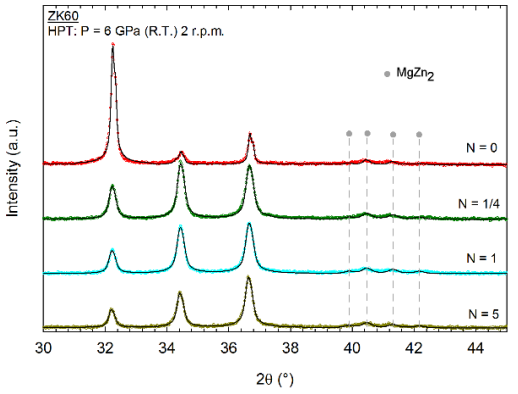

(d)

Figure 5.3 – XRD profiles of the (a) CP-Mg and (b) AZ31, (c) AZ91 and (d) ZK60 alloys before and after HPT processing.

The values of the crystal structure parameters determined by XRD are summarized in Table 5.1. The crystallite size after HPT processing was larger for CP-Mg than for the magnesium alloys which is in qualitative agreement with the TEM data. The AZ91 alloy exhibits slightly smaller values for the cell size parameters, *a* and *c*, and the microstrain, which is associated with the distortion of the crystalline structure and is related to the dislocation density, is lower in CP-Mg and larger in the AZ91 alloy. This shows that increasing the solid solution content increases the maximum microstrain after HPT. It is worth noting that the lattice microstrain increases in the initial stage of HPT processing and decreases slightly at larger number of turns in the AZ31 and ZK60 alloys. A decrease in microstrain was also reported in a ZK60 alloy [23] and a decrease in dislocation density was reported in an AZ31 alloy [7] processed by HPT to large number of turns. This effect is attributed to the onset of contribution of grain boundary sliding to the deformation [23].

Table 5.1– Crystallite size, d_{XRD}, crystal parameters a and c and microstrain, ε, determined by XRD for the magnesium alloys before and after HPT processing.

Material	N	d_{XRD} (nm)	a (nm)	c (nm)	$\varepsilon \times 10^{-4}$
CP-Mg	0	239	0.32103	0.52111	4.78
	1/8	193	0.32136	0.52148	3.21
	1/2	227	0.32138	0.52144	3.09
	5	206	0.32138	0.52152	4.10
AZ31	0	312	0.32021	0.51969	11.63
	1/8	142	0.31980	0.51935	16.60
	1	120	0.31992	0.51965	16.61
	5	119	0.32005	0.51988	15.41
AZ91	0	530	0.31814	0.51688	11.22
	1/8	107	0.31822	0.51727	20.81
	10	141	0.31827	0.51795	39.96
ZK60	0	434	0.32029	0.52018	3.23
	1/4	147	0.32059	0.52052	11.94
	1	133	0.32064	0.52067	11.57
	5	133	0.32081	0.52086	8.69

5.3.2 Hardness

The hardness distributions for the different materials are presented in Fig. 5.4 for (a) CP-Mg, (b) AZ31, (c) AZ91 and (d) ZK60. These color-coded maps have different hardness scales for the various materials due to significant differences in the hardness values but the scale for each material is shown at the upper right. A reasonable level of heterogeneity in the hardness distributions in the through-thickness directions (the vertical directions in the plots) is apparent in all samples with larger heterogeneity for the AZ31 alloy. Heterogeneity in the hardness distribution was already reported in this alloy [16, 24] which suggests that the alloy is more susceptible to deformation localization. An increase in the numbers of turns reduces the level of heterogeneity in the AZ91 and ZK60 alloys. This agrees with an earlier report of good homogeneity in the hardness distribution on the disc surface of a ZK60 alloy processed by HPT [11] and it indicates that deformation localization is less important in this alloy. Overall, it appears that the hardness does not change significantly after 1 turn of HPT in all materials tested.

In order to evaluate the hardening behavior of the different materials, the average hardness along the through-thickness direction is plotted as a function of the effective strain in Fig. 5.5. The effective strain, ε, was calculated as $\varepsilon = 2\pi Nr/\sqrt{3}h$, where N is the number of turns, r is the distance from center and h is the sample thickness [25]. The CP-Mg and the AZ31 alloy display a very short hardening stage such that the saturation takes place at strains <10. This short hardening in the AZ31 alloy agrees with an earlier observation in this alloy processed by HPT [6] but in pure magnesium there may be a very short hardening stage followed by softening and saturation [19]. Nevertheless, a peak hardening is not apparent in the present data and this may be due to the different hardness testing conditions. For example, it was shown that HPT processing of pure magnesium leads to the activation of grain boundary sliding at room temperature which causes the occurrence of room temperature creep [2]. Conventional microhardness testing is associated with a dwell time in which the load is applied to the sample so that room temperature creep may be activated to increase the depth of the indentation and thereby decrease the measured hardness in the microhardness testing. In the present work the dynamic hardness tests had no dwell time

so that the effect of creep was minimized and this directly explains the absence of a softening stage in the curve of hardness versus strain.

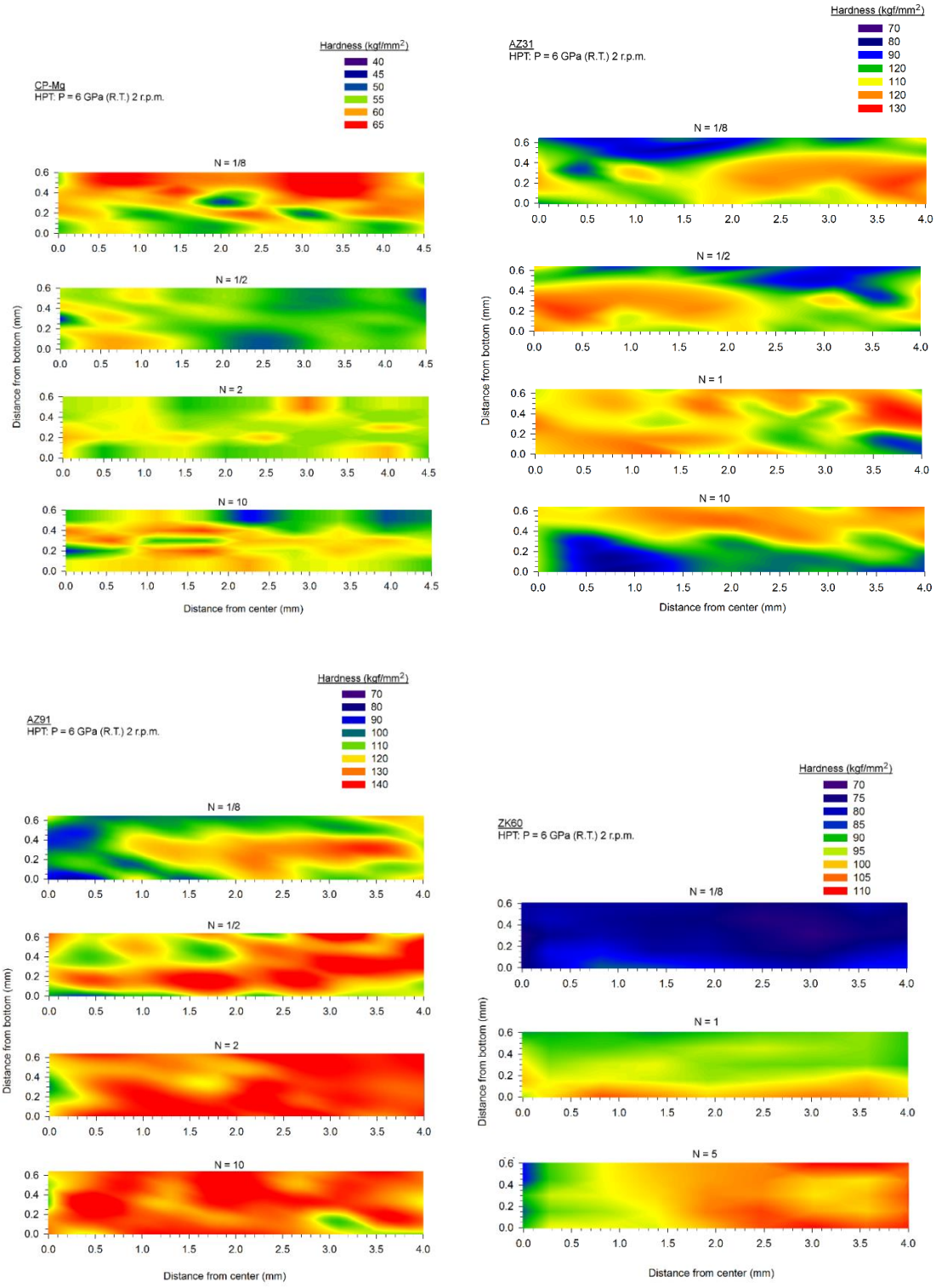

Figure 5.4 – Hardness distribution maps for the (a) CP-Mg and (b) AZ31, (c) AZ91 and (d) ZK60 alloys at different stages of HPT processing.

The AZ91 and the ZK60 alloys present a broader hardening stage up to strains of >20. Previous reports described strain hardening up to strains of ~20 in ZK60 [9, 26] and a broad strain hardening in the AZ91 alloy [27]. It is known that hardening is effective in preventing deformation localization and this agrees with the higher homogeneity of the hardness distribution in these alloys compared to the AZ31 alloy. It is noted also that the AZ91 alloy exhibits the highest hardness after HPT in Fig. 5 and this is followed by AZ31 and ZK60. The CP-Mg is the softer material after HPT as expected for a reasonably pure material. Although the ZK60 is considered a high strength alloy and the AZ31 is considered of medium strength [25], the present results show that the Al-rich alloys (AZ31 and AZ91) display higher strength after strain hardening than the Zn-rich alloy.

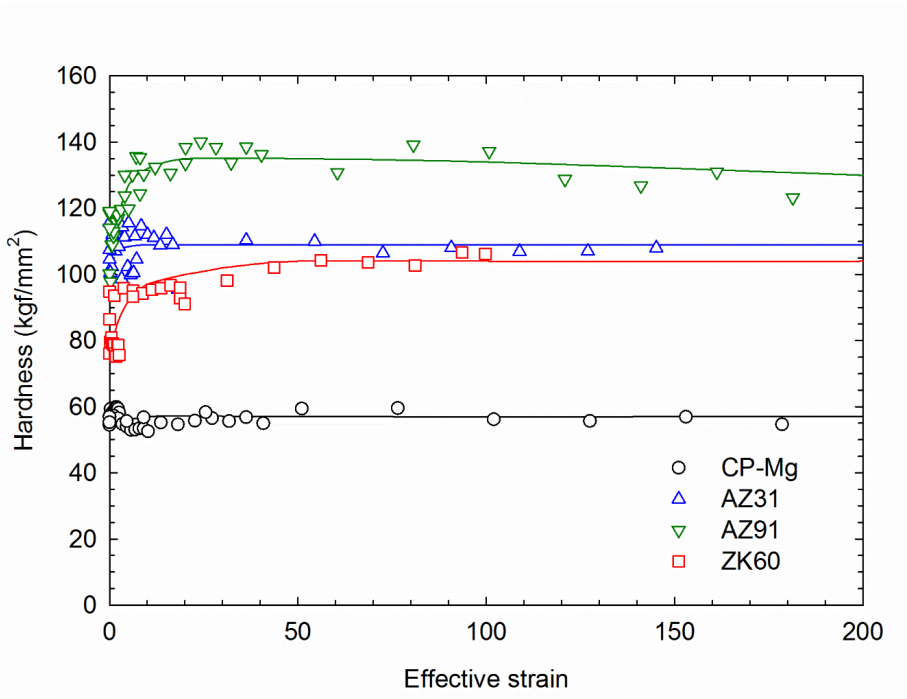

Figure 5.5 – Evolution of hardness as a function of the effective strain in the CP-Mg, AZ31, AZ91 and ZK60 alloys processed by HPT.

5.3.3 Corrosion

Figure 5.6 shows the potential vs. current curves determined by the potentiodynamic polarization tests in the different materials before and after HPT

processing. The samples processed by HPT were subjected to 10 turns each. The corrosion potential is higher in the alloys compared to the CP-Mg indicating a positive effect of the alloying elements. HPT processing does not affect the overall shapes of the curves of the unprocessed materials. The CP-Mg and the AZ31 and AZ91 alloys display a range of potentials with low variations in the current. This effect is more pronounced in the AZ91 and it suggests the formation of a protective layer of a corrosion product. This stage is not visible in the ZK60 alloy suggesting a more homogeneous corrosion in this material. This is in agreement with the polarization curve reported for this alloy in a similar solution [29]. The electrochemical parameters are summarized in Table 2 including the penetration rate estimated from the corrosion current. The corrosion current observed in the ZK60 alloy is lower than values reported earlier [29, 30] and this is attributed to the prior thermo-mechanical processing of this alloy by extrusion which is expected to decrease the corrosion current [31].

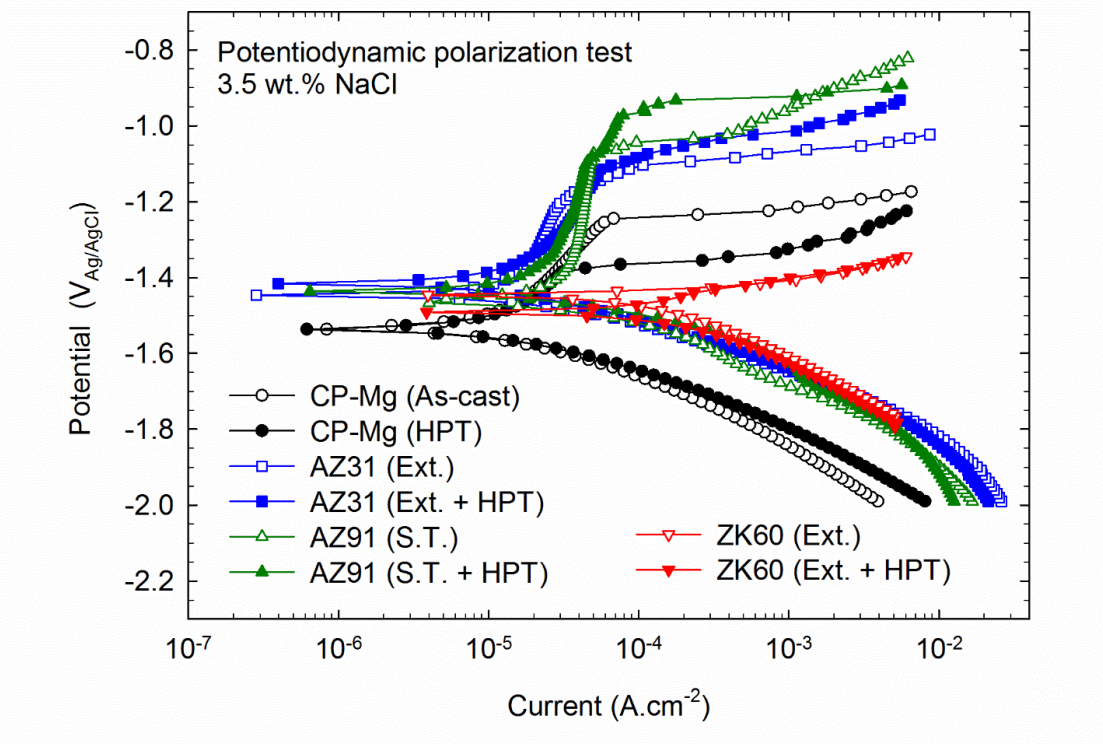

Figure 5.6 – Potentiodynamic polarization curves in 3.5% NaCl solution for the CP-Mg, AZ31, AZ91 and ZK60 alloys before and after HPT processing.

Table 5.2 – Summary of corrosion potential (E_{Corr}), current density (i_{Corr}) and penetration rate (P_i), determined by potendiodinamic polarization tests.

Material and condition		E_{Corr} ($V_{Ag/AgCl}$)	i_{Corr} ($\mu A.cm^{-2}$)	P_i ($mm.y^{-1}$)
CP-Mg	As-cast	-1.54 ± 0.01	18 ± 5	0.4 ± 0.1
CP-Mg	HPT	-1.55 ± 0.02	13 ± 1	0.30 ± 0.02
AZ31	Ext.	-1.44 ± 0.03	16 ± 2	0.37 ± 0.04
AZ31	Ext. + HPT	-1.42 ± 0.03	17 ± 2	0.39 ± 0.04
AZ91	S.T.	-1.46 ± 0.01	36 ± 15	0.8 ± 0.3
AZ91	S.T. + HPT	-1.46 ± 0.02	28 ± 7	0.6 ± 0.2
ZK60	Ext.	-1.48 ± 0.09	110 ± 30	2.5 ± 0.7
ZK60	Ext. + HPT	-1.44 ± 0.02	150 ± 20	3.4 ± 0.5

The Nyquist plots for all samples are depicted in Fig. 5.7(a) for conditions before and after HPT processing. There are significant differences in the diameters of the capacitive arcs between the samples. Thus, the diameters of the arcs for the AZ31 and ZK60 alloys are significantly smaller than for the CP-Mg and AZ91 alloy. Therefore, a second plot is shown in Fig. 5.7(b) with a smaller scale. It is apparent that the ZK60 alloy presents the smallest arc followed by the AZ31 alloy but both alloys also exhibit an inductive arc suggesting adsorption of the ionic species or pitting formation during the test [29, 30]. The result for the as-cast CP-Mg is in reasonable agreement with earlier reports for a similar solution [34, 35].

However, the AZ91 alloy exhibits a larger arc than CP-Mg which disagrees with an earlier study [31] and this difference is attributed to the solution treatment processing of the AZ91 in the present experiments. This solution treatment will increase the aluminum content in the magnesium matrix and decrease the amount of second phase particles and both of these effects will enhance the corrosion resistance. It is worth noting that HPT processing has no significant effect on the shape and size of the plots for the different materials. An increase in the diameter of the arc due to HPT processing was only observed in the CP-Mg which agrees with earlier results for this material [3].

A decrease in the arc diameter was observed in the AZ91 alloy after HPT processing while the AZ31 and the ZK60 alloys showed no significant difference.

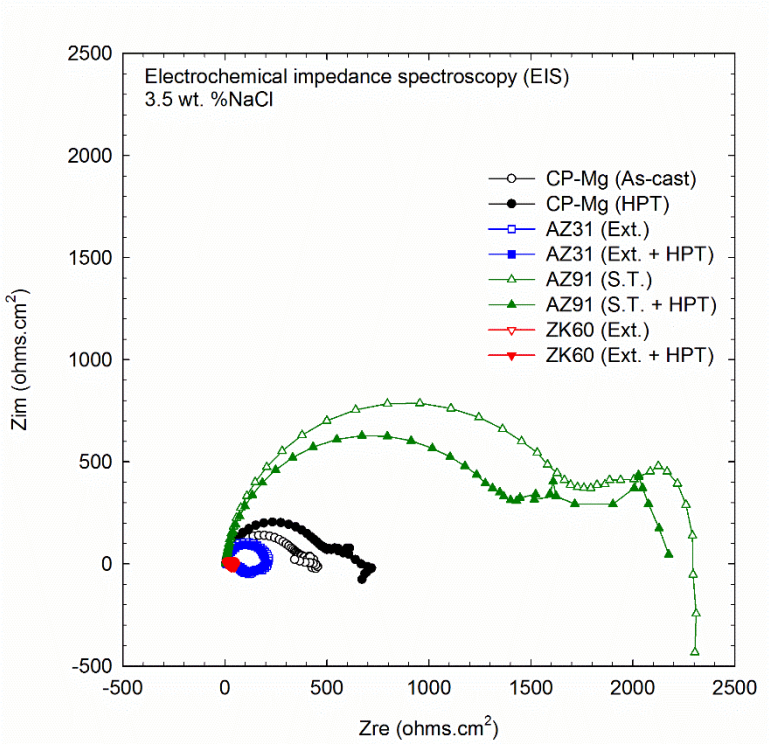

(a)

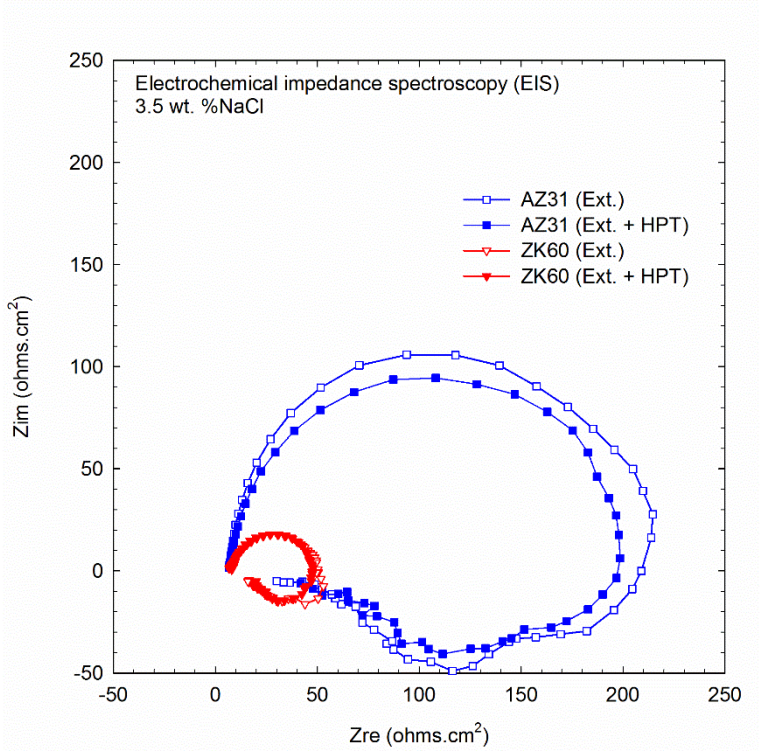

(b)

Figure 5.7 – Nyquist plots in 3.5% NaCl solution for the CP-Mg, AZ31, AZ91 and ZK60 alloys before and after HPT processing.

5.4 Discussion

It is widely known that severe plastic deformation by high pressure torsion refines the grain structure of magnesium and magnesium alloys and increases the hardness. The present results confirm this trend as samples with initial grain sizes of several microns were refined to the submicrometer range and hardness values over 100 kgf mm^{-2} were obtained. The present results also provide supporting evidence for comparing different commercial magnesium alloys. Although the initial condition of the different alloys varied (ranging from as cast to solution treated and extruded conditions), processing by HPT was carried out through a large number of turns so that hardness evolution essentially saturated. Also, the microstructure and hardness are in agreement which shows that a saturation in microstructural refinement was achieved in all materials.

The TEM analysis confirmed the formation of a bi-modal grain size distribution, with grains over 1 μm and ultrafine grains in the commercial purity magnesium after HPT processing. However, micrometer-sized grains were not observed in the magnesium alloys after HPT. Instead, the microstructure was more homogeneous in the AZ31 and ZK60 alloys with grains in the range ~100 – 500 nm. These alloys also exhibited similar values of lattice microstrain of ~1.0×10^{-3} and with the hardness saturating within a narrow range of ~105 – 110 kgf mm^{-2} after HPT processing. These results suggest that the AZ31 and ZK60 alloys display similar grain refinement and mechanical strength after HPT. Nevertheless, AZ91 with the higher aluminum content displayed significant differences in the microstructure and hardness after HPT. TEM analysis revealed the presence of a significant number of grains smaller than ~100 nm after 10 turns and the microstrain was determined by XRD as about three times larger than the average for the AZ31 and ZK60 alloys. These finer grain structures and higher lattice microstrains are consistent with the higher hardness in the AZ91 alloy.

Despite the significant changes in the microstructure and hardness, the HPT processing revealed no significant effect on the corrosion behavior of these materials in a 3.5% NaCl solution compared to the unprocessed materials. The electro-chemical results in the present work differ slightly from earlier reports. For example, the corrosion currents for the AZ31 and the ZK60 alloys are lower than reports for these

alloys [30, 34] and this difference is attributed to the previous thermo-mechanical processing by extrusion of these alloys in the present experiments which is expected to homogenize the microstructure and enhance the corrosion resistance [31]. Further processing of these alloys by HPT failed to significantly change the electro-chemical results which suggests that there is a saturation in the increase in corrosion resistance by thermo-mechanical processing.

The results for the AZ91 alloy differs significantly from reports for this alloy in the cast condition or after ECAP processing. Although the corrosion current in the present experiments was in a similar range to that observed in a 3.5% NaCl solution in the as-cast material [34, 36], it is lower than observed in this material after processing by ECAP [36]. A major difference is observed in the impedance spectroscopy test. Thus, the arc for the AZ91 alloy in the present experiments is significantly larger than reported for the as-cast [32,34] and ECAP-processed materials [36]. These differences are attributed to the preliminary solid solution treatment in the present experiments. It has been shown that the corrosion current, which is considered proportional to the corrosion rate, increases with an increase in the fraction of β phase in this alloy [37]. This Al-rich phase is nobler than the α matrix phase and may accelerate the degradation of the matrix. Thus, the solid solution treatment decreases the amount of β phase in the alloy and increases the Al content in the α phase.

It is worth noting that severe plastic deformation by ECAP deteriorates significantly the corrosion resistance of the AZ91 alloy [36] because this processing operation, as in most of the thermo-mechanical processing of this alloy, needs to be conducted at moderate or high temperatures and this leads to significant precipitation of the β phase during processing. By contrast, high-pressure torsion can be conducted at room temperature which limits the precipitation of the second phase. A slight increase in the fraction of β phase due to HPT processing was detected by XRD in the present experiments and this explains the decrease in the corrosion resistance of the AZ91 alloy as evident in the impedance spectroscopy test. However, it is important to note that the diameter of the capacitive arc for this alloy after HPT processing remains significantly larger than observed in this material in the as-cast condition or after ECAP processing. Therefore, HPT processing of the solution-treated AZ91 alloy is an effective method for improving the mechanical properties without compromising the corrosion resistance.

The only material processed by HPT in these experiments without any previous thermal or thermo-mechanical processing was the CP-Mg. Previous reports document a reduction in corrosion resistance of cast pure magnesium after processing by hot-rolling [3] and by ECAP at high temperatures [35]. However, this material exhibits an increase in the capacitive arc after room temperature HPT processing which suggests an increase in the corrosion resistance. This is in agreement with earlier results for this material after processing by HPT [3].

There are many reports of significant improvements in the corrosion resistance of magnesium alloys due to HPT processing but these reports of corrosion behavior are generally for magnesium alloys in solutions that simulate biological environments [4,5,39,40]. The present results show no clear improvement in the corrosion resistance in a 3.5 wt% NaCl solution for magnesium alloys processed previously by extrusion or through a solution treatment. Thus, it is reasonable to conclude that HPT processing is more effective in improving the corrosion resistance of magnesium alloys when testing in less aggressive environments.

5.5 Summary and conclusions

1- Commercial purity magnesium (CP-Mg) and commercial alloys AZ31, AZ91 and ZK60 were processed by high-pressure torsion. The structure and hardness evolution were determined before and after HPT processing together with the corrosion behavior in a 3.5% NaCl solution.

2- Pure magnesium exhibits coarser average grain size and a bimodal grain distribution after HPT processing. The magnesium alloys AZ31 and ZK60 display homogeneous grain size distributions with final grain sizes of ~130 and ~160 nm respectively. The AZ91 alloy contains a large fraction of grains smaller than 100 nm after HPT.

3- The microstructural evolution, final grain sizes and maximum hardness values are similar in the AZ31 and ZK60 alloys. The hardening of the ZK60 alloy takes place over a broader deformation range and leads to a more homogeneous hardness distribution. The AZ91 alloy has a finer structure with a more distorted lattice and a higher hardness than in the other magnesium alloys and pure magnesium.

4- High-pressure torsion improves the corrosion resistance of cast pure magnesium but has no significant effect on the corrosion behavior of extruded AZ31 and ZK60 magnesium alloys when testing in a 3.5% NaCl solution.

5- The AZ91 alloy displays the largest capacitive arc among the materials tested and this is attributed to the small fraction of β phase in the microstructure. The processing by HPT at room temperature limited the precipitation of this phase during the processing operation and this led to a minor decrease in the capacitive arc.

5.6 Acknowledgements

The authors would like to acknowledge the Center of Microscopy at the Universidade Federal de Minas Gerais (http://www.microscopia.ufmg.br) for providing the equipment and technical support for experiments involving electron microscopy. This study was funded by CNPq (grant #400407/2016-7) and FAPEMIG (grant # APQ-00580-15). RBS has received a research fellowship from CAPES.

5.7 References

1. R. B. Figueiredo, F. S. J. Poggiali, C. L. P. Silva, P. R. Cetlin, and T. G. Langdon, *Journal of Materials Science*, 2016, 51, 3013.

2. R. B. Figueiredo, S. Sabbaghianrad, A. Giwa, J. R. Greer, and T. G. Langdon, *Acta Materialia*, 2017, 122, 322.

3. C. L. P. Silva, A. C. Oliveira, C. G. F. Costa, R. B. Figueiredo, M. de Fátima Leite, M. M. Pereira, V. F. C. Lins, and T. G. Langdon, *Journal of Materials Science*, 2017, 52, 5992.

4. C. Z. Zhang, S. K. Guan, L. G. Wang, S. J. Zhu, and L. Chang, *Journal of Materials Research*, 2017, 32, 1061.

5. J. H. Gao, S. K. Guan, Z. W. Ren, Y. F. Sun, S. J. Zhu, and B. Wang, *Materials Letters*, 2011, 65, 691.

6. J. Xu, X. W. Wang, M. Shirooyeh, G. N. Xing, D. B. Shan, B. Guo, and T. G. Langdon, *Journal of Materials Science*, 2015, 50, 7424.

7. J. Straska, M. Janecek, J. Gubicza, T. Krajnak, E. Y. Yoon, and H. S. Kim, *Materials Science and Engineering a-Structural Materials Properties Microstructure and Processing*, 2015, 625, 98.

8. A. Al-Zubaydi, R. B. Figueiredo, Y. Huang, and T. G. Langdon, *Journal of Materials Science*, 2013, 48, 4661.

9. S. A. Torbati-Sarraf, S. Sabbaghianrad, R. B. Figueiredo, and T. G. Langdon, *Journal of Alloys and Compounds*, 2017, 712, 185.

10. H. J. Lee, S. K. Lee, K. H. Jung, G. A. Lee, B. Ahn, M. Kawasaki, and T. G. Langdon, *Materials Science and Engineering a-Structural Materials Properties Microstructure and Processing*, 2015, 630, 90.

11. S. A. Torbati-Sarraf and T. G. Langdon, *Journal of Alloys and Compounds*, 2014, 613, 357.

12. D. X. X. Liu, X. Pang, D. L. L. Li, C. G. G. Guo, J. Wongsa-Ngam, T. G. Langdon, and M. A. Meyers, *Advanced Engineering Materials*, 2017, 19.

13. E. A. Lukyanova, N. S. Martynenko, I. Shakhoya, A. N. Belyakov, L. L. Rokhlin, S. V. Dobatkin, and Y. Z. Estrin, *Materials Letters*, 2016, 170, 5.

14. P. H. R. Pereira, R. B. Figueiredo, Y. Huang, P. R. Cetlin, and T. G. Langdon, *Materials Science and Engineering A*, 2014, 593, 185.

15. R. B. Figueiredo, P. H. R. Pereira, M. T. P. Aguilar, P. R. Cetlin, and T. G. Langdon, *Acta Materialia*, 2012, 60, 3190.

16. R. B. Figueiredo, M. T. P. Aguilar, P. R. Cetlin, and T. G. Langdon, *Metallurgical and Materials Transactions A: Physical Metallurgy and Materials Science*, 2011, 42, 3013.

17. R. B. Figueiredo and T. G. Langdon, *Materials Science and Engineering A*, 2011, 528, 4500.

18. B. J. Bonarski, E. Schafler, B. Mingler, W. Skrotzki, B. Mikulowski, and M. J. Zehetbauer, *Journal of Materials Science*, 2008, 43, 7513.

19. K. Edalati, A. Yamamoto, Z. Horita, and T. Ishihara, *Scripta Materialia*, 2011, 64, 880.

20. D. Ahmadkhaniha, Y. Huang, M. Jaskari, A. Järvenpää, M. H. Sohi, C. Zanella, L. P. Karjalainen, and T. G. Langdon, *Journal of Materials Science*, 2018, 53, 16585.

21. B. Li , S. Joshi, K. Azevedo, E. Ma, K.T. Ramesh, R.B. Figueiredo, T.G. Langdon, *Materials Science and Engineering A,* 2009, 517, 24.

22. K. N. Braszczyńska-Malik, *Journal of Alloys and Compounds*, 2009, 487, 263.

23. A. Galiyev, R. Kaibyshev, *Materials Transactions*, 2001, 42, 1190

24. R. B. Figueiredo, M. Kawasaki, and T. G. Langdon, *Acta Physica Polonica A*, 2012, 122, 425.

25. R.Z. Valiev,Yu.V. Ivanisenko, E.F. Rauch, B. Baudelet, *Acta Materialia,* 1996, 44, 4705.

26. H. J. Lee, B. Ahn, M. Kawasaki, and T. G. Langdon, *Journal of Materials Research and Technology-Jmr&T*, 2015, 4, 18.

27. A. S. J. Al-Zubaydi, A. P. Zhilyaev, S. C. Wang, P. Kucita, and P. A. S. Reed, *Journal of Materials Science*, 2016, 51, 3380.

28. I. J. Polmear, *Materials Science and Technology*, 1994, 10, 1.

29. Z. Z. Qiu, R. Wang, Y. S. Zhang, Y. F. Qu, and X. H. Wu, *Journal of Materials Engineering and Performance*, 2015, 24, 1483.

30. P. Su, X. Wu, Y. Guo, and Z. Jiang, *Journal of Alloys and Compounds*, 2009, 475, 773.

31. D. Orlov, K. D. Ralston, N. Birbilis, and Y. Estrin, *Acta Materialia*, 2011, 59, 6176.

32. M. Metikoš-Huković, R. Babić, Z. Grubač, and S. Brinć, *Journal of Applied Electrochemistry*, 1994, 24, 772.

33. C. A. Farias and V. F. C. Lins, *Chemical Engineering & Technology*, 2011, 34, 1393.

34. I. B. Singh, M. Singh, and S. Das, *Journal of Magnesium and Alloys*, 2015, 3, 142.

35. D. Song, A. Ma, J. Jiang, P. Lin, D. Yang, and J. Fan, *Corrosion science*, 2010, 52, 481.

36. D. Song, A. B. Ma, J. H. Jiang, P. H. Lin, D. H. Yang, and J. F. Fan, *Corrosion Science*, 2011, 53, 362.

37. M. Hatakeyama, K. Shimono, D. Iwashima, S. Saikawa, and S. Sunada, *Archives of Metallurgy and Materials*, 2017, 62, 155.

38. K.D. Ralston, N. Birbilis, C.H.J. Davies, *Scripta Materialia*, 2010, 63, 1201.

39. C. Z. Zhang, S. J. Zhu, L. G. Wang, R. M. Guo, G. C. Yue, and S. K. Guan, *Materials & Design*, 2016, 96, 54.

40. C. Zhang, S. Guan, L. Wang, S. Zhu, J. Wang, and R. Guo, *Advanced Engineering Materials*, 2017, 19, 1600326.

6. CAPÍTULO 6 – CONSIDERAÇÕES FINAIS

6.1 Conclusões gerais

O processamento por deformação plástica severa além de modificar as propriedades mecânicas (resistência mecânica, ductilidade e dureza), pode ser utilizado para aumentar a resistência à corrosão do magnésio em solução de 3.5 wt.% de NaCl. O processamento também pode ser utilizado para modificar o perfil de corrosão do magnésio fazendo com que o perfil de corrosão localizada típico do material no estado como fundido seja convertido em um perfil de corrosão mais generalizada como o apresentado pelo material processado por HPT.

No caso das ligas AZ31 e ZK60, o processamento por HPT modifica as propriedades mecânicas do material, mas não afeta a resistência à corrosão. O processamento da liga AZ91 por HPT pelo fato de poder ser realizado em temperatura ambiente e ao contrário de outros tratamentos termomecânicos (ex: extrusão, laminação, ECAP e etc) aparentemente é um dos mais adequados para a liga AZ91, pois limita o crescimento da fase β o que faz com que o processamento não afete negativamente a resistência à corrosão dessa liga.

Tanto o histórico de processamento quanto o tamanho médio de grão não afetam a biocompatibilidade do magnésio comercialmente puro. Esse comportamento é um diferencial importante em relação à utilização de elementos de liga para melhorar as propriedades mecânicas e a resistência à corrosão, pois o uso de elementos de liga pode comprometer a biocompatibilidade do material.

6.2 Contribuiçoes originais

A partir de amostras de magnésio no estado como fundido e utilizando diferentes técnicas e rotas de processamento (laminação, laminação + recozimento, ECAP e HPT), foi possível obter amostras com diversos tamanhos médio de grão cobrindo uma ampla faixa de 0.5 μm a 480 μm. Na revisão de literatura, realizada antes e durante a execução desta pesquisa, não foram encontrados trabalhos semelhantes que utilizaram amostras

cobrindo um faixa, de tamanho médio de grão, tão ampla. Nos trabalhos publicados que utilizam amostras de magnésio com grãos finos (da ordem de poucos microns) e ultrafinos (< 1μm), as amostras foram produzidas utilizando técnicas de processamento diferentes (moagem de alta energia e ECAP com pressão contrária). Nas pesquisas que utilizam amostras de magnésio processadas por ECAP sem pressão contrária, o menor tamanho médio de grão alcançado é uma ordem de grandeza maior do que o obtido no presente trabalho.

Com essas amostras, foi possível avaliar a influência dos diferentes processamentos e do tamanho médio de grão na resistência mecânica, ductilidade, biocompatibilidade e na taxa de corrosão do magnésio em solução de 3.5 wt.% de NaCl .

Também não foram encontrados na literatura trabalhos que avaliaram a influência do processamento por HPT sobre o comportamento em corrosão de amostras de magnésio e das ligas AZ31, AZ91 e ZK60. Com essa pesquisa foi possível avaliar e comparar diretamente a influência do processamento por HPT sobre o comportamento mecânico e a resistência a corrosão em solução de 3.5 wt.% de NaCl, utilizando amostras de magnésio comercialmente puro e ligas comerciais de magnésio.

6.3 Produção acadêmica relacionada

6.3.1 Artigos Publicados

Silva, C. L.P.; Tristão, I. C.; Sabbaghianrad, S.; Torbati-Sarraf, S. A.; Figueiredo, R. B.; & Langdon, T. G. (2017). Microstructure and Hardness Evolution in Magnesium Processed by HPT. Materials Research, 20, 2-7.

Silva, C.L.P; Oliveira A.C.; Costa C.G.F.; Figueiredo, .RB.; de Fátima Leite M.; Pereira M.M.; Lins, V.F.C.; Langdon, T.G.; (2017) Effect of severe plastic deformation on the biocompatibility and corrosion rate of pure magnesium. Journal of Materials Science. (10):5992-6003.

6.3.2 Artigos Submetidos

Silva, C. L., Soares, R.B., Pereira, P. H. R., Figueiredo, R. B., Lins V. F. C., Langdon, T. G. The effect of high-pressure torsion on microstructure, hardness and corrosion behavior for pure magnesium and different magnesium alloys. Artigo submetido e aceito para publicação no periódico Advanced Engineering Materials.

6.4 Sugestões para trabalhos futuros

- ✓ Estudar a influência do processamento por SPD na taxa de corrosão utilizando outras ligas de magnésio.
- ✓ Estudar a influência do processamento por SPD na taxa de corrosão do magnésio em outros meios (ex: solução com diferentes concentrações de NaCl).
- ✓ Usinar implantes de magnésio processados por SPD (Chapas, parafusos, fios, Scaffolds).
- ✓ Realizar testes de corrosão *in vitro* de implantes feitos de magnésio processado por SPD.
- ✓ Realizar testes de corrosão *in vitro* com implantes usinados por diferentes processos de fabricação.
- ✓ Estudar a degradação dos implantes usinados utilizando microtomografia. E utilizar as imagens (3D) em conjunto com um software de simulação por elementos finitos para estudar a variação da resistência mecânicas ao longo do período de imersão.
- ✓ Realizar testes de degradação *in vivo* dos implantes usinados que apresentaram os melhores resultados nos testes *in vitro.*

- ✓ Estudar a influência da velocidade de rotação na taxa de crescimento da fase β e na resistência a corrosão durante o processamento da liga AZ91 por HPT.

- ✓ Estudar de maneira mais detalhada a influência de diferentes frações de alumínio na resistência mecânica e na resistência a corrosão em ligas de magnésio do tipo AZ (ex: AZ21, AZ31, AZ61 e AZ91) submetidas a tratamento térmico de solubilização.

7. APÊNDICE A – MONTAGENS EXPERIMENTAIS E METODOLOGIAS

Testes de evolução de hidrogênio

As medidas da taxa de corrosão por evolução de hidrogênio foram realizadas em meio de 3.5 wt.% de NaCl em temperatura ambiente. Na figura 7.1 é apresentado o esquema da montagem utilizada para os testes de evolução de hidrogênio. Nessa montagem as amostras foram colocadas em um béquer de 250 ml preenchido com a solução de interesse e cobertas com um funil para coletar o hidrogênio gerado no processo de degradação. Posteriormente uma proveta graduada, também preenchida com a solução de NaCl, foi mergulhada no béquer de maneira a se encaixar na haste do funil tomando os devidos cuidados para não deixar a solução no interior da proveta escapar. Para evitar que uma das faces da amostra ficasse em contato com o fundo do recipiente a mesma permaneceu suspensa durante todo o ensaio, amarada por um fio de Nylon.

Figura 7.1 – Esquema da montagem utilizada para determinação da perda de massa por evolução de hidrogênio

O volume inicial V_o de gás no interior da proveta foi medido no início de cada teste e para o cálculo do número de mols de hidrogênio gerado, foi utilizada a equação dos gases ideais. Devido ao fato da pressão hidrostática, gerada pela coluna do liquido no

interior da proveta, ser bastante reduzida (≈ 1% da pressão atmosférica), a mesma foi desprezada nos cálculos. Com essa simplificação a pressão do hidrogênio no interior do béquer ficou resumida a pressão atmosférica local equação 1.

$$P_{atm}.V = n.R.T \tag{7.1}$$

Testes Eletroquímicos

Para a realização dos testes eletroquímicos foi utilizado um porta amostras do tipo cachimbo figura 7.2 que comporta amostras de tamanho reduzido e sem embutimento.

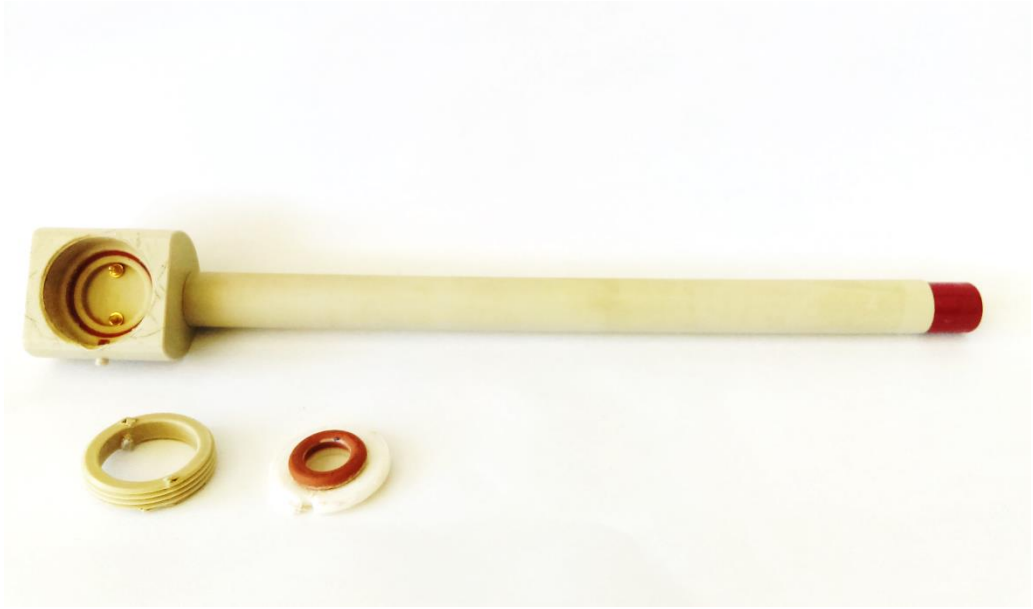

Figura 7.2 – Porta amostras tipo cachimbo.

Uma célula eletroquímica composta por 3 eletrodos sendo o eletrodo (Ag/AgCl) utilizado como referência, uma malha de platina utilizada como contra-eletrodo e as amostras de magnésio como eletrodo de trabalho. A célula foi montada utilizando um béquer de 250 ml. Os eletrodos foram colocados no recipiente suspensos por um suporte, conforme a disposição mostrada na figura 7.3. As superfícies das amostras foram preparadas utilizando lixas de carbeto de silício até a granulação 4000# para obter um acabamento espelhado. Em seguida as amostras foram limpas com álcool absoluto e secas com um soprador de ar.

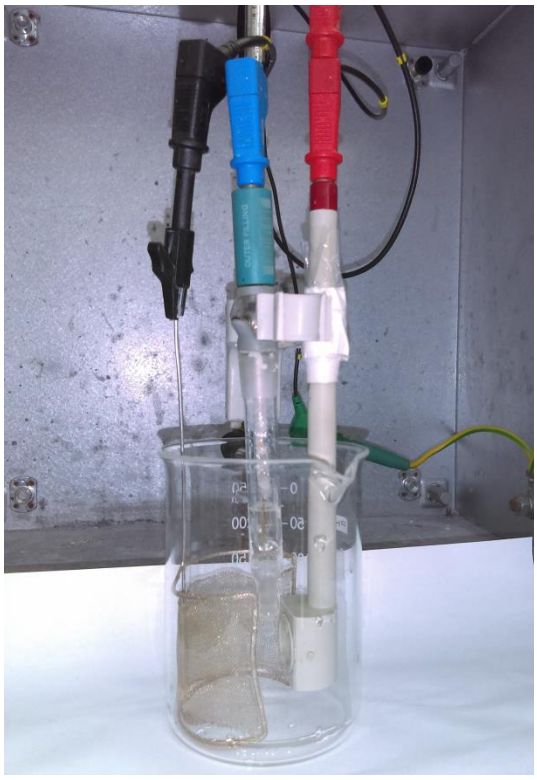

Figura 7.3 – Montagem da célula eletroquímica.

Para determinação do tempo padrão de imersão antes do início dos testes (tempo de OCP), foram realizados alguns testes preliminares. O tempo para a estabilização do potencial para as diferentes amostras foi determinado e o maior tempo de OCP encontrado foi utilizado como padrão para todas as amostras. Os testes de polarização potenciodinâmica foram feitos com uma taxa de varredura de 1 mV/s de -2.0V a -1.0V. Por sua vez os testes de impedância eletroquímica foram realizados utilizando um sinal senoidal de 10 mV de amplitude em relação ao potencial de OCP fazendo uma varredura na faixa de frequência de 10 KHZ a 10 mHZ.